UNIVERSITY OF SOUTHAMPTON

FACULTY OF ENGINEERING AND THE ENVIRONMENT
Aerodynamics and Flight Mechanics Research Group

Effects of Large-Scale Free-Stream Turbulence on a Zero-Pressure-Gradient Turbulent Boundary Layer

by

Eda Dogan

Thesis for the degree of Doctor of Philosophy

March 2017

UNIVERSITY OF SOUTHAMPTON

ABSTRACT

FACULTY OF ENGINEERING AND THE ENVIRONMENT
Aerodynamics and Flight Mechanics Research Group

Doctor of Philosophy

EFFECTS OF LARGE-SCALE FREE-STREAM TURBULENCE ON A ZERO-PRESSURE-GRADIENT TURBULENT BOUNDARY LAYER

by Eda Dogan

The focus of this study is to investigate the characteristics of a zero-pressure-gradient turbulent boundary layer in the presence of large-scale free-stream turbulence. Particular attention is given to scale interactions occurring within the turbulent boundary layer. The free-stream turbulence was generated by an active grid. The investigation was conducted as an experimental work using hot-wire anemometry and Particle Image Velocimetry. Large-scale structures occurring in the free-stream are shown to penetrate the boundary layer and increase the streamwise velocity fluctuations throughout. The near-wall peak amplitude of the streamwise velocity fluctuations are observed to increase with increasing turbulence level in the free-stream. This trend has been found analogous to high Reynolds number flows for increasing Re_τ. Free-stream turbulence imposes an outer energy peak in the boundary layer and the energy level of this peak is observed to increase with increasing turbulence level. It is also shown that the large-scales dominating the outer region of the boundary layer have a modulating effect on the small-scales in the near wall region; this effect becomes more significant with increasing turbulence level in the free-stream. These added up to the analogy between the high Reynolds number flows and present study cases. The latest efforts in the field of high Reynolds number flow investigations are aimed towards predicting the near-wall turbulence using only the large-scale information input. Therefore, this analogy has encouraging implications towards generalising large-scale influences on the near-wall small scales. The study also presents results regarding the structural organisation inside the boundary layer using the PIV data. The coherent structures found inside the boundary layer are observed to have inclined features as consistent with the previous studies for canonical flows. The fact that the external disturbance, such as FST in this study, does not alter the organisation of the structures inside the boundary layer could potentially provide an evidence for a universal structure for all wall-bounded flows as also proposed from previous studies in the literature.

Contents

List of Figures

List of Tables

Declaration of Authorship

I, Eda Dogan , declare that the thesis entitled *Effects of Large-Scale Free-Stream Turbulence on a Zero-Pressure-Gradient Turbulent Boundary Layer* and the work presented in the thesis are both my own, and have been generated by me as the result of my own original research. I confirm that:

- this work was done wholly or mainly while in candidature for a research degree at this University;
- where any part of this thesis has previously been submitted for a degree or any other qualification at this University or any other institution, this has been clearly stated;
- where I have consulted the published work of others, this is always clearly attributed;
- where I have quoted from the work of others, the source is always given. With the exception of such quotations, this thesis is entirely my own work;
- I have acknowledged all main sources of help;
- where the thesis is based on work done by myself jointly with others, I have made clear exactly what was done by others and what I have contributed myself;
- parts of this work have been published as:
  Dogan, E., Hanson, R. E., and Ganapathisubramani, B. (2016). Interactions of large-scale free-stream turbulence with turbulent boundary layers. *Journal of Fluid Mechanics*, 802:79–107
  Dogan, E., Hearst, R. J., and Ganapathisubramani, B. (2017). Modelling high Reynolds number wall–turbulence interactions in laboratory experiments using large-scale free-stream turbulence. *Philosophical Transactions of the Royal Society of London A: Mathematical, Physical and Engineering Sciences*, 375(2089)

Signed:..

Date:...

Acknowledgements

Coming to the University of Southampton to undertake a PhD has been an amazing journey in the pursuit of a long-dreamed career path and for myself. I would like to acknowledge some of the many people that took part in this journey.

First and foremost, I would sincerely like to thank my supervisor Prof. Bharath Ganapathisubramani for giving me the opportunity to conduct research with him. I owe a great debt to his guidance, patience and unwavering support throughout these years. I can say, without any doubt, that I am privileged to have worked with him and to have experienced a cutting-edge research environment. I also had the chance to work in close collaboration with Dr Ronald E. Hanson and Dr R. Jason Hearst, from whom I learned a lot about experimentation and particularly hot-wires. I appreciate all the long hours of work and fun in the lab. I also would like to mention Dr Roeland de Kat for always being encouraging in any research or career-related chats we had. I also would like to thank Dr Robert Bleischwitz for designing and manufacturing the active grid for this project. I deeply appreciate his time and effort on this. I also would like to mention Luis Blay Esteban for his hard work on his master-degree project that made my mentoring fun with a valuable piece of work.

It was very nice to be part of BGroup and I am really happy to have met and to have worked with all the people in my research group. I would like to thank Laura for proof-reading part of the thesis at short notice and for all the theatre shows we have been to. Thank you Angeliki for being the only other member of our “secret” Turbulence team and not to mention her friendship for the good and bad. I believe we will expand that team in the future. Thank you Dario for all the things we shared that made this journey full of adventures, good food, music and trips with a great company.

And special thanks for Emeritus Prof. Cahit Çıray (back home at METU, Turkey) for encouraging me towards a research in turbulence field and for reminding me the only requirement for this PhD whenever I needed it: perseverance. I am truly proud to make him proud.

All these years away from home certainly did change many things but many stayed the same which I feel very lucky about. Thank you Çağıl, Didem, Tuğçe for always being there for me during these years. Also thanks to ones that I was so happy to meet and share this path and further: Sonia S., Sonia T., Kuti, Bahareh among many others.

And last but not least, to my mother, Ayten Doğan, my father Kemal Doğan and my sister Emel Doğan Kurtoğlu... If not for their unconditional support and love, I would not be where I am right now. I am so lucky to have them and have their support whatever I do and wherever I go. Now there is a new addition to my favourites, Güney Kurtoğlu, you were born at the right time to give your auntie the best courage to work with all the little cuteness reaching me.

This PhD project was funded by the European Research Council (ERC grant agreement no. 277472) and EPSRC (grant ref no: EP/I037717/1) and this financial support is greatly acknowledged. I have also been selected as an Amelia Earhart fellow by Zonta International Foundation that enabled me to pursue my career goals for an extra year and I am truly indebted to them.

To the memory of my grandmother, Münevver Toksoy...

Nomenclature

Roman Symbols

h	Hole size
k_x	Streamwise wavenumber
n	Decay power-law exponent
u	Streamwise velocity fluctuation
u_L	Large-scale component of streamwise velocity fluctuation
u_S	Small-scale component of streamwise velocity fluctuation
$\sqrt{\overline{u^2}}/U$	Turbulence intensity
v	Wall-normal velocity fluctuation
w	Spanwise velocity fluctuation
$-\overline{uv}$	Reynolds shear stress
x	Streamwise direction
y	Wall-normal direction
z	Spanwise direction
A	Log-law coefficient, additive constant
C_f	Skin friction coefficient
E	Hot-wire sensor voltage
H	Shape factor, δ^*/θ
I	Isotropy ratio, $\sqrt{\overline{u_0^2}}\,/\sqrt{\overline{v_0^2}}$
L	Integral length scale
L^*	Integral length scale, Mydlarski and Warhaft (1996) definition
L_e	Dissipation length scale, Hancock and Bradshaw (1983) definition
Lx_{AB}	Streamwise length scale based on correlation R_{AB}
Ly_{AB}	Wall-normal length scale based on correlation R_{AB}
M	Grid mesh length
$Q1-4$	Quadrant events
R	Amplitude modulation coefficient, Mathis et al. (2009) definition
R_{AB}	Cross-correlation coefficient between any two variables A and B
Re_λ	Reynolds number based on Taylor microscale, $\sqrt{\overline{u^2}}\lambda/\nu$
Re_τ	Reynolds number based on skin friction velocity, $U_\tau\delta/\nu$
Re_θ	Reynolds number based on momentum thickness, $U_0\theta/\nu$
Re_x	Reynolds number based on streamwise distance, U_0x/ν

S_u	Skewness factor of the streamwise velocity fluctuations
T	Mean cruise time of rotation of grid wings
U	Mean streamwise velocity
U_τ	Skin friction velocity, $\sqrt{\frac{\tau_w}{\rho}}$
V	Mean wall-normal velocity

Greek Symbols

α	Predictive model superposition coefficient, Marusic et al. (2010b) definition
β	Free-stream parameter, Hancock and Bradshaw (1983) definition
β	Predictive model modulation coefficient (Chapter 5), Marusic et al. (2010b) definition
δ	Boundary layer thickness, Perry and Li (1990) definition
δ^*	Displacement thickness
ϵ	Dissipation rate
ζ_x	Streamwise wavelength
η	Kolmogorov scale
θ	Momentum thickness
θ_L	Mean inclination angle of the large-scale structures
κ	Log-law coefficient, von Kármán constant
λ	Taylor microscale
λ_{ci}	Signed swirling strength
μ	Dynamic viscosity of air
ν	Kinematic viscosity of air
ρ	Air density
τ_w	Mean wall shear stress
ϕ_{uu}	Energy spectra of streamwise velocity fluctuations
ω_z	Spanwise vorticity component
ΔP	Pressure difference between the Preston tube and the static tap
Π	Coles wake parameter
Ω	Mean rotational speed of grid wings

Superscripts

$.^+$	Indicates inner-scaling, also referred to inner-normalisation. The variables are non-dimensionalised using U_τ and ν

Subscripts

$\cdot_0$	Indicates free-stream parameters

Acronyms

CTA	Constant Temperature Anemometer
DAQ	Data acquisition

FST	Free-stream turbulence
LSMs	Large-scale motions
PIV	Particle Image Velocimetry
VLSMs	Very-large-scale motions

Chapter 1

Introduction

1.1 Motivation

One of the most important fluid flow problems is turbulent boundary layers, which are encountered in many natural and industrial flows, for example the flow over wings and bodies, the flow inside pipes and ducts. A boundary layer is the thin layer of fluid closest to the wall. They are formed when a fluid passes over a surface and forms a velocity profile from zero on the surface to a free-stream value at a specific distance from the wall which is called the thickness of the boundary layer. Previous studies reveal that turbulence inside this thin layer is generated and sustained in two ways: slow moving fluid close to the wall being ejected outwards and fast moving fluid farther away from the wall being swept inwards towards the wall. This mechanism of turbulence production is mainly responsible for the drag that a body experiences when immersed in a fluid. This drag is also what is mainly responsible for the fuel consumption of an engineering device. Up to half of the fuel consumption of an airliner, for example, is due to that drag and this proportion goes higher for an oil tanker or submarine (Marusic et al., 2010b). To understand the drag characteristics of any engineering device is essential to develop efficient strategies on drag control and reduction. Therefore, study of turbulent boundary layers is both fundamentally and economically very important. In particular, the way this turbulence responds to any external disturbance needs significant attention as that would in turn affect the drag and thermal characteristics of that device.

Free-stream turbulence (FST) is one major external disturbance for turbulent boundary layers. FST exists above almost all industrial and naturally occurring boundary layers. The effects of FST on turbulent boundary layers include enhanced heat transfer and increased skin friction (Blair, 1983b; Hancock and Bradshaw, 1983), which can be both beneficial and detrimental for the performance of a device. FST adds multiple length scales into the boundary layer and causes changes in the nature of momentum and energy transport within, through interactions with the scales that already exist in the boundary layer. These interactions are due to the penetration of FST into the boundary layer. This penetration was studied by Hunt et al. (1998) to investigate the effects on the transition mechanisms inside the boundary layer. The effects of FST penetration inside turbulent boundary layers were discussed in Sharp et al. (2009). They suggested that depending on its level, FST can penetrate into the boundary layer as well as affecting the small near-wall scales. However, Sharp et al. (2009) were not able to provide measurements very close to the wall. The near-wall information is needed to establish a clear relationship between the near-wall turbulence and FST level and to determine the extent of the FST penetration into the near-wall region. Currently the mechanism on how FST interacts with the outer region of the boundary layer and how this in turn affects the near-wall turbulence, specifically in the context of scale interactions, is not well understood. Also, to the author's knowledge, the dominant mechanisms for the generation and the sustenance of turbulence inside the turbulent boundary layer as a result of these interactions have not been tackled previously. With these motivations in hand, this study aims to contribute towards the understanding of the scale interactions and to shed light on the leading mechanisms of turbulence production inside the turbulent boundary layer in the presence of large-scale FST. This would ultimately count towards the general understanding of turbulent boundary layers and aid those who seek to develop new robust flow control strategies for practical applications such as turbomachinery and wind turbines.

1.2 Wall-bounded turbulent flows

Wall-bounded turbulent flows involve boundary layers, channels and pipe flows. Canonical cases of these flows correspond to incompressible, fully developed channel and pipe flows and zero-pressure-gradient boundary layers, which are not affected by surface roughness, wall curvature or outer disturbance. In this study, the presence of FST above the turbulent boundary layer forms a non-canonical case; however findings will be discussed mostly in comparison with canonical flows, particularly in relation to high Reynolds number cases for the reasons that will be clear later in the study. Therefore, the brief literature of the wall-bounded turbulent flows presented here relate to canonical cases. Reynolds number here is defined based on the skin friction velocity as $Re_\tau = \delta U_\tau / \nu$ with δ boundary layer thickness, U_τ skin friction velocity and ν kinematic viscosity. The conventions used in the literature to define the coordinate axes and corresponding fluctuating velocity components might differ; therefore, for the sake of consistency, the convention used in this study is as follows: the axis system, x, y and z refer to the streamwise, wall-normal and spanwise directions, respectively, with u, v and w respective fluctuating velocity components.

Wall-bounded turbulent flows can be described by two main regions with two distinct scalings: inner and outer regions with inner and outer scalings, respectively. The inner region is where the viscosity dominates and the outer region where it does not (Marusic et al., 2010c). Consistent with this, the inner velocity scaling is the friction velocity, $U_\tau = \sqrt{\tau_w/\rho}$ where τ_w is the mean wall shear stress and ρ is the fluid density. The characteristic inner length scale, ν/U_τ, and inner time scale, ν/U_τ^2, have also been defined using kinematic viscosity, ν. These scales are dynamically significant near the wall (Klewicki, 2010). The properties that are scaled with inner unit variables are traditionally shown with a superscript of +. The outer length scale is defined by δ, which could be the boundary layer thickness or half-channel height or the pipe radius depending on the wall-bounded flow in context. Friction velocity can be used for the outer region as well as the inner region. When the Reynolds number is high enough, both of the scalings are simultaneously valid in an overlap region (Millikan, 1938). Using the overlap argument, the streamwise velocity can be expressed in inner scaling as in the following logarithmic law:

$$U^+ = \frac{1}{\kappa} \ln y^+ + A \tag{1.1}$$

where $y^+ = yU_\tau/\nu$ is the inner-scaled wall-normal position, κ is the von Kármán constant and A is the additive constant of the log-law. The extent of this overlap region (in terms of y^+) is known to increase with increasing Reynolds number (Panton, 2001). A historical account for the overlap region is extensively detailed in Örlü (2009). In light of these scalings and the overlap argument of these scalings, the mean structure of the turbulent boundary layer can be well-depicted as in Figure 1.1. As such, apart from the overlap region, the boundary layer can be classically divided into the following regions: the viscous sublayer that extends to about $y^+ = 5$, the buffer layer between $5 < y^+ < 30$, the classical logarithmic layer from $y^+ = 30$ to $y/\delta \approx 0.2$ and the wake/outer layer extending from the outer edge of the logarithmic layer to the outer edge of the boundary layer, $0.2 \leq y/\delta \leq 1$. The limits of these regions are approximate (and different for pipes and boundary layers) and are still controversial.

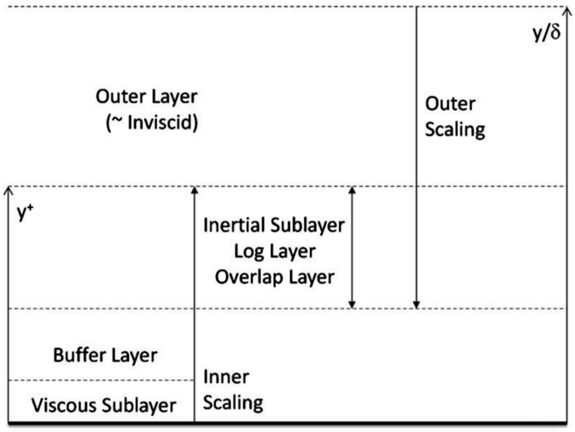

Figure 1.1: Schematic of the mean velocity scaling and different regions of the boundary layer taken from Klewicki (2010) as adapted from the work of McKeon and Morrison (2007).

The present study will not make an attempt to contribute towards the known issues related to the mean structure of the boundary layer such as the extent of the layers, universality of the log-law coefficients or the overlapping argument; however, it might challenge the robustness of these arguments in the case of a strong external disturbance.

1.2.1 Coherent motions

The current view of turbulent structure in turbulent boundary layers identifies four principal elements: near-wall streaks, hairpin vortices, large-scale motions (LSMs) and very-large-scale motions (VLSMs) (Smits et al., 2011). Theodorsen (1952) was the first one to propose a structural model for the turbulent boundary layer. In this model, he acknowledged the presence of hairpin vortices that are responsible for turbulence transport. This model is followed by many studies focusing on the near wall region of the turbulent boundary layer. Kline et al. (1967) observed the formation of low-speed streaks near the wall by carrying out a landmark visualisation experiment using hydrogen bubbles. They also spotted that these low-speed streaks begin to oscillate and suddenly break-up into a violent motion called a "burst", a process for which these streaks are assigned a main role in the turbulence production cycle. Later, another landmark visualisation study by Corino and Brodkey (1969) enabled the workers to expand the definition for turbulence producing events to include: "ejections" as low-speed fluid close to the wall being pushed away from the wall and "sweeps" as high-speed fluid being moved towards the wall. In an attempt to quantify these visual observations, Wallace et al. (1972) and Willmarth and Lu (1972) introduced uv quadrant splitting. This was one of the many suggested conditional sampling methods to infer turbulence events.

Strong experimental evidence of the presence of hairpin vortices was further provided by Head and Bandyopadhyay (1981), who observed that these structures were becoming increasingly elongated with higher Reynolds numbers. They suggested that these hairpin vortices could themselves be organised into larger coherent groups and have inclined features with an angle of 15° to 20° with the wall.

When multiple hairpin structures travel at the same convective velocity, they form vortex packets which in turn create large-scale motions (LSMs) or turbulent bulges (Kim and Adrian, 1999). Very long, meandering, features consisting of narrow regions of low-streamwise-momentum fluid flanked by regions of higher-momentum fluid have been observed in the logarithmic and wake regions of turbulent boundary layers (Kim and Adrian, 1999; Guala et al., 2006; Hutchins and Marusic, 2007a). These structures are called very large-scale motions (VLSMs) in pipe and channel flows and superstructures in boundary layer flows. A different name for the structure depending on the type of flows implies quantitative differences among these flows (Monty et al., 2009). They are populated in the outer region of the boundary layer and carry a significant portion of the turbulent kinetic energy, which contributes to almost half of the Reynolds shear stress in the boundary layer (Ganapathisubramani et al., 2003; Guala et al., 2006; Balakumar and Adrian, 2007). With increasing Reynolds number, these large-scale structures become more energetic. Coherent structures within the turbulent boundary layer are known to be dominated by these energetic large-scales at high Reynolds numbers (Hutchins and Marusic, 2007a). The following section briefly introduces the characteristics of a high Reynolds number flow and its dominant features.

1.2.2 High Reynolds number turbulent boundary layers

Defining high Reynolds number flows

Most of the turbulent flows we encounter in everyday's life exhibit very high Reynolds number. The flow in the atmosphere, over aircrafts and submarines and in large pipe flows are some examples. Understanding high Reynolds number turbulence is important to better understand meteorological events and to design energy efficient vehicles.

One distinct feature of a high Reynolds number flow in comparison to a low Reynolds one is the major contribution to the bulk turbulence production. At high Reynolds numbers, the major contribution comes from the logarithmic region, whereas at low Reynolds numbers it occurs within the viscous buffer layer. This is well illustrated in Figure 1.2 with the pre-multiplied form of the production term. This form allows to represent equal contributions to the total production by equal areas. The increasing contribution of the logarithmic region, i.e. the extended plateau, to the total production with increasing Reynolds numbers is evident from this figure. The cross-over where the logarithmic region starts to dominate in the production is estimated to occur at $Re_\tau \approx 4200$.

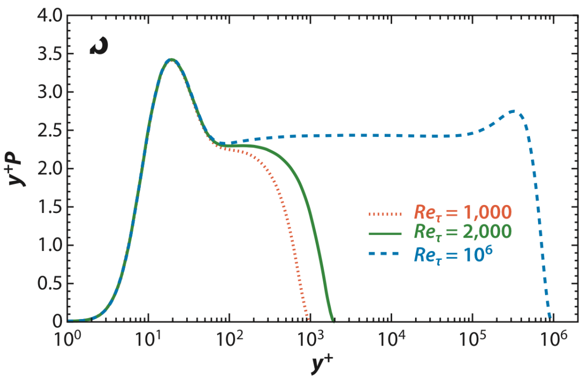

Figure 1.2: Turbulence kinetic energy production in pre-multiplied form for a range of Reynolds numbers (taken from Smits et al., 2011 as adapted from Marusic et al., 2010a).

Another distinctive feature of a high Reynolds number flow is a sufficient separation of scales. According to Hutchins and Marusic (2007a,b), $Re_\tau > 4000$ is required to ensure enough separation between the largest and smallest scales. They considered the full u spectrogram across the boundary layer using Taylor's hypothesis such that $\lambda_x = 2\pi/k_x = U/f$ as shown in Figure 1.3 (Note that λ_x is their representation for streamwise wavelength, in the present study it will be denoted as ζ_x). This way of representing the velocity spectra has been widely used in the community to show the energy distribution in the boundary layer. The spectra is a clear illustration of the evolution of two distinct (inner and outer) energy peaks with increasing Reynolds number (Hutchins and Marusic, 2007a; Smits et al., 2011). The inner energy peak (white + sign) at $y^+ = 15$ ($\lambda_x^+ = 1000$) is present for both Reynolds numbers. However, the outer peak (black + sign) is barely distinguishable at the lower Reynolds number whereas the spectral outer peak separation is easily seen for higher Reynolds number case. Hutchins and Marusic (2007b) also highlighted a region with initials "FP" for the footprint of the increasing outer energy in the near-wall region. They showed that this footprint can extend deep into the near-wall region and lead to an increase in the near-wall streamwise turbulence intensities. All of this has been attributed to the large energetic motions in the outer region that carry more and more energy with increasing Reynolds number. These motions appear to be the dominating structures of high Reynolds number flows and the primary driving mechanism for scale interactions.

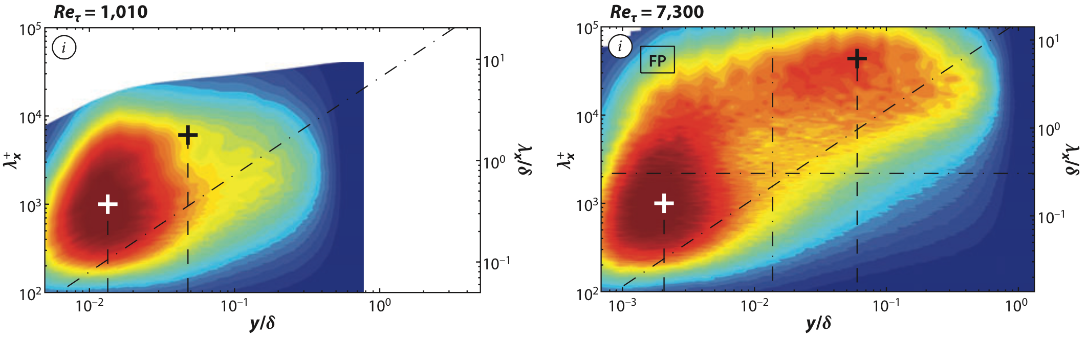

Figure 1.3: Contour maps of pre-multiplied energy spectra of streamwise velocity fluctuations across the whole boundary layer for two Reynolds numbers (taken from Hutchins and Marusic, 2007b).

Scale Interactions in High Reynolds Number Turbulent Boundary Layers

Large-scale structures are found to exhibit a footprint in the near-wall region affecting the near-wall structures (Hutchins and Marusic, 2007a). They also showed that these large scales in the outer region tend to modulate the amplitude of the small-scale fluctuations in the near-wall region (Hutchins and Marusic, 2007a). This sort of interaction between the scales has been examined before by Bandyopadhyay and Hussain (1984) for various shear flows, including boundary layers, mixing layers, wakes and jets. They found significant coupling between the scales across all shear flows by correlating the low-frequency component (i.e. low-pass filtered time-series data from their hot-wire measurements) with a signal similar to the envelope of the high-frequency component. Mathis et al. (2009) expanded upon this non-linear interaction and defined the modulation by a correlation coefficient, R, between the large-scale streamwise fluctuating velocity and an envelope of the small-scale fluctuations to quantify the level of modulation across the boundary layer. Their profiles of R provided supporting evidence of amplitude modulation of the near-wall small scales by the large scales. Mathis et al. (2009) also noted that the modulating effect of the large scales increases with increasing Reynolds number. Ganapathisubramani et al. (2012), on the other hand, explored the dependence of the level of modulation on the strength of the large-scale fluctuations. In addition, they showed significant frequency modulation of the small-scale fluctuations by the large-scales.

While there are certainly many open questions relating to how these scale interactions take place in high Reynolds number flows, there are also numerous limitations of performing measurements in the near-wall region of said flows, e.g. sensor spatial and temporal resolution, wall proximity errors (Hutchins et al., 2009; Marusic et al., 2010b). Therefore, there is high demand for accurately predicting the near-wall turbulence with only large-scale information input (Mathis et al., 2011a; Marusic et al., 2010b).

In an attempt to isolate the influence of the large scales, Jacobi and McKeon (2011a,b, 2013) and Duvvuri and McKeon (2015) introduced a single synthetic large scale into the boundary layer. Specifically, Duvvuri and McKeon (2015) found that exciting the turbulent boundary layer by a large-scale input modifies the phase relationships naturally existing between the large and small scales of the turbulent boundary layer. These phase relationships were quantified in their study by the skewness of the streamwise velocity fluctuations and the amplitude modulation coefficient as previously suggested in the literature (Chung and McKeon, 2010; Ganapathisubramani et al., 2012). While the studies of Jacobi and McKeon (2013) and Duvvuri and McKeon (2015) introduce a single large-scale into the boundary layer, the present study introduces a wide range of large-scales that are imposed from outside the boundary layer in the free-stream. The interest of the present work lies in the effects of a broadband external disturbance, namely free-stream turbulence, on the scale interactions inside the turbulent boundary layer as well as the phase relations between the scales. This will contribute towards the attempt by the previous studies cited above to generalise the large-scale influences on the near-wall small scales.

1.2.3 Free-stream turbulence effects on turbulent boundary layers

It is well known that the turbulent boundary layers are influenced by changes in external flow characteristics. In this study, the focus is on the presence of FST. Increased skin friction and enhanced heat transfer are the most prominent effects of FST that are widely studied in the literature. Charnay et al. (1976), Hancock and Bradshaw (1983), Blair (1983a) and Castro (1984) are among many who used bar grids to generate the turbulence in the free-stream. Reynolds number dependence of these effects were investigated by Bandyopadhyay (1992) as well as Blair (1983a) and Castro (1984). The studies from Stefes and Fernholz (2004) and Nagata et al. (2011) are the more recent contributions to these findings. The boundary layer statistics for the interaction between the boundary layer and the FST were reported in Thole and Bogard (1996) and Sharp et al. (2009). Another recent study from Brzek et al. (2009) investigated the effects of FST on transitionally rough turbulent boundary layers. Although focused on rough walls, they did extensive statistical analyses of boundary layers in the presence of FST and presented some of their results in comparison with smooth wall canonical cases.

Hancock and Bradshaw (1983) deduced that the effect of FST was not only dependent on the turbulence intensity level but also on a characteristic length scale of FST which they defined as the dissipation length scale. They formed an FST parameter, β, using both the turbulence intensity, $\sqrt{\overline{u_0^2}}/U_0$ (%), and the length scale, L_e, to define the overall effect of the FST on turbulent boundary layers.

$$\beta = \frac{\sqrt{\overline{u_0^2}}/U_0}{\dfrac{L_e}{\delta_{995}} + 2} \tag{1.2}$$

where δ_{995} is the height at which the mean streamwise velocity in the boundary layer is equal to 99.5% of the mean free-stream velocity, U_0. L_e is defined from the decay power law of the grid turbulence (Castro, 1984). The subscript "0" is used to denote the free-stream values. Blair (1983b) added a damping term to this parameter to account for low Reynolds number effects.

Later, Thole and Bogard (1996) presented boundary layer statistics for FST levels up to 20% and confirmed the validity of the log-law in the mean profiles of the boundary layer for these high turbulence levels by direct measurements of total shear stress. Stefes and Fernholz (2004) complemented the study of Thole and Bogard (1996) by providing skin friction data and measurements in the vicinity of the wall at relatively higher Reynolds numbers at FST levels up to 13%. They also presented mean and fluctuating velocity distributions for the boundary layer and showed that there were considerable changes in the outer region of the boundary layer, such as the increase in the velocity fluctuations.

The turbulent boundary layer subjected to FST becomes thicker and Hancock and Bradshaw (1983) correlated this variation in thickness to the increase in skin friction. The shape factor, H, the ratio of displacement thickness (δ^*) to momentum thickness (θ^*), was also found to be correlated with increased skin friction. However, these correlations were observed to be limited to moderate turbulence levels. When turbulence intensity levels exceed around 8-10%, the shape parameter tended towards a limit (Kondjoyan et al., 2002).

As far as the interaction between the turbulent boundary layer and the FST is concerned, Thole and Bogard (1996) showed through spectra and length scale measurements that FST penetrated into the boundary layer for turbulence levels ranging from 10 to 20%. They observed that power spectrum of the streamwise velocity fluctuations for the free-stream and for the boundary layer at the near wall location were similar even for very high turbulence cases. Based on this, Thole and Bogard (1996) concluded that the free-stream was able to penetrate through the boundary layer and to occur unaltered even very close to the wall. However, they did not distinguish between the scales of FST and the turbulent boundary layer.

Recently, Sharp et al. (2009) put the emphasis on the scale interactions and their relative intensities. They observed that for high FST cases, the energy of the FST masked that of the boundary layer's outer scale. Their measurements indicated that FST could penetrate into the boundary layer and affect the wall stress as well as the small scales, depending on its intensity. They related their observations to the work of Hutchins and Marusic (2007a) and Mathis et al. (2009) who examined inner-outer scale interactions for canonical high Reynolds number turbulent boundary layers. These works were detailed in the previous section for high Reynolds number flows. However, the near-wall information is required to establish inner-outer interactions and the work from Sharp et al. (2009) was not able to provide very near-wall measurements in this respect. One motivation of the present study, therefore, lies in these scale interactions inside the boundary layer in the presence of large-scale FST by providing the near-wall information.

1.3 Generating turbulence in the free-stream: active turbulence grids

In the course of this study, an active turbulence grid was employed to generate the turbulence in the free-stream. There are different methods to generate turbulence other than the conventional static or active grids in the literature such as turbulence-generating-jets (Thole and Bogard, 1996; Stefes and Fernholz, 2004). The main focus of these studies is usually to simulate the flows in gas turbines where high FST levels in the range of 20-30% occur. Although they correspond better to practical applications, more care has to be taken when dealing with these flows. The reason is that they result in a highly non-uniform mainstream and a balance should be established between the flow uniformity which increases in the downstream direction of the jet and the FST which decays in the same direction (Stefes and Fernholz, 2004). Using an active grid as a means of generating the turbulence has the advantage of being a well-documented flow (Makita, 1991; Mydlarski and Warhaft, 1996; Kang et al., 2003; Larssen, 2005; Hearst and Lavoie, 2012).

The aim of creating uniform and transversely homogeneous decaying turbulent flow in a wind tunnel using grids, consisting of circular or rectangular bars, dates back to Simmons and Salter (1934). Grid turbulence is usually characterised in terms of its turbulence intensity ($\sqrt{\overline{u_0^2}}/U_0$ where u_0 is the streamwise velocity fluctuations and U_0 is the mean streamwise velocity of the free-stream) and its Taylor Reynolds number ($Re_{\lambda_0} = \sqrt{\overline{u_0^2}}\lambda_0/\nu$) based on the root-mean-square of the streamwise velocity fluctuations, the kinematic viscosity, ν, and the Taylor microscale, λ_0. These traditional grid designs, also called static grids, allow a limited value of Taylor Reynolds number (up to only a few hundred), turbulence intensities (up to a few percent) and integral scales (small compared to the facility dimensions).

The alternatives were investigated to improve the design in terms of dynamic features, as opposed to static features of conventional grids. The most widely accepted and implemented design was introduced by Makita (1991), namely active turbulence generating grid (also called active grid). Their design was developed in the early eighties and was published in Makita and Miyamoto (1983); however, the details of the design was not revealed until Makita (1991). The design uses rotating grid bars with attached agitator wings on them, which results in a space- and time-varying solidity (the ratio of open cross-sectional area to total cross-sectional area) that is, on average, much higher than that found in most conventional grids. Similar concept grids have been used since then by Mydlarski and Warhaft (1996), Poorte and Biesheuvel (2002), Kang et al. (2003), Larssen (2005), Sharp et al. (2009), Cekli and Water (2010), Knebel et al. (2011) and Hearst and Lavoie (2012) for many different applications like simulating atmospheric conditions or flows in gas turbines or in the interest of investigating the decaying grid turbulence in more detail. Comparisons of these different designs are given in Chapter 2.

The original design of Makita (1991) consisted of a rectangular array of diamond-shaped wings attached to 8 horizontal and 8 vertical rows of rotating bars. Each rotating bar was controlled by a stepper motor allowing random direction changes. This design was able to achieve an integral length scale of 19.7 cm, turbulence intensities of 16% and a Re_{λ_0} of 387 for a flow speed of 5 m/s. However, the anisotropy ratio related to that design was higher than the value of static grids which is less than 1.1. To improve isotropy, Poorte and Biesheuvel (2002) suggested the use of a staggered configuration of wings as opposed to parallel configuration in Makita's original design. Parallel wing configuration requires wings of adjacent rods to be in parallel planes, i.e. they are alternately positioned on opposite side of the rod, whereas in staggered configuration adjacent wings are placed perpendicularly along every rod. This solution reduced the anisotropy ratio at the expense of Re_{λ_0} due to smaller integral length scales and lower turbulence intensities. However, Kang et al. (2003), who also used parallel wing configuration, found out that the anisotropy is mostly associated with the largest scales of the flow on the order of the test section size and the inertial-range dynamics are nearly isotropic.

The flow behind the grid can be described as a decaying turbulence and is governed by the following power-law (Gad-El-Hak and Corrsin, 1974),

$$\frac{\overline{u^2_{0,local}}}{U^2_{0,local}} = D\left(\frac{x - x_o}{M}\right)^n \tag{1.3}$$

where $u_{0,local}$ and $U_{0,local}$ is the streamwise velocity fluctuation and the mean streamwise velocity of the free-stream, respectively, at the local downstream measurement station behind the grid, D is the decay coefficient, x is the downstream distance of the local measurement station from the grid, x_o is the virtual origin of the grid (assumed zero in the study by Mydlarski and Warhaft (1996)), M is the mesh length of the grid and n is the decay exponent of the power-law. Reviewing some of the active grid studies in the literature, Larssen (2005) found out, without generalising, that the decay exponent, n, might be common for different grid designs, a value around -1.3 within experimental error, whereas D and x_0 can be dependent on grid geometry and/or Reynolds number.

1.4 Objectives and approach

The current knowledge of a turbulent boundary layer under the effect of FST, as summarised in previous sections, lacks the near-wall information and thus possible interactions between FST and the boundary layer in that region. The primary objective of the present study is to contribute towards the understanding of the scale interactions in a turbulent boundary layer in the presence of large-scale FST. The main questions that this study is trying to answer are:

- Does large-scale FST have a direct effect on the near-wall small-scales and/or does it affect through modulation?
- Does the flow of interest have similar scale interactions to high Reynolds number flows that could potentially lead to generalising large-scale influences?
- What are the governing turbulence producing events in the boundary layer under the effect of FST?
- How is the structural organisation of the turbulent boundary layer affected due to the penetration of large-scale FST?
- What is the effect of increasing turbulence intensity level of the free-stream on all the features stated above?

The investigation approach is purely experimental. Measurements of the streamwise velocity in the boundary layer and in the free-stream are obtained using two single-component hot-wire anemometers. These measurements will be used to characterise both flows in detail. At the same downstream position, further measurements are performed using multiple hot-wires to enable cross-correlations between the signals from different wall-normal locations in the boundary layer. Preston tube measurements are used to obtain the skin friction velocity. In addition, planar Particle Image Velocimetry (PIV) is conducted in streamwise-wall-normal plane to reveal the spatial characteristics of the flow and provide comparison with temporal characteristics where applicable.

1.5 Thesis outline and author's contributions

Chapter 2 introduces the experimental setup and the instrumentations used throughout the study. Chapter 3 presents mean flow and bulk characteristics of the flow for different FST conditions using single-wire measurements and Chapter 4 uses the same dataset for turbulence statistics and spectral analysis. These two chapters are parts of the recent published work in *Journal of Fluid Mechanics* (Dogan et al., 2016). Chapter 5 discusses the results from multiple-wire measurements in the context of scale interactions which forms a part of the published work in *Philosophical Transactions of the Royal Society A: Mathematical, Physical and Engineering Sciences* (Dogan et al., 2017). Chapter 6 presents PIV results and discusses the structural organisation in the presence of FST. The last chapter summarises the study and concludes with some recommendations for further work. Appendix A has additional plots for velocity fluctuations and Appendix B has some snapshots for vorticity and swirling strength.

The active grid used in this study was designed and built during the course of the study by Robert Bleischwitz and the process was assisted by the author. The operational schemes of the active grid were developed by the author based on similar studies from the literature. The experiments were performed by the author and the author was assisted for the setups by Dr Ronald E. Hanson and later by Dr R. Jason Hearst. The analysis of all experimental data was performed by the author. The pixel-locking algorithm applied to PIV data of this study was developed by Hearst and Ganapathisubramani (2015) who used the present dataset for their analyses. The author also mentored a master degree project by Luis Blay Esteban which resulted in the validation of skin friction measurements of this study by oil film interferometry.

This work has also been presented by the author in the following conferences:

Dogan E, Hearst RJ, Hanson R, Ganapathisubramani B *Comparison of spatial and temporal characteristics of a turbulent boundary layer in the presence of free-stream turbulence*. 69th Annual Meeting of the APS DFD, Portland, USA, November 20-22, 2016.

Dogan E, Hearst RJ, Ganapathisubramani B *Interactions of large-scale free-stream turbulence with turbulent boundary layers*. MULTISOLVE Workshop, Imperial College London, September 28-30, 2016.

Dogan E, Hearst RJ, Ganapathisubramani B *Interactions of large-scale free-stream turbulence with turbulent boundary layers.* Inaugural UK Fluids Conference, Imperial College London, September 7-9, 2016.

Dogan E, Hanson R, Ganapathisubramani B *Effects of external disturbances on turbulent boundary layers.* 15th European Turbulence Conference, Delft, The Netherlands, August 25-28, 2015.

Dogan E, Hanson R, Ganapathisubramani B *Effects of external disturbances on turbulent boundary layers.* 67th Annual Meeting of the APS DFD, San Francisco, USA, November 23-25, 2014.

Chapter 2

Experimental Setup and Instrumentation

This chapter describes the experimental setup and all its components. It also details the instrumentation employed to perform the measurements. The final section of the chapter introduces the uncertainty estimates for the measurements performed.

2.1 Experimental Setup

The experimental setup involved in this study consisted of several major components: the wind tunnel, the boundary layer plate and the active grid.

2.1.1 Wind Tunnel

The experiments were performed in an open-circuit suction type wind tunnel at the University of Southampton. The test section of the tunnel is 4.5 m long and has 0.9×0.6 m^2 cross-section. The tunnel speed can reach up to 30 m/s. The turbulence intensity of the tunnel is around 0.6 %. The speed control of the tunnel was achieved through an analogue output from NI-USB-6212 Data Acquisition (DAQ) device connected to the computer and controlled through MATLAB programming. The reference velocity measurements of the tunnel were performed using a Pitot-static tube connected to a Furness FCO510 pressure transducer.

2.1.2 Flat Plate

A turbulent boundary layer was established on a 4.2 m long flat plate mounted 0.135 m above the floor of the test section. The plate had a 0.1 m long sharp leading edge (machined from aluminium) that was designed to a 15° edge to ensure the flatness over the entire length of the plate on the measurement side. The leading edge was followed by an extension plate of 0.5 m long made of aluminium and then a COMPOCEL® sandwich panel of parallel 1 mm thick aluminium sheets bonded to a 8 mm thick honeycomb aluminium core. The purpose of using honeycomb sandwich panels was to have a lightweight and manageable setup. A 0.5 m long flap followed at the trailing edge of the plate and extended into the diffuser section of the wind tunnel. The flap was used to position the stagnation point on the measurement side of the plate. The leading edge of the plate was positioned 0.3 m downstream of the active grid which was placed between the contraction and the test section of the tunnel. Although the grid-generated FST could trip the boundary layer to a turbulent state, the leading edge was also equipped with a tripping wire that might have been necessary for measurements made at low FST levels.

2.1.3 The Active Grid

For this study, to generate free-stream turbulence, an active turbulence grid was designed and manufactured in-house. The design and manufacturing and operational details are given in the following sections.

Grid Sizing

The grid sizing involves setting the mesh length and consequently the number of rods. This is the most important parameter in terms of generating desired length scales for the turbulence since length scales are known to inherently scale on streamwise distance from the grid as well as the mesh length, M (Larssen, 2005). The smaller the integral length scales, the greater the chance of having good transverse homogeneity, however, large scale turbulence was aimed for this study. Therefore, M should be small enough to sustain the transverse homogeneity and large enough to achieve the large scales as desired. The sizing was decided by investigating the previous studies in the literature. Table 2.1 presents a competitive study for some of the active grid studies in the literature. The cross section of the wind tunnel that the active grid was to be inserted is 0.9×0.6 m^2 as previously mentioned. Therefore, a square mesh length, $M = 81$ mm, was chosen accordingly and this sizing resulted in 18 rods in total. The wings attached to rods were placed such that the gap between the outermost wings and the edges of the tunnel cross section was 2 mm on each side.

Design and Manufacturing of the Grid

The active grid was to be placed between the contraction section and the test section of the wind tunnel. The test section of the tunnel was extended by 300 mm by putting a dummy insert between the contraction and the test section so that the active grid

	Makita (1991)	**Mydlarski and Warhaft (1996)**	**Poorte and Biesheuvel (2002)**	**Kang et al. (2003)**	**Larssen (2005)**	**Sharp et al. (2009)**	**Knebel et al. (2011)**	**Cekli (2011)**	**Hearst and Lavoie (2012)** [1]	**Present work**
Fluid	air	air	water	air	air	air	air	air	air	air
Type and number of rods	-/15	aluminium/14	-/24	aluminium/12	aluminium/20	aluminium/15	steel/16	-/17	steel/25	aluminium/18
Rod diameter (mm)	6.0	6.4	5	N/A[2]	N/A	12.7	10	-	6.35	10
Tube diameter (mm)	N/A	N/A	N/A	19.05	25.4	N/A	N/A	N/A	N/A	N/A
Mesh width, M (mm)	46.7	50.8	37.5	152	209.55	114	110	100	80	81
Test section dimensions (width x height)	$15M \times 15M$	$8M \times 8M$	$12M \times 12M$	$8M \times 6M$	grid placed in the contraction section	$8M \times 8M$	$9M \times 7M$	$10M \times 7M$	$15M \times 8M$	$11M \times 7M$
Wing material	aluminium	aluminium	aluminium	aluminium	plywood	aluminium	aluminium	aluminium	aluminium	plywood
Wing thickness (mm)	-	0.38	1.0	3.18	4.76	1.4	-	-	-	3.0
Motor type	stepper	stepper	DC	AC	stepper	stepper	stepper	servo	integrated stepper	integrated stepper

Table 2.1: Main characteristics of previous active grids in comparison with present work

---

[1] The active grid is a double-mesh configuration which is different from the original design of Makita (1991) and the followers; but still in the table for completeness.

[2] N/A : Not applicable

placement could be easier. During the tests with the active grid, this dummy insert was being replaced by the active grid (Figure 2.1).

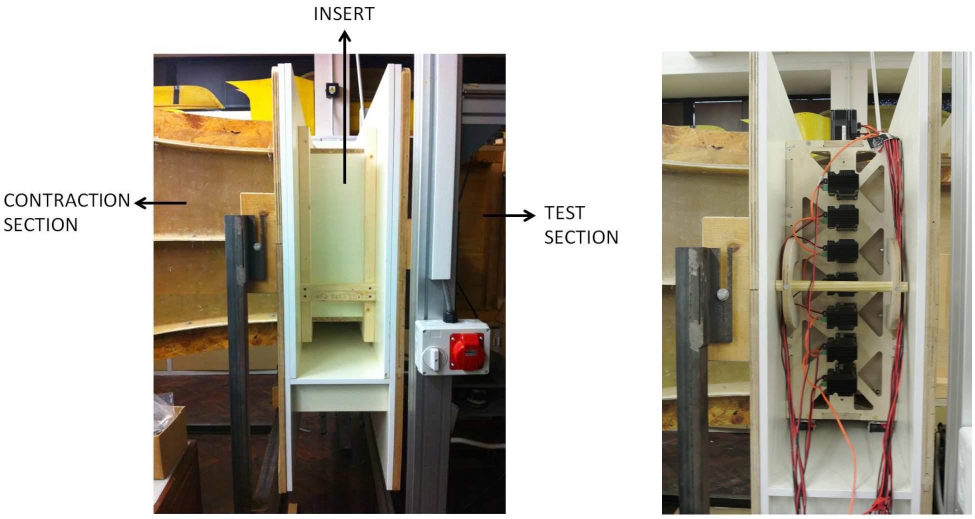

(a) Extension of the test section by a dummy insert (b) Active grid inserted

Figure 2.1: The space allocated for the active grid

The CAD model and the final assembly of the active grid are shown in Figure 2.2. The design and manufacturing details of the grid will be presented in the following paragraphs.

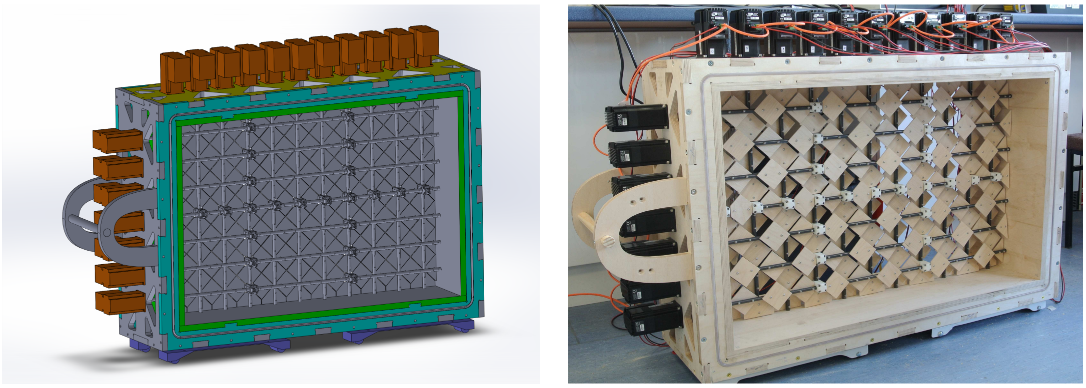

(a) CAD model (by Robert Bleischwitz) (b) The manufactured grid outside the wind tunnel

Figure 2.2: CAD model and the final assembly of the active grid

The active grid is a bi-planar configuration which requires either horizontal or vertical rods to be placed at some distance downstream/upstream with respect to the other. For the present design, horizontal rods were 20 mm upstream of the vertical rods (the distance measured between the centres of the rods) when looking from the test section of the tunnel. This distance was chosen considering the thickness of the wings such that the risk of the wings hitting adjacent ones when in operation was reduced. This was visualised at design stage in CAD model to detect any failure beforehand (Figure 2.3(a)).

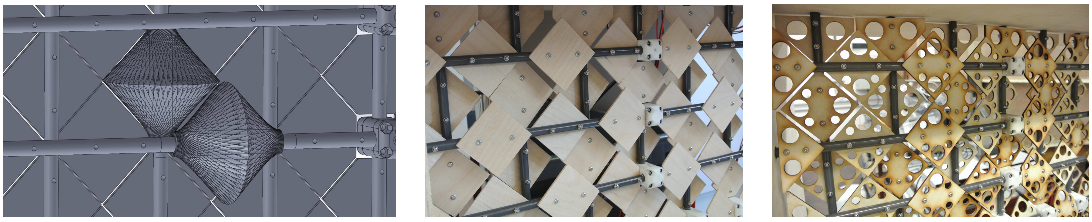

(a) CAD model (by Robert Bleischwitz) showing two representative wings in operation to test against crash. Note that the position of the non-rotating wings along the rods, i.e. non-alternating facing directions, does not reflect final configuration.

(b) Solid wings

(c) Cut-out wings

Figure 2.3: A close look at the wings of the active grid

There were two different types of wings used for the active grid as can be seen in Figure 2.3(b) and Figure 2.3(c). Initially, solid wings were manufactured. After some initial measurements, the turbulence intensity values achieved by the grid operation were found to be quite high, around 12-13% which were in most cases higher than the turbulence intensity at the near-wall peak of the turbulent boundary layer. In order to generate free-stream turbulence with a wider range of turbulence intensity, the same outer dimension wings with reduced solidity using circular cutouts, i.e. cut-out wings, were manufactured. With these two configurations, turbulence intensity levels ranging from around 7 to 13% could be produced.

The edge wings could rotate as in the original design of Makita (1991) and also as in many studies which followed the original design (Larssen, 2005; Knebel et al., 2011; Hearst and Lavoie, 2015). On the other hand, Mydlarski and Warhaft (1996) attached the edge wings to the tunnel walls which was thought to be the reason for the uniformity and homogeneity being to a lesser degree compared to the original design.

Not all the wings had the same shape. Some of the wings without any constraint had full diamond shape and these were the square wings of length 55.86 mm that had a chord length (diagonal of the square) of 79 mm. However, the wings with a constraint were shaved off on one edge and/or on both edges to prevent overlapping with the stabilising couplings and/or edges of the tunnel. Regardless of their shapes, in total, there were 172 wings that were made of plywood with 3 mm thickness. The material for the wings was chosen as plywood to make it lighter. According to their trade-off analysis in Larssen (2005) between 2.4 mm thick aluminium and 4.8 mm thick plywood wings, plywood wings were found to require about 1/3 of the torque compared to that of the aluminium. To further reduce the inertial load on the rods due to wings, some of the designs in the literature drilled holes on the wings which they could later cover with tapes to obtain different blockages. For current design, holes were considered to reduce the blockage ratio of the grid which would directly affect the generated turbulence intensity levels. The maximum blockage by the solid wings is 100%, although the probability of this incidence is very low, and this has been reduced to 75% with cut-out wings.

The rods of the active grid were chosen to be high tolerant (h8) and high tensile aluminium (AL7075) for precision and vibration concerns, respectively. Steel could also be a good option but it would be heavy and hard to machine. The wings were attached alternately on opposite sides of the rod to keep the moment of inertia symmetric for the rod. As already shown in Figure 2.2, the design comprises of two frames. The inner frame was for housing the rods and the wings which fit into the tunnel cross section. The outer frame was used for mounting the motors, holding the whole structure on four rollers to enable sliding. It also had a handle bar to pull/push the active grid from/into the space allocated in the wind tunnel. The triangular cut-outs on the outer frames, the ones visible in the figure (also elliptical cut-outs on the other sides that are not captured in the figure), were for weight concerns and also for visual accessibility purposes to be able to detect any failure during operation. For the outermost frames which were in contact with the tunnel on both sides (Figure 2.2 shows only one side), a groove of 8 mm diameter and 6 mm depth was milled. A silicon tube of 8 mm outer diameter with 2 mm wall thickness was glued inside the groove. In this way, the sealing of the tunnel could be provided. During the first trials of fitting the grid into the tunnel, these silicon tubes made it even harder to push it in; therefore, one of them, facing the test section, was removed. The grooves on each side should have been designed 1 mm deeper.

The rods were clamped at both ends with a shaft collar of 10 mm inner diameter (Figure 2.4(a)) in direct contact with the rubber sealed ball bearings (6200 RS) (Figure 2.4(b)) which were housed in the inner frame. Then the rod to motor shaft coupling was achieved through flexible couplings (Figure 2.4(c)). As mentioned previously, the distance between the horizontal and vertical rods was 20 mm between the centres of the rods. To reduce the vibration, a coupling (Figure 2.4(d)) was custom-designed and 3D-printed and inserted at the positions that were considered to be critical. The number of couplings could be more but then the torque requirements of the grid would have been much higher.

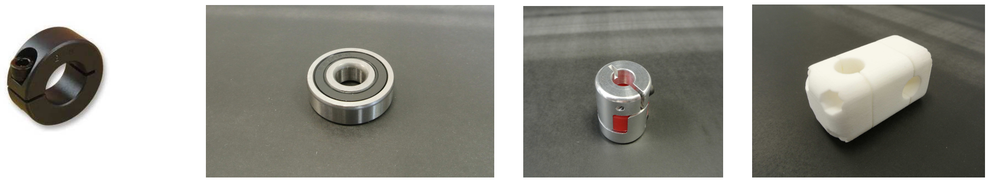

(a) Shaft collar

(b) Rubber sealed ball bearing

(c) Motor to rod coupling

(d) Coupling between horizontal rods and vertical rods

Figure 2.4: Active grid mechanical elements

Grid Control Hardware and Software

Each of the rods of the active grid could be rotated independently using stepper motors. The motors were STM23S-3RE integrated stepper motors from Applied Motion Products (AMP) with a holding torque of 1.5 Nm and a resolution of 200 steps resolution per revolution. STM23S-3RE is a drive+motor unit with an integrated encoder. The encoder eliminates the possibility of losing steps and also prevents the occurrence of stall. The motors require power supplies in the range of 12-70 VDC. For this study, 48 VDC power supplies of the same company were used to power two motors at once, i.e. 9 power supplies for 18 motors. The operational temperature for the motors was in the range of 0 to 85 degrees Celsius; however, the continuous operation of the motors more than an hour needed special attention as the motors could reach the temperature limit. Therefore, a cooling desktop fan was needed to reduce the excess heating. As an alternative improvement to the current design of the active grid, individual small desk fan for each motor could be attached on the outer frame of the grid.

These stepper motors are RS-485 serial port communication type motors. A USB-to-serial adapter was used to communicate with the motors. All 18 motors were daisy chained and connected to the adapter and then the adapter was connected to the computer through a USB port. All the control hardware is shown in Figure 2.5.

(a) Integrated stepper motor from AMP Inc.

(b) 48 V power supply from AMP Inc.

(c) RS-485 serial adapter

Figure 2.5: Active grid operational elements

The motors were controlled via a MATLAB routine. MATLAB communicated with the motors through serial port using Serial Command Language (SCL) commands. Single random forcing protocol was used in the same way as implemented by Larssen (2005) which involved randomising the rotational speed or the cruise time and forcing directional change at each random case (Figure 2.6). That means the rod is accelerated from rest at a constant rate to an angular velocity $\tilde{\Omega}$. The wings then remain at this speed for a cruise time of $\tilde{T}$ after which they decelerate at the same rate to zero. The rod then immediately re-accelerates in the reverse direction and performs a qualitatively identical manoeuvre with a new $\tilde{\Omega}$ if it is a randomised rotational speed case for the same cruise time or with the same $\tilde{\Omega}$ for a duration of different $\tilde{T}$ if it is a randomised cruise time case. The cruise time and rotation rate were varied randomly using a uniform probability density function defined by the mean values T and Ω and standard deviation values of t' and ω, respectively.

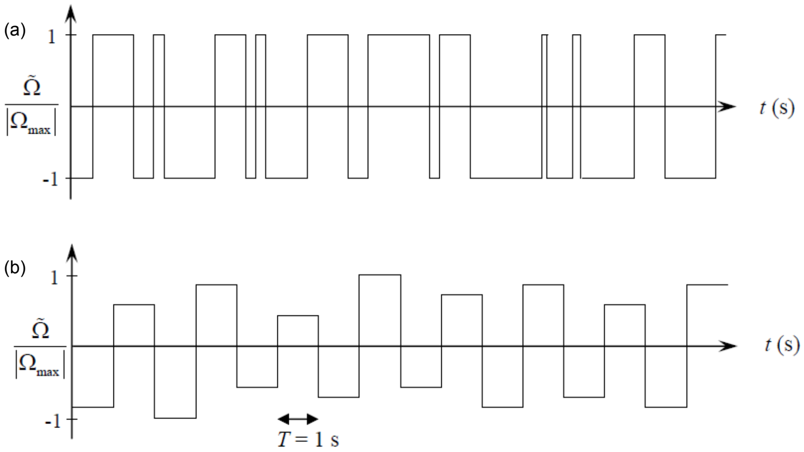

Figure 2.6: Active grid forcing schemes taken from Larssen (2005). (a) randomised cruise time scheme (b) randomised rotational speed scheme

The motor schemes implemented during this study were reproduced from similar active grid studies of Larssen (2005) and Kang et al. (2003) (Table 2.2). Three major parameters to set the operational limits of an active grid are given in Hearst and Lavoie (2012) as U_0, Ω and the wing geometry. Therefore, the cases were tested at different mean free-stream velocities, U_0, and with different wings, both solid and cut-out wings, to vary the turbulence characteristics generated by the grid.

Test case from literature	$\Omega(Hz)$	$T(sec)$	ω/Ω	t'/T
Kang et al. (2003)	5.25	1	1.75	0
Larssen and Devenport (2011), test case 14	4	1	0.5	0
Larssen and Devenport (2011), test case 15	4	1	0	0.5

Table 2.2: Operating schemes of the active grid from previous studies. Ω: mean rod rotational speed (Hz), T: mean cruise time (sec), ω/Ω: normalised maximum deviation in rotational speed, t'/T: normalised maximum deviation in cruise time.

More parameters related to the test cases will follow in Chapter 3.

2.2 Instrumentation

The experimental methods practised during this study are hot-wire anemometry, Particle Image Velocimetry (PIV) and Preston tube measurements. Details of each of the method and related experimental setup are introduced in this section.

2.2.1 Hot-Wire Anemometry

Hot-wire anemometry is a widely used measurement technique in experimental fluid mechanics. This technique is used to measure rapidly varying velocities with good spatial and time resolution (Tropea et al., 2007). The probes are available with one, two or three wires where the number of wires corresponds to the number of velocity components that can be measured.

Before any measurement, anemometer set-up should be carried out which involves setting the overheat ratio of the wire, determining the frequency response of the wire and finally setting the conditioning parameters for the signal.

A significant parameter to control the operation of the sensor is the overheat ratio which defines the relative difference in resistance given by,

$$a_w = \frac{R_w - R_a}{R_a} \tag{2.1}$$

where R_w is the sensor resistance when heated and R_a is the resistance of the unheated sensor. Typical values of a_w for air measurements range between 0.5-1.0. Beyond this range, the sensor could be permanently damaged or oxidized (Tropea et al., 2007). The overheat ratio was adjusted for the wire only once at the start of the experiment and did not need readjustment as long as the anemometer system did not need restart due to any failure like electric or the sensor related.

The output signal of a hot-wire measurement is a voltage signal; therefore, it needs to be converted to a velocity value which can be achieved through a calibration procedure. Calibration can be performed before (pre-calibration) and after (post-calibration) the measurement to compensate later for the temperature drift during the course of the measurement. Calibration of a hot-wire enables establishing a relation between the output voltage (E) of the wire and the flow velocity (U) after exposing the probe to a set of known flow velocities that are measured using a pitot static probe. This relation can be obtained either using polynomial curve fitting given by,

$$U = C_0 + C_1 E + C_2 E^2 + C_3 E^3 + C_4 E^4 \tag{2.2}$$

where C_0 to C_4 are calibration coefficients or power law curve fitting (King's law) given by,

$$E^2 = A_0 + BU^m \tag{2.3}$$

where A_0 and B are calibration coefficients and m is usually given as 0.45 in the literature as a good initial estimate for wire probes.

The temperature during calibration as well as during experiment should be recorded. Any change in temperature during measurement will cause drift in measurements but these drifts can be compensated by temperature corrections (possible correction schemes are available from either Bruun, 1995 or Hultmark and Smits, 2010). Another correction is needed to compensate the electrical drift during the long hours of experiments using the pre- and post-calibration data. It can be achieved by assuming a linear drift, i.e. the velocity measurements can be linearly interpolated between the pre- and post-calibration curves. The linear interpolation can be performed as follows for a general quantity, Q:

$$Q\left(t_i\right) = Q\left(t_{pre}\right) + \frac{Q\left(t_{post}\right) - Q\left(t_{pre}\right)}{\left(t_{post} - t_{pre}\right)}\left(t_i - t_{pre}\right) \tag{2.4}$$

where t_{pre} and t_{post} are the time at pre- and post-calibration measurements, respectively and $Q\left(t_{post}\right)$ and $Q\left(t_{pre}\right)$ are the corresponding measured quantities and t_i is the time at the measurement of the quantity, $Q\left(t_i\right)$.

Setup

The first set of hot-wire measurements were performed to measure the streamwise flow velocity in the boundary layer and in the free-stream using two single-component hot-wire anemometers. A Dantec StreamLine Pro Constant Temperature Anemometer (CTA) system was used to operate the hot-wire probes. The overheat ratio was set as 0.8 based on the definition given previously. The system had built-in signal conditioners for amplification and filtering of the CTA signal before Analogue to Digital (A/D) conversion. The output of the CTA system was low-pass filtered at 10 kHz and was sampled at a rate of 20 kHz, to prevent aliasing, by a 16-bit National Instruments USB-6212 BNC, A/D data acquisition board, connected to a PC. Simultaneous measurements with two hot-wire probes were performed: one probe was held stationary in the free-stream at 27 cm above the flat plate while the other probe was traversed over the thickness of the boundary layer and at the same streamwise location as the stationary probe, $43M$ downstream of the active grid (Figure 2.7).

The single wire traversing the boundary layer was an Auspex A55P05 boundary layer probe that had 10 mm long prongs spanned by a 3 mm long and 5 µm diameter tungsten wire with a central 1.05 mm active region shouldered on either side by copper-plated sections. The resulting length to diameter ratio was 210 following the recommendations by Ligrani and Bradshaw (1987) and Hutchins et al. (2009). Measurements of the streamwise velocity in the boundary layer were acquired at 28 wall-normal locations while the streamwise velocity in the free-stream was acquired simultaneously for a sampling period of 6 minutes.

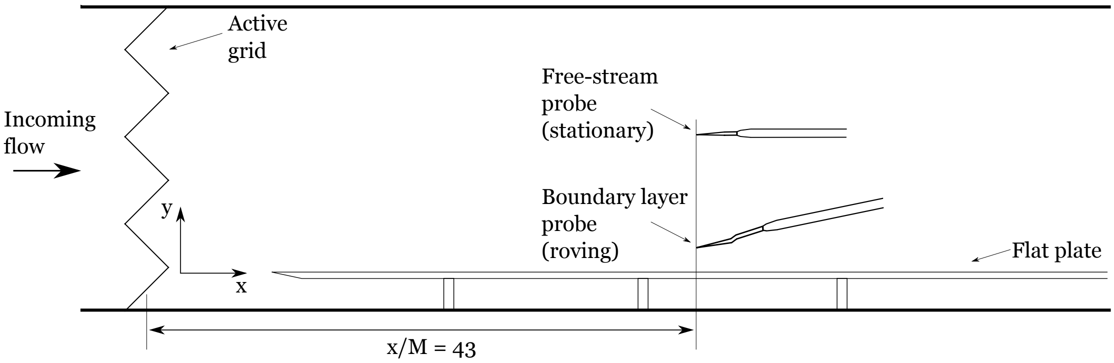

Figure 2.7: Schematic of the test section with two hot-wire probes

The motion along the wall-normal direction was achieved through a traverse system that used stepper motors that were controlled through MATLAB in the data acquisition routine. The nearest position of the hot-wire to the wall was located using a microscope camera placed on the test plate close to the wire. The probe was moved down to the wall in small steps by looking through the camera making sure that the wire did not hit the wall. When the possible closest location was achieved, an image of the wire was captured making sure that the wire had a clear shadow on the wall as parallel as possible to the wire. This was achieved using a torch directly on top of the wire making the lighting as vertical as possible. Then the wire was moved upwards with known steps and at each known step, an image was captured (Figure 2.8). Using the images, pixel-to-mm conversion was obtained since the distance covered (in steps) was known. Then the starting wall-normal position can be determined for each case. The operation of the active grid was causing the plate and the tunnel to slightly vibrate; therefore care was taken about how close the wire could get to the wall. Nonetheless, the closest distance achieved between the wire and the plate wall was ranging between 0.3-0.5 mm for different FST cases. A representative picture for wire-positioning for the first measurement location is given in the following figure for three consecutive traverse steps.

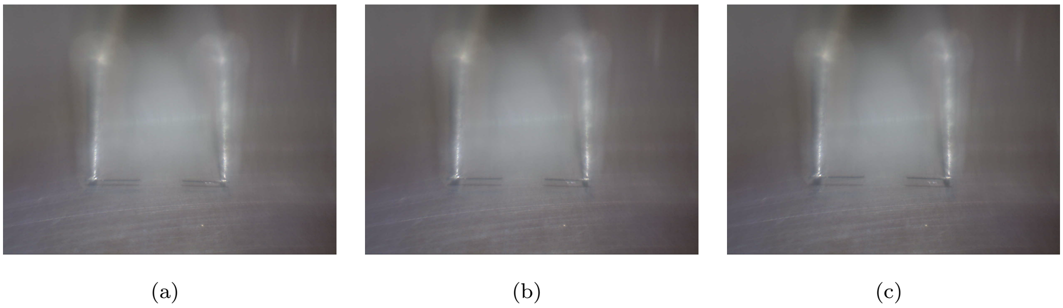
(a) (b) (c)

Figure 2.8: Wire-positioning images captured by a microscope camera. Images captured at three consecutive traverse steps: a,b and c in order of capturing.

The temperature of the free-stream was acquired by a T-type Omega thermocouple throughout the experiments. Hot-wire output signals were corrected with respect to the reference temperature during the calibration (see Bruun (1995)). The hot-wires were statically calibrated *in situ* against a reference velocity that was measured using a pitot-static tube connected to a Furness FCO510 0 - 200 Pa pressure transducer. Calibrations were performed immediately before and after each experiment. Additionally, the measurements were linearly corrected for the temperature drift between these pre- and post-calibrations. The hot-wires were calibrated while the wings of the grid were aligned with the stream direction, i.e. similar to a static mesh grid having turbulence levels of around 2-2.5%. The main reason for that was the difficulty of removing the active grid in and out of the tunnel at every time when the calibration was due. Other alternatives could be to use a calibration jet or to follow a stochastic calibration technique (Breuer, 1995), which is a technique for the calibration of the wires in turbulent flows. However, the calibration with the grid in was validated against a test with the grid removed and agreed within ±1% (Figure 2.9). Therefore, calibrations in all experiments reported were performed without removing the active grid.

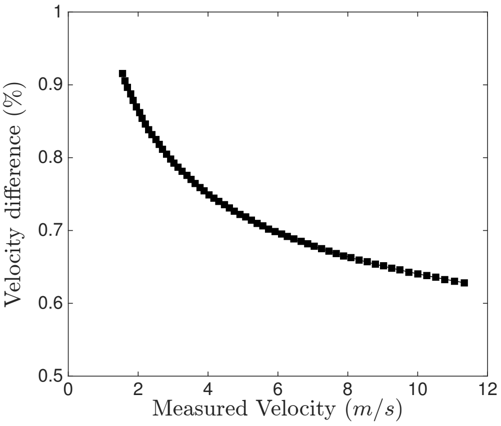

Figure 2.9: The measurement difference between the hot-wire calibrations with and without the active grid in the wind tunnel

The hot-wires were calibrated using a 14-point velocity calibration ranging between 1.4 m/s and 14 m/s. The conversion from voltage to velocity was achieved through King's law fit to the calibration points. Figure 2.10 shows a representative pre- and post-calibration of an experiment which lasted around 3 hours. Figure 2.10a shows the variation of the measured output voltage with respect to the reference velocity measured with pitot static probe. The inset, Figure 2.10b, is a close-up view of the fitted curves of pre- and post-calibrations. Here, it can be seen that the two curves are very close and there is only a slight difference between them. Figure 2.10c and Figure 2.10d show the deviation of the calibration data points from pre- and post-calibrations, respectively.

Another set of hot-wire measurements were performed to be able to measure the decaying turbulence characteristics of the grid. For this setup, a single probe was used at the same height of free-stream hot-wire measurements. The probe was moved to different streamwise locations: 5M, 11M, 22M, 33M, 43M. The data was sampled at 20 kHz for 10 minutes at each streamwise position. The calibration for these measurements were performed using a 15-point velocity calibration ranging between around 3.2 m/s to around 16.3 m/s. Temperature corrections and the linear interpolation between the pre- and post-calibrations were similarly applied.

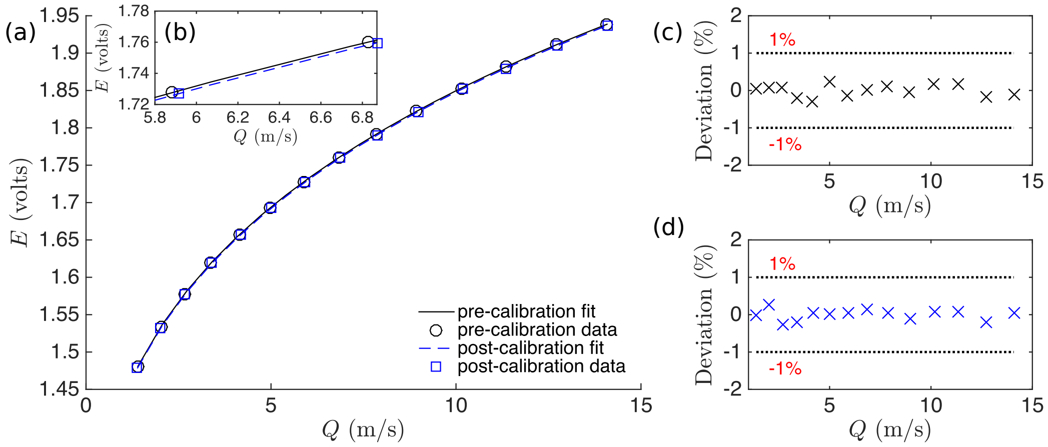

Figure 2.10: (a) Calibration curve for pre- and post-calibrations; (b) inset figure; the deviation of the data points from the fitted calibration curve for (c) pre-calibration and (d) post-calibration. Representation of data is similar to Hanson (2013)

Final set of hot-wire measurements were performed as the multi-point measurements. This set of measurements were performed long after the single-point measurements based on initial observations from these measurements. They were performed only for a small set of study cases that were deliberately duplicated from the first single-point measurements to enable the detailed investigations of the scale interactions in the turbulent boundary layer which will be discussed in Chapter 5.

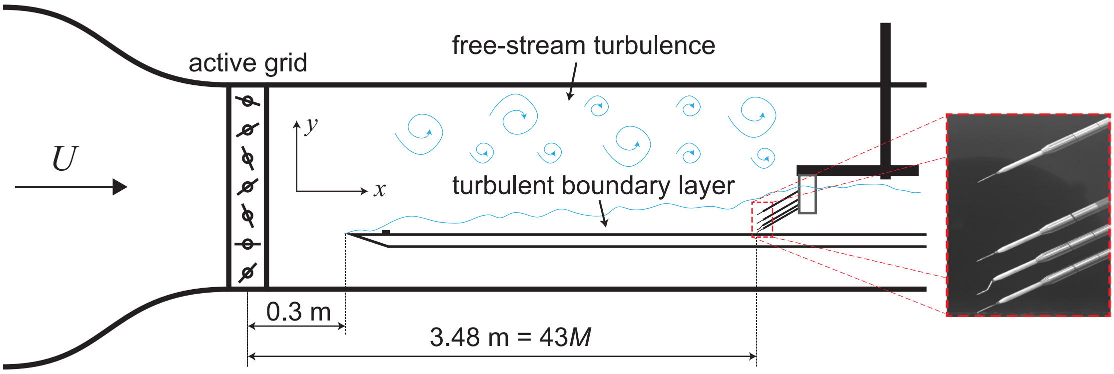

Figure 2.11: Schematic of the test section with multiple hot-wire probes (taken from Dogan et al., 2017)

For this set of measurements, four wire probes were mounted to a rake with the probes angle into the boundary layer at 30°. The second, third, and fourth wires were separated from the first by 7, 22, and 55 mm, respectively. This rake was then traversed in the wall-normal direction in the boundary layer using the traverse system over the range 0.4 mm $\leq y \leq$ 223 mm. All wires were made in-house from tungsten wire mounted to Dantec-style prongs and had a nominal sensing length of 1 mm. The second wire in the rake was a boundary layer probe in order to position it in close proximity to the first wire and all other wires were standard single-wires (see Figure 2.11). The wires were operated by a Dantec 54N82 multichannel constant temperature anemometer at an overheat of 0.8. The wires were calibrated *in situ* with 15 points fitted to a fourth-order polynomial. The linear interpolation between the pre- and post-calibrations were similarly applied. For this set of measurements, a temperature correction from Hultmark and Smits (2010) was employed. Data were acquired at 20.5 kHz for a minimum of 6 minutes, which was previously found suitable for single-point measurements to converge the relevant statistics. An analog filter was set at 10 kHz, and in post-processing the data were filtered with a fifth-order digital Butterworth filter at 7.5 kHz as it was observed that there was no meaningful signal beyond this frequency. The data were acquired with a National Instruments (NI) PXIe-1062Q 16-bit system. In particular, an NI TB-2709 card was employed because it allows for simultaneous acquisition of multiple signals with dedicated A/D converters without the need of a multiplexer, thus ensuring no phase offset between signals. As a final note, the wall-proximity of the wires was monitored using a LaVision ImagerProLX CCD 16 mega-pixel camera. The wall-offset values were determined from a calibrated image of the camera.

2.2.2 Preston Tube

Preston tube measurement is an alternative way of determining skin friction to estimating it using Clauser chart method from the mean velocity profiles of hot-wire measurements. This method makes use of a circular Pitot tube, the so-called Preston tube, resting on the wall. The pressure difference is measured between two tubes: one (Preston tube) is placed in contact with the wall and open to the oncoming flow and the other is a static pressure port drilled through the surface of the plate. The measurements depend on the assumption of the validity of the log-law (Patel, 1965). This method needs calibration that involves relating friction velocities derived from log-law to the difference between the total pressure measured by Preston tube and the static pressure measured from the static port.

The wall thickness of the tube determines which portion of the mean profile contributes to the stagnation pressure sensed at the tube opening (Tropea et al., 2007). For most of the measurements, the finite wall thickness of a typical tube will result in the location of tube opening being in the logarithmic portion of the mean profile and most of the Preston tube calibrations have been devised for such cases. Most common calibrations are given by Patel (1965). A new calibration can be performed by measuring boundary layer profiles for a range of velocities and devising a relation between the Preston tube readings to the skin friction velocity values obtained by Clauser method based on the initial assumption that the Preston method assumes the validity of the log-law.

Setup

The diameters of Preston tubes were chosen based on initial estimates using Patel's calibration. In Patel (1965), different calibrations are given for different $y*$ intervals where $y* = \log\left(\frac{\tau d^2}{4\rho\nu^2}\right)$ where d is tube diameter. From Figure 2.12, it can be seen that a calibration corresponding to the interval of $1.5 < y^* < 3.5$ is suitable for tested tubes with diameters of 1.83 mm, 2.4 mm and 2.76 mm to obtain the skin friction velocity values of the two representative cases (red dashed lines) which demonstrate the extreme values that could be encountered during the experiments. Any other cases would remain between these two extreme values and therefore they are assumed to be satisfied by the chosen calibration interval using these specified tubes. It was decided to use both 1.83 mm and 2.76 mm diameter tubes to perform simultaneous measurements that would allow to compare the effect of different tube diameters on measurements.

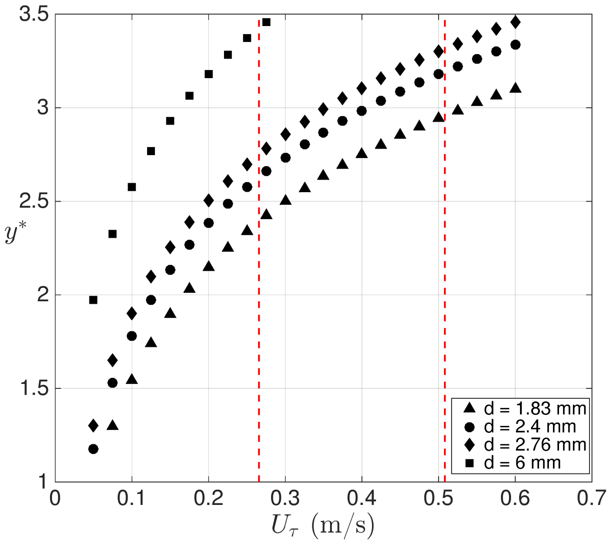

Figure 2.12: Variation of y^* with the skin friction velocity, U_τ, for different tube diameters, d. Red dashed lines are for extreme values of the study cases.

The Preston tube setup is given in Figure 2.13. Each Preston tube was given a minor curvature and fixed with tape at the centre of its 15 cm length to ensure that the tube opening was in contact with the plate at all times.

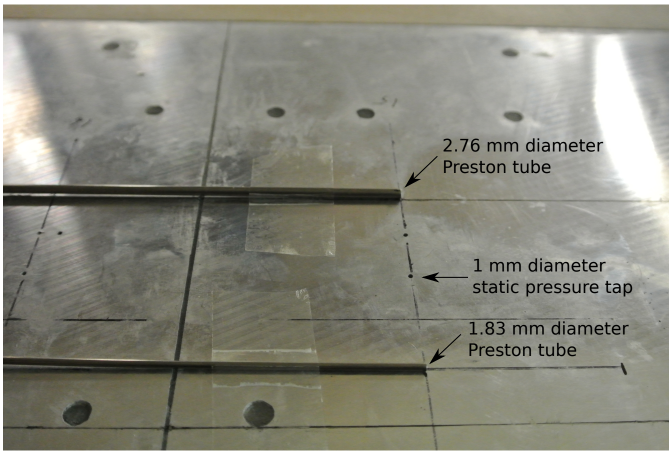

Figure 2.13: Preston tubes on the flat plate, aligned with the static tap.

A new calibration was also performed for Preston measurements as an alternative to Patel's calibration. For that, as mentioned previously, boundary layer profiles for no-FST case, the baseline case without the presence of the active grid, were obtained at various velocities and then the skin friction velocity was estimated using Clauser chart method and a calibration between the skin friction velocity and the pressure difference (between the Preston tube and the static tap) was devised. Figure 2.14 shows the alternative calibration fit based on skin friction velocity results from Clauser method in comparison with the skin friction velocity results obtained by Patel's calibration.

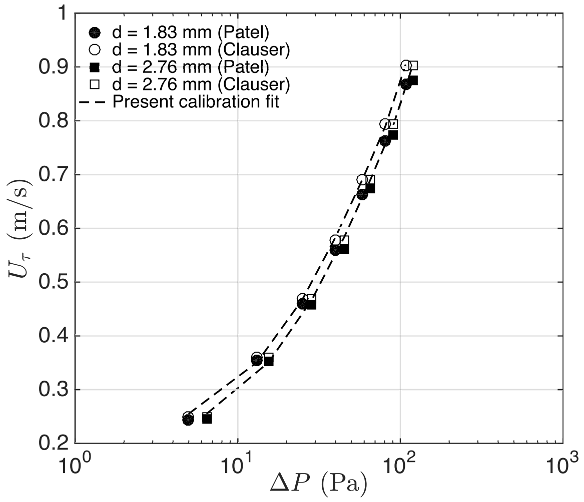

Figure 2.14: Comparison of skin friction velocity values obtained through Patel's calibration and the alternative calibration fit of the present study.

The calibration fit obtained for present cases seems compatible with Patel's calibration. It can also be deduced from the figure that different tube diameters affect the measurements differently. As the pressure difference (ΔP) increases, the difference in results from the two different diameter tubes decreases. This could be explained by the fact that for low ΔP cases, the boundary layer thickness is larger and therefore the tube opening of smaller diameter might not well be in the logarithmic region.

The results from Preston tube can be verified through the relation given by Fernholz and Finley (1996) for an incompressible zero-pressure-gradient turbulent boundary layer. They relate skin friction coefficient with momentum thickness based Reynolds number, $Re_\theta = U_0\theta/\nu$. Figure 2.15 compares this relation with the present Preston measurements for a single tube diameter (2.76 mm) based on two different calibrations. The results show a good match for both calibrations in relation to their correlation. Throughout the study, skin friction velocity values were presented from the 2.76 mm diameter Preston tube and were calculated based on the performed calibration fit. The results from Preston tube were also validated by oil film interferometry measurements which were carried out later under the same conditions during a master degree project by Luis Blay Esteban (Esteban, 2015) who was mentored by the author.

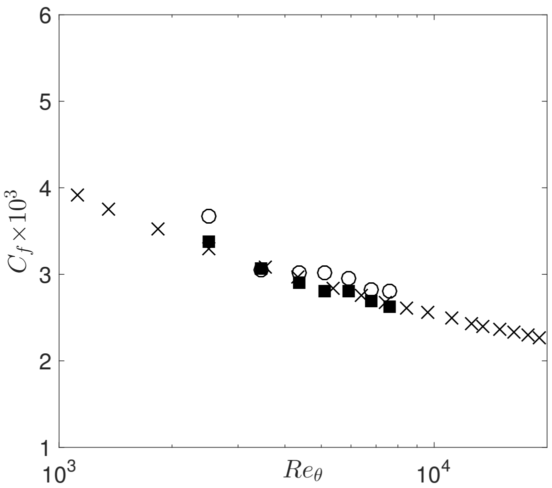

Figure 2.15: Variation of skin friction coefficient, C_f, with Re_θ. Filled symbols: data based on Patel's calibration, open symbols: data based on present calibration, × : Fernholz and Finley (1996) correlation

2.2.3 Particle Image Velocimetry

Particle Image Velocimetry (PIV) is used to perform instantaneous measurements of the velocity over a whole flow domain simultaneously that makes visualisation and quantification of the instantaneous flow organisation, also known as coherent structures, possible. The working principle of PIV is based on measuring the displacement of fluid during a short time interval. The position of the fluid is imaged through the light scattered by tracer particles seeded in the flow that are illuminated by a laser sheet. These particles are sufficiently small and light to move with the local flow velocity and they do not change the fluid properties or flow characteristics. The details of the working principle and the components of the technique can be found in Adrian and Westerweel (2011) and Tropea et al. (2007).

Setup

Planar PIV measurements were performed for this study. These measurements aimed to investigate the instantaneous spatial features of the turbulent boundary layer in the presence of FST. Three LaVision ImagerProLX CCD 16 mega-pixel cameras fitted with Nikon Nikkor lenses with a focal length of 200 mm at an f-stop (aperture) of 8. The cameras were oriented in a T-shaped formation (see Figure 2.16(a)) to acquire both the boundary layer and the free-stream with field of view of each camera overlapping by 1 cm. The measurement plane started at about 3.2 m downstream of the mid-plane of the active grid. The field of view was about 32 cm × 27 cm. The laser sheet was generated by a Litron Lasers Nano L200 15PIV Nd:YAG laser (532 nm wavelength, 200 mJ/pulse, 15 Hz repetition rate). The circular beam through the laser was focused using a spherical lens of focal length 1.0 m and subsequently passed through two cylindrical lenses with focal length -15 and -30 mm, the former being right after the spherical lens, that spread the beam into a sheet. The laser sheet formed illuminated a streamwise-wall-normal plane perpendicular to the test plate (see Figure 2.16(b)). The flow was seeded with particles of a glycol and de-mineralised water solution (Pro Smoke Super fluid from Martin). In total 2000 images were acquired and then were processed with LaVision DaVis 8.2.2. Care was taken throughout processing to mitigate the effects of pixel-locking which has been previously identified as having an adverse influence on the interpretation of the underlying physics from PIV measurements (Christensen, 2004). The algorithm developed by Hearst and Ganapathisubramani (2015) has been implemented on the cases investigated in detail in this study. The images were pre-processed by first applying a sliding background subtraction filter to reduce noise, and then applying a 3 × 3 Gaussian kernel filter to slightly blur the particles over more pixels; the latter helps to reduce the influence of pixel-locking. The vector fields were then computed using 50% overlap and five passes reducing from 96 pixels × 96 pixels windows to 16 pixels × 16 pixels windows. Window deformation was used on final passes to mitigate pixel-locking. Finally, the vectors were post-processed by applying histogram equalisation on a vector-by-vector basis as described by Hearst and Ganapathisubramani (2015) to further diminish the influence of pixel-locking.

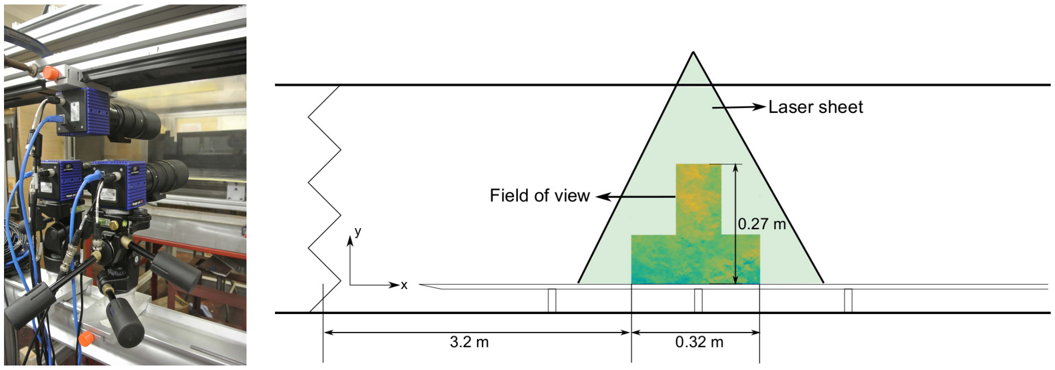

(a) (b)

Figure 2.16: (a) Camera setup (b) Laser alignment and the resulting field of view (not to scale)

2.3 Measurement Uncertainties

Although care was taken to reduce the uncertainties associated with the measurement techniques used throughout the course of the study, no measurement can be completely free of uncertainties. Therefore, it is important to quantify uncertainty estimates to strengthen the credibility of a measurement. In this section, the elements for uncertainties will be presented for each measurement technique.

2.3.1 In hot-wire measurements

The methodology in Jørgensen (2002) was followed to estimate the uncertainties for hot-wire measurements. The sources of error for these measurements and their estimated values are presented in Table 2.3. All the uncertainty estimates take into account the coverage factor of their corresponding error distributions with a confidence level of 95%.

Source of error	Uncertainty (±%)
Calibration and Linearisation	0.9
A/D resolution	0.03
Probe positioning	~0
Temperature change	0.2
Ambient pressure change	0.56
Humidity	~0
Total	1.1

Table 2.3: Error sources and uncertainties for a single velocity sample acquired with a single hot-wire.

The main uncertainty in hot-wire measurements is associated with the uncertainty in calibration and linearisation as suggested by Jørgensen (2002). The calibration uncertainty is a function of the uncertainty of the measured variables and the fitting error of the calibration curve. The total calibration error, δ_c, can be written in components following a similar procedure as in Hanson (2013),

$$\delta_c = \sqrt{{\delta_f}^2 + {\delta_r}^2 + {\delta_d}^2} \tag{2.5}$$

where δ_f is the data fitting error, δ_r is the error associated with the reference velocity obtained by the pitot-static tube and the drift error, δ_d. All these errors are assumed to be independent and therefore are added up quadratically based on the propagation principle of the random independent errors (Taylor, 1997).

For the data fitting error, δ_f, it is essential to calculate the standard deviation of the curve fit to the measured data points. This can be quantified as

$$\sigma = \sqrt{\frac{1}{s-3}\sum_{i=1}^{s}(Q_i - Q_c(E_i))^2} \tag{2.6}$$

where Q_i and E_i are the measured velocity and voltage at the calibration point i, respectively and Q_c is the velocity value obtained from King's Law for the corresponding E_i. The term $s-3$ is included since King's Law required fitting three variables (refer to Equation 2.3). When the calibration fitting method was chosen as the polynomial curve fitting, this would be $s-5$; however, it would not change the error considerably. Using the data shown in Figure 2.10, it is found that $\delta_f/Q = \pm 0.36\%$.

The error associated with the reference velocity measurement, δ_r, is dependent on the errors in the pressure difference, $\delta_{\Delta p}$ and the density, δ_ρ, based on Bernoulli's relation,

$$Q = \sqrt{\frac{2\Delta p}{\rho}} \tag{2.7}$$

From the specifications of the manometer, $\delta_{\Delta p}$ is known as ±0.25% of the reading. The error in density, δ_ρ, is dependent on the errors in ambient temperature and pressure assuming air is an ideal gas. The individual errors for ambient temperature and pressure (refer Table 2.3) could be added up quadratically to obtain δ_ρ as 0.6%. With these components, δ_r can be stated as 0.65%.

The drift error, δ_d, is related to the difference in pre- and post-calibration data fits and this is calculated using the data in Figure 2.10 as 0.5%.

Finally, the total calibration error can be determined using Equation 2.5 as 0.9%.

The second source of error in hot-wire measurements is the A/D resolution which is dependent on the input voltage range ±5V and the DAQ resolution, 16-bit. Probe positioning, which is related to the alignment of the probe after the calibration, might also cause errors. Pre- and post-calibrations were performed *in-situ* to minimise and almost eliminate that effect. Temperature variations between a calibration and the measurement and during the course of the measurement also introduce systematic errors. Although a maximum of ±1 degree Celsius change has been observed in ambient temperature during the measurements, a temperature correction scheme was always applied to minimise these errors. The ambient pressure change also influences the density and therefore adds up to the uncertainty in the calculated velocity. The maximum change was detected to be less than 2 kPa during the measurements. Final factor affecting the uncertainty of hot-wire measurements as presented in Jørgensen (2002) is the humidity which was suggested to have negligible effects on the measurements. All these uncertainties are assumed to be independent and therefore are added up quadratically (Taylor, 1997) and the overall uncertainty in hot-wire measurements can be stated as 1.1%.

2.3.2 In Preston tube measurements

Alignment of the Preston tube in the flow direction can be a significant source of error. Extreme care was given for this as can also be inferred from the setup picture (Figure 2.13). Despite that, errors in Preston tube measurements of about 1% are suggested for a misalignment of about 3°. In addition, similar to the hot-wire calibration curve fitting uncertainty, Preston tube measurements are also prone to uncertainties in calibration.

Patel (1965) reported ±1.5% error in their curve fit of the calibration. Since the calibration fit matched Patel's calibration, similar uncertainty values can be reported. The total uncertainty in Preston tube measurements, i.e. when the independent factors add up quadratically, is found as less than 2%.

2.3.3 In PIV measurements

The bias errors in PIV are related to the inadequacy of the statistical method of cross-correlation in the evaluation of a PIV image (Raffel et al., 2007). They can also occur when the particle image diameter is on the order of one pixel or less also known as the pixel-locking phenomenon. There are also other factors in PIV to cause random errors like camera noise, background illumination, seeding density inhomogeneity, out-of plane particle motion and many others (Adrian and Westerweel, 2011). Here, the contributions of each factor will not be quantified in detail as it is not the aim of this study. However, for an estimation of the uncertainty in PIV measurements, an uncertainty in the order of 0.05 pixels is cited based on the study by Sciacchitano et al. (2015) who performed a comparative assessment of different uncertainty quantification for PIV data. This corresponds to an uncertainty in the instantaneous velocity of around 0.07 m/s. They also stated that the accuracy of the estimated uncertainty is observed to reduce by 10% in the presence of pixel-locking. Therefore, Hearst and Ganapathisubramani (2015) suggested a quantification metric that could be potentially integrated to the local uncertainty estimates in Sciacchitano et al. (2015). As mentioned previously, the algorithm from Hearst and Ganapathisubramani (2015) has been implemented on the cases investigated in detail in this study to alleviate the effects of pixel-locking.

Chapter 3

Mean flow and bulk properties

3.1 Introduction

This chapter presents mean velocities and bulk characteristics of the flow for different FST conditions obtained from hot-wire measurements, the details of which have already been given. The free-stream is characterised by using the stationary single wire and the mean flow characteristics of the boundary layer are determined from the traversing single wire.

The FST cases were generated using the active grid by rotating the shafts at specified rotation rates during specified periods. Two different sets of wings, i.e. solid wings and cut-out wings, were used as described previously to achieve a range of turbulence intensity values from approximately 7% to 13%. The motor schemes of the active grid were reproduced from various active grid studies in the literature (Kang et al., 2003; Larssen and Devenport, 2011). A total of 20 FST cases are documented in this study. Detailed analysis is generally limited to only four cases because the phenomena of interest to this study can be adequately described from this reduced set. However, trends determined from 20 cases are also included when broader points are made.

3.2 FST conditions

The four FST cases investigated in detail were generated by reproducing the operation schemes from Larssen and Devenport (2011) (test case 14 in their study). It involves setting a uniformly distributed rotational speed in the range of 2-6 Hz for each rod's motor once every second while adjacent motors rotate in the opposite direction. The characteristics of these four FST cases are summarised in Table 3.1. Using the solid or reduced blockage sets of wings mainly resulted in different levels of turbulence intensity. Cases A and B were generated using cut-out wings resulting in what will be referred to as “low-range” turbulence intensity levels around $7-8\%$. Cases C and D were generated using solid wings resulting in what will similarly be referred to as “high-range” turbulence intensity levels around $12-13\%$. The parameters are obtained from the measurements acquired at $43M$ downstream of the grid. The subscript 0 is used to denote the free-stream values as mentioned before. Quantities with this subscript were obtained from the stationary probe in the free-stream from the single-wire measurements as described previously. The instantaneous velocity in the streamwise direction is denoted by the sum of the mean and fluctuating components, $U+u$. Reynolds number, Re_{λ_0}, based on the Taylor micro-scale, λ_0, is defined as $\sqrt{\overline{u_0^2}}\lambda_0/\nu$ where λ_0 is calculated as $\sqrt{\left(15\nu\overline{u_0^2}/\epsilon\right)}$. Within this definition, the turbulence energy dissipation rate, ϵ, is calculated from the spatial gradient of the streamwise velocity fluctuations as $15\nu\overline{\left(\partial u_0/\partial x\right)^2}$, the formulation of which invokes Taylor’s hypothesis to obtain the spatial gradient from the temporal gradient calculated from the hot-wire measurements. To improve the estimate of the gradient quantities in a turbulent flow from hot-wire measurements, higher order differencing schemes are suggested (Hearst et al., 2012); therefore 7-point centred differencing schemes were employed in this study to calculate the velocity gradients. Using the dissipation rate, ϵ, Kolmogorov scale (η_0), can be calculated from $\left(\nu^3/\epsilon\right)^{1/4}$. There are several ways to define the integral length scale (L_0) in a turbulent flow. A common definition is to use the value of the integrated normalised autocorrelation to the first zero crossing. However, it was found that the low frequency energy content caused by the active grid prevented the autocorrelation from reaching zero. For this reason a value of 0.1 was chosen in the present study to determine the extent of the integration region, which was above the asymptotic limit reached in all cases. Another common method to calculate the integral length scale often used in active grid studies is from the wavenumber at which the pre-multiplied spectra peaks. Since this method is associated with significant scatter, Mydlarski and Warhaft (1996) introduced the relation, $L_0^* = 0.9\overline{u_0^2}/\epsilon$. The integral length scale using each of the aforementioned methods is included in Table 3.1 for comparison purposes. As will become clear later, this study is particularly interested in the most energetic free-stream scales, which differ from the tabulated integral length scales.

The decay of turbulence downstream of a grid is governed by a power law as $\overline{u_0^2}/U_0^2 = D(x/M)^n$ as given in Mydlarski and Warhaft (1996). For each of the four cases described in Table 3.1, Figure 3.1 shows the decay of the variance of streamwise velocity fluctuations, $\overline{u_0^2}$. The measurements were performed along the test section midway between the test-section ceiling and the measurement side of the plate from approximately $x/M = 5$ until the fixed downstream location for the boundary layer profiles, $x/M = 43$, as described previously. For these cases, an exponent of $n = -1.25$ adequately describes the observed decay shown in this figure. This value is consistent with similar active grid studies from the literature (Mydlarski and Warhaft, 1996; Kang et al., 2003). The vertical shift in Figure 3.1 between two different sets of lines, i.e. different constants

FST cases	$U_0(m/s)$	$\sqrt{\overline{u_0^2}}/U_0(\%)$	Re_{λ_0}	L_0/M	L_0^*/M	$\lambda_0(mm)$	$\eta_0(mm)$
A (△)	6.1	7.4	315	2.1	5.6	10.8	0.3
B (◆)	10.1	8.3	505	2.8	4.2	9.4	0.2
C (▶)	8.0	12.1	530	2.7	3.4	8.4	0.2
D (■)	9.9	12.7	645	3.0	3.0	7.9	0.2

Table 3.1: Free-stream parameters for the study cases at $x = 43M$. U_0: mean streamwise velocity, $\sqrt{\overline{u_0^2}}/U_0$ (%): turbulence intensity, $Re_{\lambda 0}$: Reynolds number based on the Taylor micro-scale, L_0/M and L_0^*/M: integral length scale ratio based on M, λ_0: Taylor micro-scale, η_0: Kolmogorov scale. Detailed definitions of the parameters are given in the text.

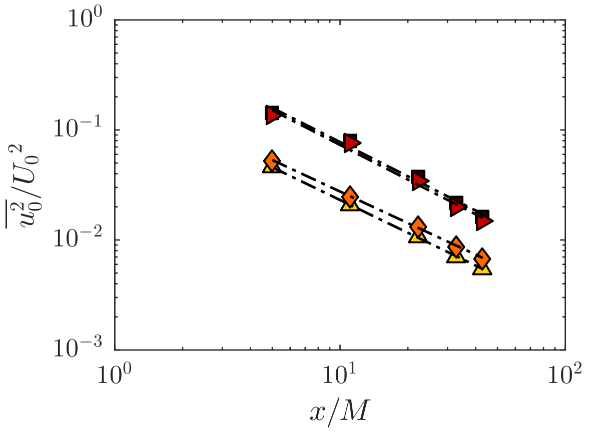

Figure 3.1: Decay of the normalised variance of the streamwise velocity fluctuations for the FST cases. (△): case A, (◆): case B, (▶): case C and (■): case D.

of D in the power-law equation, is caused by the solidity, i.e. the open area ratio, of the grid. Regardless, it can be deduced that the decay of turbulence is similar for each of the different FST cases. This suggests that the similarities and/or differences between different boundary layer cases presented in this study is not related to the rate of turbulence decay.

At the downstream location of the boundary layer profiles, $43M$, Figure 3.2 shows the pre-multiplied energy spectra of the streamwise velocity fluctuations in the free-stream normalised by the local free-stream variance, $k_x\phi_{uu}/\overline{u_0^2}$, with the streamwise wavelength, ζ_x, normalised by the grid mesh length, M, for the FST cases. The non-dimensional spectra are similar for each case and exhibit significant collapse. The characteristic wavelength of the spectral peak occurs at approximately $20M$, which is several times longer than the integral length scales given in Table 3.1. Given that the length scale of approximately $20M$ represents the most energetic scale, it is also chosen as the representative scale of turbulence in the free-stream.

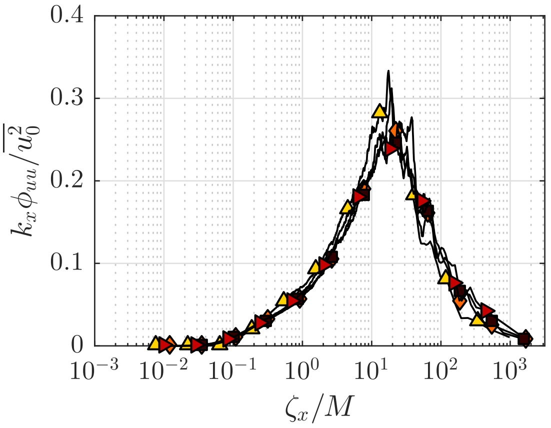

Figure 3.2: Normalised pre-multiplied energy spectra of streamwise velocity fluctuations, $k_x\phi_{uu}/\overline{u_0^2}$, of the free-stream for the FST cases with streamwise wavelength, ζ_x, of the free-stream with respect to grid mesh length, M. (▲): case A, (◆): case B, (▶): case C and (■): case D.

3.3 Boundary layer characteristics

A zero-pressure-gradient turbulent boundary layer was established under the influence of FST on a smooth flat plate as described previously in Chapter 2. Herein, the characteristics of the turbulent boundary layers developed under the influence of different FST conditions will be discussed. In addition, in the instances where comparison is possible they will be presented together with the baseline case taken without the presence of the active grid, which will be referred to as “no-FST”.

Table 3.2 is a summary of the turbulent boundary layer parameters for the no-FST case and for the four FST cases detailed in this study. This table is an extension of Table 3.1 for the parameters of the boundary layers developed under the effect of the corresponding FST cases. The definition of each of the parameters presented in this table are given in the following paragraphs.

There are several common approaches to define the thickness of the boundary layer. A common method is to report this thickness as the height at which the mean streamwise velocity in the boundary layer is equal to a fraction of the mean free-stream velocity, such as δ_{95}, δ_{99} or δ_{995}, corresponding to the height where the mean free-stream velocity reaches 95%, 99% or 99.5% of U_0, respectively. However, high fluctuations in the free-stream due to the presence of the grid resulted in a wide scatter around the mean free-stream velocity which could lead to the uncertainty associated with identifying the boundary layer thickness using these definitions. For this reason the boundary layer thickness, δ was defined using an integral method, which was found to be a more robust method for this study. The boundary layer thickness is calculated using the iterative integral method given by Perry and Li (1990) as $\delta = \delta^* U_0/(C_1 U_\tau)$ where δ^* is the displacement thickness, $\delta^* = \int_0^\infty \left(1 - \frac{U}{U_0}\right) dy$, $C_1 = \int_0^1 \left(\frac{U_0 - U}{U_\tau}\right) d\frac{y}{\delta}$ and U_τ is the skin

Cases	$U_0(m/s)$	$\sqrt{u_0^2}/U_0(\%)$	$\delta(m)$	β	Π	$U_\tau(m/s)$	Re_τ	Re_θ	Re_x
No-FST (▽)	10.1	0.6	0.05	-	0.55	0.39	1330	3830	2.2×10^6
A (▲)	6.1	7.4	0.11	1.1	-0.26	0.27	1960	2760	1.5×10^6
B (◆)	10.1	8.3	0.13	1.3	-0.26	0.41	3450	4870	2.3×10^6
C (▶)	8.0	12.1	0.16	5.0	-0.44	0.34	3670	4360	1.8×10^6
D (■)	9.9	12.7	0.17	4.9	-0.52	0.42	4720	5590	2.3×10^6

Table 3.2: Turbulent boundary layer parameters for FST cases at $x = 43M$, with the baseline no-FST case. U_0: mean streamwise velocity of the free-stream, $\sqrt{u_0^2}/U_0$ (%): free-stream turbulence intensity, δ: boundary layer thickness, β: Hancock and Bradshaw (1983) FST parameter, Π: Coles wake parameter, U_τ: skin friction velocity, Re_τ: Reynolds number based on skin friction velocity, Re_θ: Reynolds number based on momentum thickness, Re_x: Reynolds number based on streamwise distance, x. Detailed definitions of the parameters are given in the text.

friction velocity obtained from Preston tube measurements. For a canonical boundary layer, this method results in typically 20% higher δ values than that defined using δ_{99} (Perry and Li, 1990). Hancock and Bradshaw (1983) introduced the FST parameter, β, defined as $(\sqrt{u_0^2}/U_0)/(L_e/\delta_{995}+2)$ where the turbulence intensity $(\sqrt{u_0^2}/U_0)$ is given as a percentage and L_e is a turbulence length scale defined from the decay power law of the grid turbulence (Castro, 1984). The purpose of this parameter is to account for the overall effect of FST by including the level of the turbulence and the characteristic length scale. Hancock and Bradshaw (1983) had a β range of 0.62 to 1.72, Thole and Bogard (1996) had a range of 2 to 4.6 and Sharp et al. (2009) presented results with β values of 1.5 and 2.3. It should be noted that Thole and Bogard (1996) used the δ_{99} definition instead of δ_{995} for the boundary layer thickness. Likewise, the present study invokes a different definition of the thickness, i.e. δ definition given above, to calculate β values presented in Table 3.2. The next tabulated parameter Π values represent the Coles wake parameter as defined by Coles (1956). Finally, the momentum thickness $(\theta = \int_0^\infty \frac{U}{U_0}\left(1-\frac{U}{U_0}\right)dy)$, skin-friction velocity and streamwise distance (x) based Reynolds numbers are given in Table 3.2 as $Re_\theta = U_0\theta/\nu$, $Re_\tau = U_\tau\delta/\nu$ and $Re_x = U_0 x/\nu$, respectively.

As mentioned previously, the inclusive dataset with the corresponding parameters defined for Table 3.1 and Table 3.2 are presented in Table 3.3.

FST Cases	Motor Scheme	$U_0(m/s)$	$\sqrt{\overline{u_0^2}}/U_0(\%)$	$Re_{\lambda 0}$	L_e/δ	$\delta(m)$	β	H	$U_\tau(m/s)$	Re_τ	Re_θ	Re_x
+	R1	12.2	8.5	610	3.5	0.13	1.4	1.19	0.5	4300	5840	2.7×10^6
✳	R3	8.1	7.7	390	4.7	0.13	1.0	1.22	0.33	2830	3840	1.8×10^6
☆	R1	10.2	8.2	510	2.7	0.15	1.6	1.19	0.42	4080	5120	2.3×10^6
✡	R2	12.2	8.5	610	2.5	0.15	1.7	1.18	0.5	4700	6000	2.7×10^6
⟐	R2	8.1	7.8	410	4.7	0.11	1.0	1.22	0.33	2480	3540	1.8×10^6
⊙	R3	6.1	7.2	300	4.9	0.12	1.0	1.24	0.27	2120	2910	1.3×10^6
⊡	R1	8.2	7.9	410	4.0	0.13	1.1	1.22	0.34	2830	3770	1.8×10^6
⟠	R1	6.1	7.3	320	3.6	0.12	1.2	1.25	0.27	2045	2710	1.4×10^6
⊕	R3	9.8	12.4	600	0.7	0.13	4.4	1.19	0.41	3440	4330	2.2×10^6
⊞	R3	6.0	11.1	400	0.6	0.15	4.1	1.19	0.27	2670	3400	1.3×10^6
◈	R2	6.0	11.3	410	0.4	0.20	4.6	1.18	0.28	3550	3945	1.3×10^6
⊗	R1	11.6	13.0	750	0.5	0.18	5.0	1.16	0.49	5820	7470	2.6×10^6
⊠	R1	8.1	12.1	530	0.3	0.2	5.1	1.17	0.35	4645	5210	1.8×10^6
⊛	R1	6.0	11.3	400	0.3	0.17	4.8	1.18	0.27	3050	3855	1.3×10^6
⧆	R3	8.0	11.9	510	0.5	0.18	4.4	1.17	0.34	4050	4920	1.8×10^6
◬	R2	11.6	13.0	760	0.4	0.2	5.2	1.16	0.49	6450	7620	2.6×10^6

Table 3.3: Free-stream and boundary layer parameters for FST cases apart from cases A-D. The measurements were performed at $43M$ downstream of the active grid. Cases from (+) to (⟠) were generated by using cut-out wings. Cases from (⊕) to (◬) were generated by using solid-wings. Motor schemes reproduced from R1: Kang et al. (2003); R2: Larssen and Devenport (2011) (test case 14) and R3: Larssen and Devenport (2011) (test case 15). U_0: mean streamwise velocity of the free-stream, $\sqrt{\overline{u_0^2}}/U_0(\%)$: turbulence intensity of the free-stream, $Re_{\lambda 0}$: Reynolds number based on Taylor micro-scale, L_e/δ: turbulence length scale ratio defined by Hancock and Bradshaw (1983), δ: boundary layer thickness, β: FST parameter defined by Hancock and Bradshaw (1983), U_τ: skin friction velocity, Re_τ: Reynolds number based on skin friction velocity, Re_θ: Reynolds number based on momentum thickness, Re_x: Reynolds number based on streamwise distance, x.

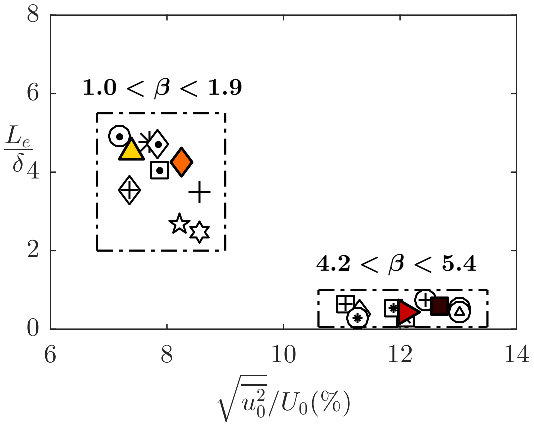

Figure 3.3: Turbulence length scale ratio defined by Hancock and Bradshaw (1983) with FST turbulence level. (▲) case A; (◆) case B; (▶) case C; (■) case D. Conditions of the cases for all other data markers are found in table 3.3.

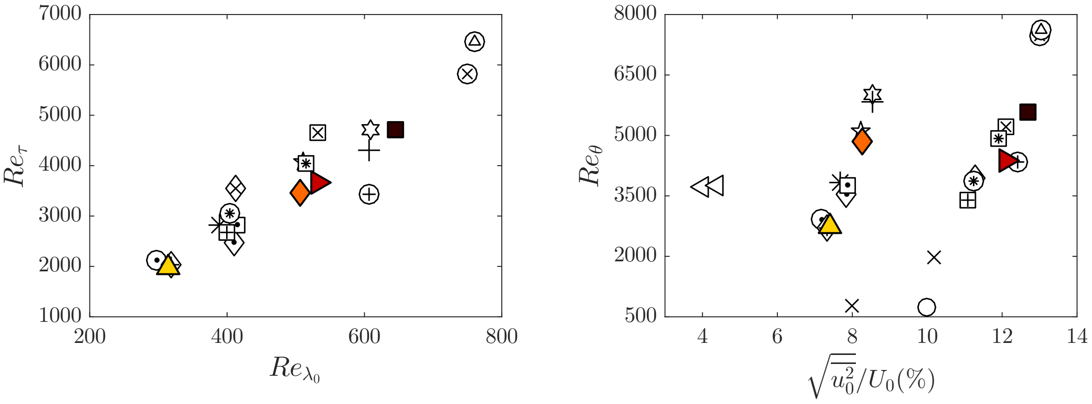

(a)

(b)

Figure 3.4: Parameter range. (a) Re_τ vs Re_{λ_0}; (b) Re_θ vs turbulence intensity level ($\sqrt{\overline{u_0^2}}/U_0(\%)$). (▲) case A; (◆) case B; (▶) case C; (■) case D. Previous studies plotted in (b): (◁) Hancock and Bradshaw (1983), (○) Thole and Bogard (1996), (×) Sharp et al. (2009). Conditions of the cases for all other data markers are found in table 3.3.

A length scale ratio (L_e/δ), originally proposed by Hancock and Bradshaw (1983) (albeit using δ_{995}) is defined for the FST cases. Figure 3.3 shows this length scale ratio with respect to the free-stream turbulence intensity. This plot and subsequent parameter plots are populated with the inclusive dataset summarised by tables 3.2 and 3.3 to reveal the trends (or lack of) between the relevant parameters. Referring back to Figure 3.3, the cases can be grouped in two different β ranges, which is mainly dependent on the wing type used. The four cases given in Table 3.2 are chosen to be representative of these two distinct groups.

The extent of the parameter domain for Re_{λ_0}, Re_τ and Re_θ is shown in Figure 3.4. Referring to Figure 3.4(a), Re_τ appears to linearly increase with Re_{λ_0}. It must be noted that although a distributed range of Re_{λ_0} have been obtained in the experiments, the range of turbulence intensities that were achieved is more clustered. This is primarily because the turbulence intensity values were related to the solidity of the wings of the active grid, as previously discussed. However, the variation of the Taylor micro-scale appears to be dependent on the actuation scheme of the active grid. Regardless, the approximate linear relationship between Re_{λ_0} and Re_τ is reasonably clear from this figure. The four cases chosen for this paper (Table 3.2) also well manifest this linear relationship. It should also be noted that Re_τ range covered for the present study is not as wide as desired. Figure 3.4(b) shows the relationship between turbulence intensity of the free-stream ($\sqrt{\overline{u_0^2}}/U_0(\%)$) and Re_θ. This figure shows that for each of the low- and high-range FST groups, Re_θ increases with the level of FST. However, comparing the two different groups, a similar range of Re_θ is observed although the level of FST is markedly different. This suggests that similar boundary layer characteristics may be developed under the effect of different FST levels and characteristics, which is further supported by the inclusion of several relevant examples from the literature. It can also be seen that the present study achieves higher Re_θ values with higher turbulence levels compared to those previous studies.

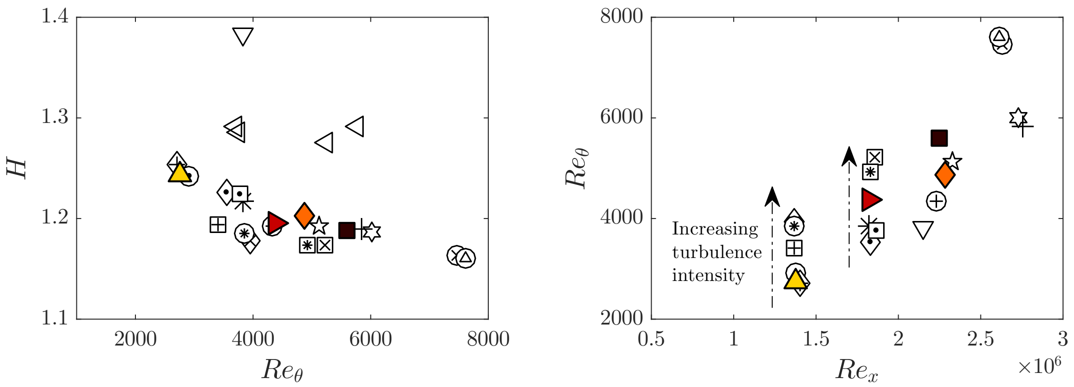

(a)

(b)

Figure 3.5: Development of boundary layer parameters. (a) Shape factor (H) with Re_θ; (b) Re_θ with Re_x. (△) case A; (◆) case B; (▶) case C; (■) case D. No-FST case (▽) and relevant data from Hancock and Bradshaw (1983) (◁) are also plotted in (a). Conditions of the cases for all other data markers are found in Table 3.3.

The shape factor, $H = \delta^*/\theta$, is in relevance to the evolution of the boundary layer and is a measure of the "fullness" of the boundary layer. Due to penetration of FST and therefore mixing in the boundary layer, there is higher momentum flux towards the wall and this increases the fullness of the velocity profile. That in turn means a decrease in the shape factor, H, as also shown in various previous studies (Hancock and Bradshaw, 1983; Castro, 1984; Stefes and Fernholz, 2004; Brzek et al., 2009). This is demonstrated in Figure 3.5(a), which shows that the shape factor is reduced by the presence of FST in comparison to the no-FST case, which exhibits a typical value of around 1.4 for a turbulent boundary layer. Furthermore, the high-range turbulence intensity cases, i.e. cases with solid wings, typically have even lower values of H compared to the low-range turbulence intensity cases, i.e. cases with cut-out wings. This suggests that there is higher FST penetration into the boundary layer for the higher turbulence intensity cases. The data of Hancock and Bradshaw (1983), which has low turbulence intensity of around 3-4% generated by a static grid, is also shown in Figure 3.5(a). The shape factors of their cases reside between the no-FST case and those of the comparatively higher FST cases of the present study, which supports the systematical reduction of the shape factor with the increase in free-stream turbulence level. Furthermore, it is known that H is a slowly decreasing function of Re_θ for a canonical turbulent boundary layer (Monkewitz et al., 2008) and this observation also appears to be valid for the FST cases shown in Figure 3.5(a).

Thus far, the results that demonstrate the variation of different boundary layer parameters with different free-stream turbulence conditions have been shown. The aforementioned results were obtained by altering the velocity of the free-stream, the active grid actuation scheme and its blockage. However, in order to examine the development of the boundary layer, it is perhaps more relevant to compare the state of the boundary layer at a fixed unit Reynolds number. In order to compare this, the boundary layer state (in this case Re_θ) is plotted against the Reynolds number based on the downstream distance of the test plate, Re_x, in Figure 3.5(b). This representation takes into account the decay of the FST and the growth of the boundary layer in some ways and can be used to compare cases at the same Re_x for different intensity values of FST. If the power-law decay rate of the FST is the same across different cases (as previously shown), then this plot shows the development of the boundary layer up to a fixed value of Re_x. The figure shows that for the same Re_x (indicated by dashed arrows in the direction of increasing turbulence intensity), higher turbulence intensity in the free-stream results in higher Re_θ. It can also be observed that one could change Re_x and obtain the same Re_θ by modifying the free-stream turbulence intensity. It should be noted that the four FST cases given in Table 3.2 enable the comparison of the effects of different FST levels on the boundary layer for a fixed Re_x, say cases B and D, and the effects of different Re_x for similar FST levels, say cases A and B and/or cases C and D.

It has been well established that the presence of FST increases the skin friction in the boundary layer (Hancock and Bradshaw, 1983; Blair, 1983b; Castro, 1984; Stefes and Fernholz, 2004). For a smooth wall zero-pressure-gradient boundary layer without FST, the skin friction coefficient is given as a function of Reynolds number, Re_θ, through a semi-empirical relation by Fernholz and Finley (1996). The baseline case from this study is captured by their relation, as shown in Figure 3.6, whereas the FST cases result in

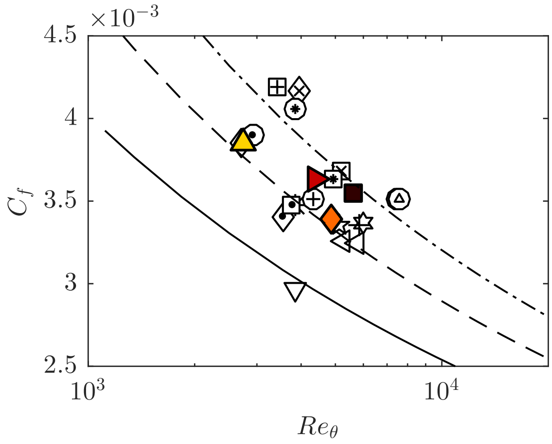

Figure 3.6: Variation of skin friction coefficient, C_f with Re_θ. (△) case A; (◆) case B; (▶) case C; (■) case D; (▽) no-FST case; (◁) Hancock and Bradshaw (1983); (—) Fernholz and Finley (1996) correlation, (– –) fitted line for low range turbulence intensity cases and (–.) fitted line for high range turbulence intensity cases based on Fernholz and Finley (1996) correlation. Conditions of the cases for all other data markers are found in Table 3.3.

larger values of the skin friction coefficient compared to this relation. Figure 3.6 also appears to show that the empirical relation of Fernholz and Finley (1996) seems to hold for the FST cases, however, with different offset values for the two different turbulence ranges shown in the plot as fitted lines. At a constant Re_θ of, say, 6000 from Figure 3.6, where there is data for three different turbulence intensities (one of Hancock and Bradshaw (1983) and two of present study cases of low- and high-range turbulence), it can be seen that an increase in the free-stream turbulence intensity causes an increase in the skin friction coefficient.

The preceding analysis demonstrated the significance of FST on properties of the boundary layer. Now outer-variable scaling of the free-stream velocity fluctuations can be considered since the boundary layer thickness and the FST appeared to be coupled (see Table 3.2). Figure 3.7 shows the pre-multiplied energy spectra of the streamwise velocity fluctuations in the free-stream normalised by local free-stream variance, $k_x\phi_{uu}/\overline{u_0^2}$. The streamwise wavelength, ζ_x, appears on the abscissa normalised by δ. Each case appears to be forced from the free-stream at a similar length scale of around 10δ. This suggests that the external disturbance experienced by the boundary layer is most energetic at about 10δ and the response to forcing at this dominant scale for different levels of forcing (i.e. FST level) can be examined in detail by comparing the boundary layer subjected to these different cases. The boundary layer characteristics under the influence of different FST levels will be investigated through statistical as well as spectral characteristics in the following chapters.

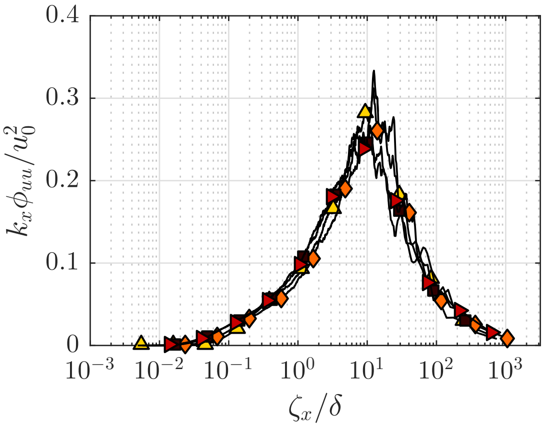

Figure 3.7: Normalised pre-multiplied energy spectra of streamwise velocity fluctuations, $k_x\phi_{uu}/\overline{u_0^2}$, of the free-stream for the FST cases with streamwise wavelength, ζ_x, of the free-stream with respect to boundary layer thickness, δ. (▲) case A; (◆) case B; (▶) case C; (■) case D.

3.4 Mean velocity

The inner-normalised mean streamwise flow velocity is shown in Figure 3.8 for the study cases together with the baseline case. The skin friction velocity in all cases was determined using the Preston tube method. A remarkable feature of the mean velocity profiles of turbulent boundary layers subjected to FST is the persistence of the log-law region for FST levels up to 20% (Thole and Bogard, 1996). The inner-scaled profiles (Figure 3.8) show a clear collapse below the outer region with log-law coefficients of von Kármán constant, $\kappa = 0.384$ and constant, $A = 4.4$; these coefficient values follow from Marusic et al. (2013). This suggests that the effect of FST on the mean flow in the inner region is to alter the value of skin-friction velocity. However, once this change is accounted for, there is self-similarity in the logarithmic region and below. This indicates a proportional effect of the FST in the mean flow and robustness of the law-of-the-wall even when subjected to large external disturbances. This collapse in the mean profiles has also been interpreted by Hancock and Bradshaw (1989) as the mean flow being less affected by FST. The mean velocity profiles deviate from the similarity to the baseline no-FST case as the FST cases have an extended logarithmic region compared to the no-FST case. From the figure, the deviation point of the profiles from the log-law is obvious for no-FST case whereas for the FST cases deviation from that curve occurs at much higher wall-normal positions (in wall units); therefore implying an extended region that is defined by the logarithmic law. The inset in the figure shows a close-up view of the profiles which highlights the similar extension of the logarithmic region for the FST cases. Within the measurement uncertainty, the profiles exhibit a logarithmic region that extends up to $y^+ \approx 700$. This has important implications for the overlap region argument of the turbulent boundary layer. It can be deduced that the validity of the law of the wall, i.e. $U^+ = f(y^+)$, is not dictated here by the outer scales in the boundary

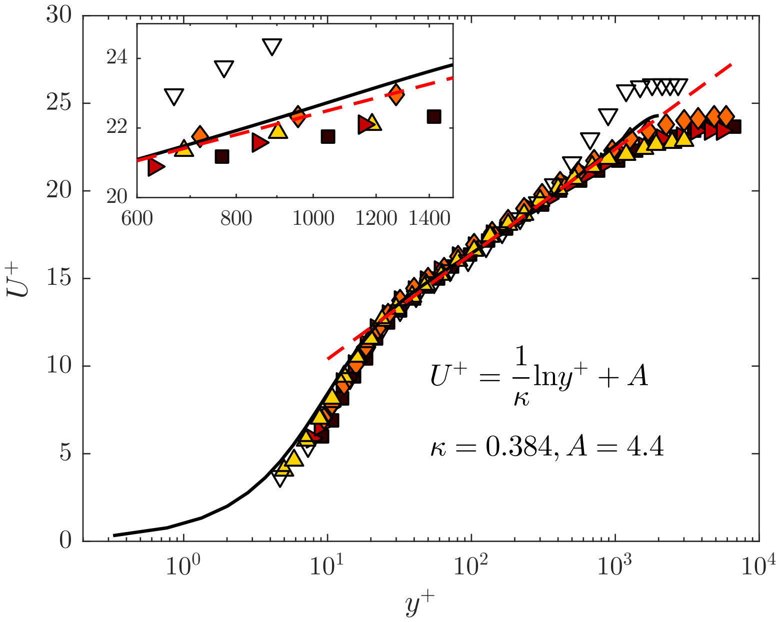

Figure 3.8: Inner-normalised mean velocity profiles. (▲) case A; (◆) case B; (▶) case C; (■) case D; (▽) no-FST case; dashed line: log-law with coefficients κ = 0.384 and A = 4.4, solid line: DNS channel flow data at $Re_\tau \approx 2000$ from Hoyas and Jiménez (2006). The inset shows a close-up of the profiles for the range of $600 < y^+ < 1500$.

layer and FST can be said to affect these outer scales in such a way that the law of the wall can extend up to higher wall-normal positions in wall units. It is assumed for a canonical turbulent boundary layer that the logarithmic law is valid up to $y^+ = 0.2Re_\tau$; therefore looking at the extended y^+ values from the figure, a Reynolds number analogy between the present FST cases and canonical boundary layers can be made. This would imply for the present FST cases to represent a high Reynolds number flow without FST at Re_τ of around 3500.

The extension of the logarithmic region is intimately connected to the suppression of the wake region under the effect of FST. In a canonical boundary layer like the no-FST case, the profile is bounded by the onset of intermittency resulting in a well-defined wake region; however for a turbulent boundary layer under the FST effect, there is no intermittent region since the free-stream is also turbulent and thus the wake region is almost vanished. For this reason, turbulent boundary layers under the FST effect can be said to have similarities with a turbulent channel flow where there is significant turbulence in the outer region at the centreline of the channel. Direct numerical simulation (DNS) data of a turbulent channel flow at $Re_\tau \approx 2000$ from Hoyas and Jiménez (2006) has been added on the mean profile plot for comparison. The suppression of the wake region with respect to the no-FST case is also obvious from their data and shows similarities to the present FST cases. This lack of wake in channel is primarily due to the presence of a turbulent core. In addition to turbulent core, the presence of favourable pressure gradient (FPG) in channel flows would also tend to suppress the wake region (Nagib and Chauhan, 2008); however, this pressure gradient effect is likely to be weak especially at higher Reynolds number. Having said that, presence of FPG will indeed reduce the wake strength in external flow (i.e. boundary layers) due to the acceleration of the free-stream. In fact, Stefes and Fernholz (2004) made an analogy between the FST effect on the wake region of the turbulent boundary layer and the effect of a favourable pressure gradient on a turbulent boundary layer. Consequently, external flows with FPG such as sink flows (Jones et al., 2001) can also produce a mean flow that is similar to the ones presented in the current study, however, the turbulence properties are likely to be different.

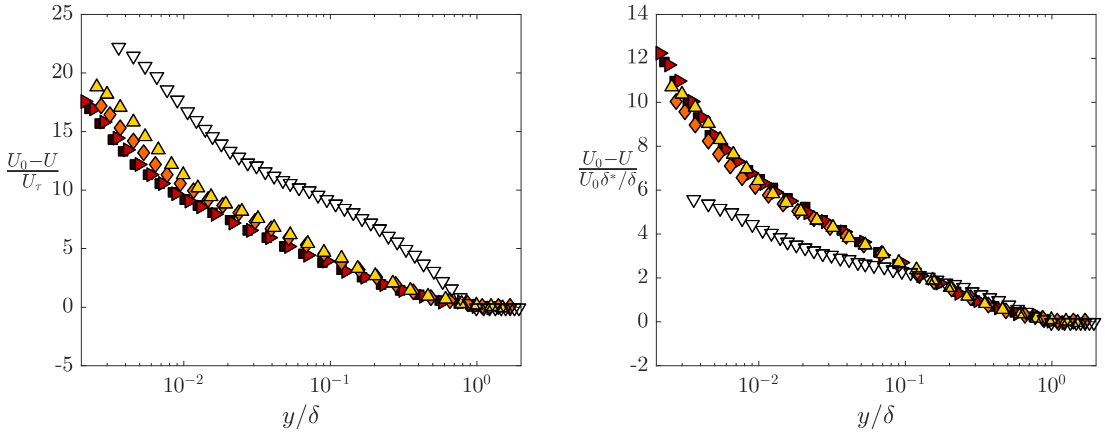

(a)

Figure 3.9: Velocity defect profiles normalised by (a) inner velocity scaling (b) outer velocity scaling proposed by Zagarola and Smits (1998). (▲) case A; (◆) case B; (▶) case C; (■) case D; (▽) no-FST case.

The velocity defect profiles in two different scalings are given in Figure 3.9. The suppression of the wake region can be clearly observed from both scalings. For the first scaling shown in Figure 3.9(a), the velocity defect is either very little or absent in the outer region of the boundary layer when compared with the no-FST case. This results in reduced wake strength as expected for a turbulent boundary layer under the effect of FST (Thole and Bogard, 1996; Sharp et al., 2009). Correspondingly, the Coles wake parameter, Π, that quantifies the wake strength reduces with the presence of FST and even becomes negative for strong FST cases as shown in Table 3.2. In Figure 3.9(b), the outer velocity scale proposed by Zagarola and Smits (1998) is considered following the observations by Brzek et al. (2009). Although the scaling effectively removes Reynolds number variations in the mean velocity defect law for various flows (Klewicki, 2010), it has been shown by Brzek et al. (2009) that it does not completely eliminate the effects of high FST. Therefore, the Zagarola and Smits scaling does not offer any improvement compared to inner-scaling for the velocity-defect similarity of the FST cases with respect to the no-FST case; however, the various FST cases appear to collapse. This scaling is proportional to the mass flux deficit, i.e. δ^*, and since the mass flux deficit does not vary among different FST cases, the similarities between different cases can therefore be justified. Although Brzek et al. (2009) observed an improved collapse with the Zagarola and Smits scaling, an overall collapse as shown in Figure 3.9(b) was not achieved. This is probably due to the fact that the mass flux in their case is also under the influence of surface roughness.

3.5 Summary

Mean flow and bulk properties of FST and the turbulent boundary layer have been presented in this Chapter. The FST cases investigated in detail in this study were generated by rotating the grid rods at a specific motor scheme while running the wind tunnel at different inlet velocities. This resulted in four different FST cases that had similar length scales of around 10δ but different turbulence intensity levels ranging from around 7% to around 13%.

The effects of FST on the skin friction and boundary layer integral parameters were found to be consistent with the previous studies (Hancock and Bradshaw, 1983; Castro, 1984; Stefes and Fernholz, 2004). The wake region of the boundary layer has been shown to be suppressed by the presence of FST and the logarithmic region has been observed to extend. This shows the robustness of the log-law even under the high levels of turbulence as previously observed by Thole and Bogard (1996). The mean flow has been found to be less affected by FST. The differences in FST levels are expected to have more pronounced effects in turbulence characteristics of the boundary layer and the energy distribution in the boundary layer which are the contents of the next chapter.

Chapter 4

Turbulence statistics and spectral analysis

4.1 Introduction

The penetration of highly fluctuating FST into the boundary layer is expected to alter the turbulence intensity distribution inside the boundary layer. The energy distribution among the scales of the boundary layer also needs attention with the addition of the energetic large-scales of FST. Here, in this chapter, the turbulence intensity profiles are presented to investigate the broadband influence of the FST in different regions of the boundary layer, divided mainly into two sections as the near-wall region and the outer region of the boundary layer. Later in the chapter, the results of the spectral analyses are discussed to investigate how the energy distribution across the boundary layer is influenced by the presence of FST.

4.2 Streamwise broadband turbulence intensity

The broadband turbulence intensity, i.e. variance, profiles of the streamwise velocity fluctuations are given in Figure 4.1 for two different normalisations. For the first case, the variance profiles are normalised by corresponding variance of the free-stream fluctuations (Figure 4.1(a)). Within the boundary layer the normalisation does not collapse these profiles. Rather, this normalisation may be interpreted as a gain of the turbulence level in the boundary layer compared to the free-stream turbulence whereby the turbulent fluctuations outside the boundary layer amplify the fluctuations within the boundary layer. Therefore, in the free-stream the amplification is exactly $\overline{u^2}/\overline{u_0^2} = 1$. Within the boundary layer the amplification may vary up to the wall owing to the penetration of FST. Using this analogy, it can be further claimed that the level of amplification and

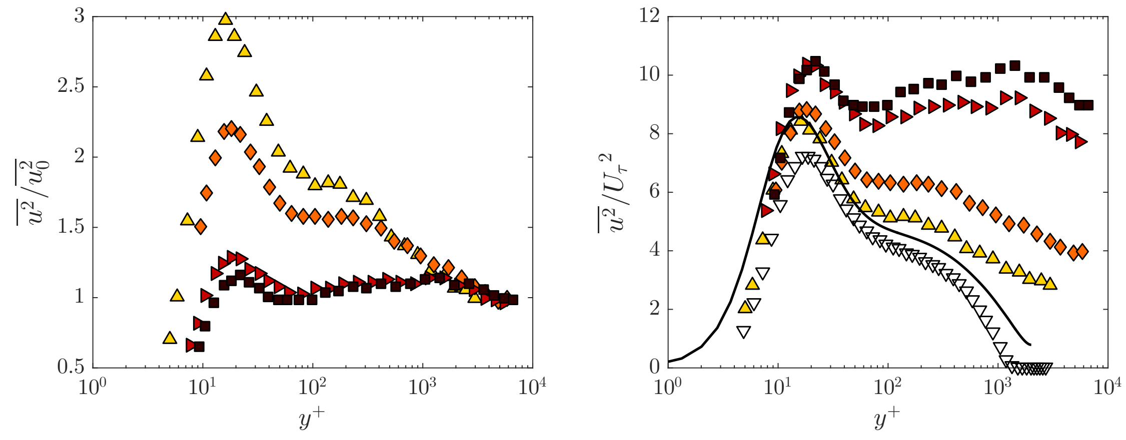

(a) (b)

Figure 4.1: Variance profiles of streamwise velocity fluctuations. (a) Free-stream variance normalised; (b) inner-normalised. (△) case A; (◆) case B; (▶) case C; (■) case D. No-FST case (▽) and DNS channel flow data at $Re_\tau \approx 2000$ from Hoyas and Jiménez (2006) (solid line) are also plotted in (b).

the distribution varies with the level of the free-stream disturbance. For example, it is shown in Figure 4.1(a) that for the higher turbulence levels a more uniform amplification throughout the boundary layer exists. In contrast, for lower turbulence range, the near-wall turbulence peak remains a dominant feature. Therefore, the highest amplification likely occurs when the free-stream is laminar and when the fluctuations in the near-wall are solely governed by near-wall cycle. This suggests a possible saturation limit for the turbulence within the boundary layer when subjected to external disturbances. Because a relative effect of the FST at each wall normal location can be observed, the investigation of the energy distribution throughout the boundary layer with spectral analysis will be used to clarify how the energy of the FST affects the different regions of the boundary layer.

The inner-normalised variance profiles are presented in Figure 4.1(b) in comparison with the no-FST case and with the DNS data from Hoyas and Jiménez (2006) for a turbulent channel flow. The response of the fluctuating component of the streamwise velocity in the boundary layer to the change in the free-stream turbulence level is not consistent, which is similarly found in Figure 4.1(a). Immediately evident from Figure 4.1(b) are the behaviour of the near-wall peak and the emergence of an outer-peak for these laboratory scale flows. Both these features are examined in greater detail in the following sections.

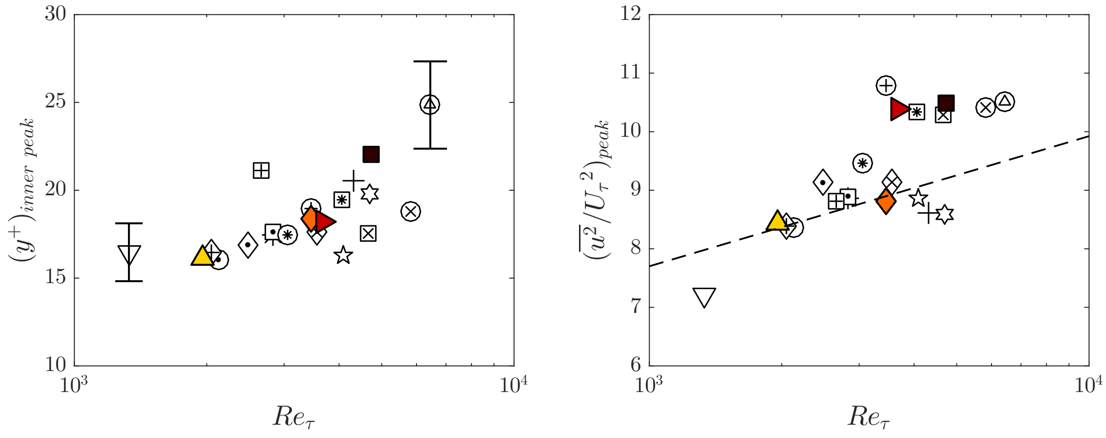

(a) (b)

Figure 4.2: Variation of (a) the location and (b) the amplitude of the near-wall peak of the inner-normalised variance of the streamwise velocity fluctuations with Reynolds number. (▲) case A; (◆) case B; (▶) case C; (■) case D; (▽) no-FST case. Conditions of the cases for all other data markers are found in Table 3.3. Error bars shown in (a) correspond to 10% uncertainty in y^+, dashed line in (b) is the curve fit, $\left(\overline{u^2}/U_\tau^2\right)_{peak} = 1.036 + 0.965\ln(Re_\tau)$, given by Hutchins and Marusic (2007b).

4.2.1 Near-wall region

For canonical turbulent boundary layers, the near-wall turbulence production, governed by the near-wall cycle of streaks and quasi-streamwise vortices, peaks at $y^+ \approx 15$ as documented in many studies to date (Smits et al., 2011). In the present study, the location of the near-wall peak appears to propagate away from the wall (for inner scaling) with increasing Reynolds number as shown in Figure 4.2(a) for the inclusive dataset summarised in tables 3.2 and 3.3. The error bars represent the largest uncertainty in locating the wall to justify the discrepancy of the present cases from the expected $y^+ \approx 15$ location. The outward movement of the near-wall peak, in wall units, has important implications in terms of the extent of the penetration and the governance of the near-wall turbulence production. Similar behaviour can be found in the comparable data shown by Stefes and Fernholz (2004); however, they did not mention this gradual movement of the peak location. Despite lower Reynolds number (Re_τ) range, Schlatter and Örlü (2010a) also reported a similar trend in the near-wall peak location from several DNS datasets for a canonical zero-pressure-gradient turbulent boundary layer. Regardless, the current study does not have sufficient range of conditions to identify a definitive relationship between FST and the movement of the near-wall peak.

The near-wall peak amplitude increases with the turbulence intensity level of the freestream. Similar attributes in the near-wall peak are also encountered in high Reynolds number boundary layers for increasing Reynolds numbers, Re_τ (Smits et al., 2011).

For these type of flows, the energy in the outer region grows as the Reynolds number increases inferring that the fluctuations of the outer region structures are becoming stronger and comparable to the fluctuations of the near-wall structures (Hutchins and Marusic, 2007a). This induces a growing influence of the energetic outer region on the near-wall region and explains the increase in the near-wall peak amplitude. A possible analogy with high Reynolds number flows in this respect implies similar interactions between the structures of the near-wall and the large structures in the outer region for the present FST cases. The difference here in this study compared to a high Reynolds number flow without FST is that the outer large scales here are introduced by large scales of the free-stream that penetrate into the boundary layer. The trend in the near-wall peak amplitude for the FST cases is given in Figure 4.2(b), which is again populated with the inclusive dataset summarised in tables 3.2 and 3.3. Also included is the relation given by Hutchins and Marusic (2007b) for the variation of the near-wall peak with Re_τ. For low-range turbulence intensity cases, the data appears scattered about the relationship given by Hutchins and Marusic (2007b) whereas the high-range turbulence intensity cases appear consistently above that relation. Regardless, it is evident that for FST cases, like in high Reynolds number flows, the increase in the near-wall peak can also be attributed to the increasing influence of the large scales on the near-wall region as they become more energetic with increasing Reynolds number.

It is also worth to mention that the increase in the fluctuation levels in the near-wall peak varies among the different cases. The difference in the peak levels with respect to the no-FST case is more prominent between the low- and high-range turbulence intensity cases (e.g. between case B and case D or between case A and case C) than between the similar intensity cases (e.g. between case A and case B or between case C and case D). This is due to higher penetration of FST into the boundary layer in higher FST cases, a point which will be made clear from examining the spectra. This also indicates that the increase in the level of fluctuations in the near-wall region is mostly governed by the level of turbulence in the free-stream.

Figure 4.1(b) also shows that the near-wall peak for case A is similar to that of a turbulent channel flow at a comparable Reynolds number. However, the channel flow has a free-stream turbulence level of only about 2% to 4% (i.e. the streamwise turbulence intensity at the centreline of the channel). This indicates that although the FST cases do not have an outer wake region in the mean flow due to loss of intermittency, analogous to the channel flow, a much higher free-stream turbulence appears to be necessary for the near-wall peak to have the same intensity as a channel flow at the same Re_τ. This suggests that the near-wall region of the boundary layer damps out the outer disturbances much more than in a channel flow.

4.2.2 Outer region

The outer region of the boundary layer is directly affected by the presence of FST, in comparison to that of the near-wall region, as shown in Figure 4.1(b). The variance of the no-FST case levels off at approximately zero since the free-stream has near-zero turbulence whereas the FST cases level off at the non-zero free-stream fluctuation values. For each of the FST cases, starting from the level of free-stream turbulence at the edge of the boundary layer, the fluctuations in the outer region are amplified. The amplification there appears higher for high-range turbulence intensity cases. This reflects the growing energy level in the free-stream. Similarly, in high Reynolds number flows, the outer scales become more energetic as the Reynolds number increases and this is reflected in the emergence of an outer peak in the streamwise velocity spectra (Hutchins and Marusic, 2007a). Also, the increasing magnitude and constancy of the plateau-like region in the variance profiles is observed to coincide with that peak (Klewicki, 2010). Therefore, in an attempt to investigate the energy distribution for the study cases, spectral analysis is performed and interesting similarities with high Reynolds number flows are observed.

Figure 4.3 shows contour maps of the inner-normalised pre-multiplied energy spectra of the streamwise velocity fluctuations that are plotted against wall distance, y, and streamwise wavelength, $\zeta_x \, (= 2\pi/k_x)$, for the FST cases with their corresponding mean velocity and variance profiles. Figure 4.3(a) to 4.3(d) are in order of increasing turbulence intensity levels. They are also in the increasing order of friction Reynolds numbers with $Re_\tau = 1960$, 3450, 3670 and 4720, respectively. For each of the contour maps two distinct peaks in the energy are observed, which will be referred to as the inner and outer spectral peaks and indicated by black and white (+) symbols, respectively. The inner spectral peak corresponds to the near-wall cycle of streaks and quasi-streamwise vortices. The location of that peak is found to be fixed in inner coordinates at $y^+ {\approx} 15$ and $\zeta_x^+ {\approx} 1000$ from all the spectra plots as also previously found in Hutchins and Marusic (2007a,b) for a canonical turbulent boundary layer. The vertical dashed lines following the inner spectral peak also shows the corresponding wall normal location in variance profiles presented in plot (ii) for each case. As FST level increases, it can be seen that the near-wall spectral peak remains rooted at $y^+ = 15$. However, the near-wall broadband peak in the variance seems to move outwards as observed previously in Figure 4.2(a). The disparity between these two peak locations can be related to the low wavenumber content of the FST in the near-wall region. The footprint of the outer broadband peak in the near-wall is essentially causing the inner broadband peak to occur further away from the wall. Apart from indicating how far the penetration can go down to very near-wall, it can also be deduced that the extent of penetration depends on the level of turbulence. This is consistent with the observed increase in the near-wall peak amplitude (Figure 4.1(b)) with increasing FST level.

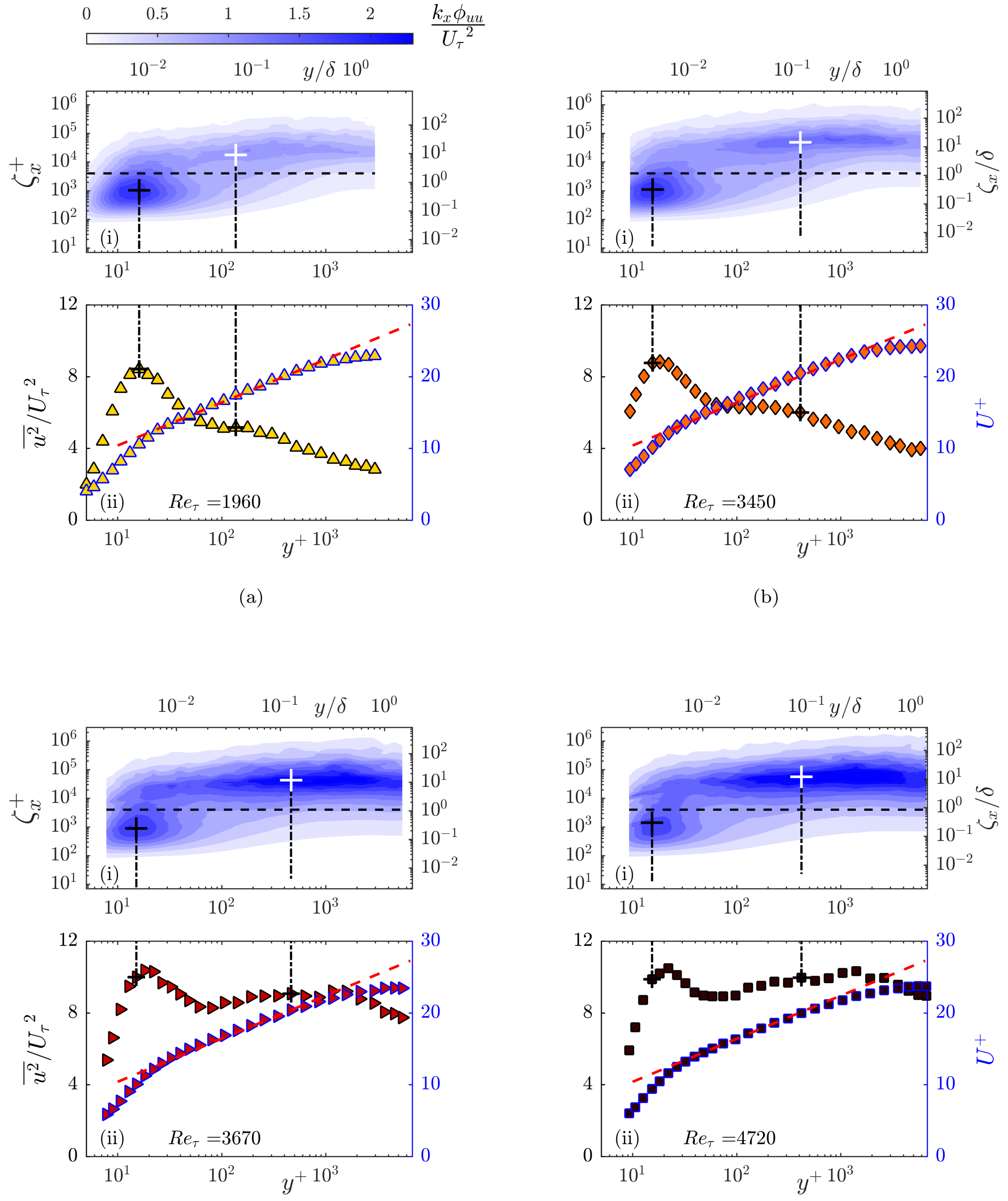

(a) (b) (c) (d)

Figure 4.3: (i) Contour maps of the inner-normalised pre-multiplied energy spectra of the streamwise velocity fluctuations, $k_x\phi_{uu}/U_\tau^2$, for cases (a) (▲) case A; (b) (◆) case B; (c) (▶) case C; (d) (■) case D. The ordinates show streamwise wavelength, ζ_x, in both inner (left) and outer (right) scaling. The abscissas show the wall normal location, y, also plotted in both inner (bottom) and outer (top) scaling. (+) indicates inner (black) and outer (white) spectral peaks. (ii) Corresponding mean (blue outlined marker) and variance profiles. Dashed red line: log-law with coefficients $\kappa = 0.384$ and $A = 4.4$. Dot-dashed vertical lines and (+) symbols represent the locations corresponding to the spectral peaks indicated on (i).

As mentioned previously, there is a second distinct spectral peak in the outer region indicated with a white (+) symbol on spectra plots. The emergent outer spectral peaks for FST cases seem to increase in magnitude with increasing Reynolds number, i.e. with increasing FST levels. A similar behaviour is also known to occur for the canonical turbulent boundary layer with increasing Reynolds number. This similarity could have implications in mimicking high Reynolds number flows that are difficult to achieve without a purpose-built facility, by using FST at much lower Reynolds numbers. This observation will be investigated more in Chapter 5.

For the high-range turbulence cases, two distinct broadband peaks are observed in the variance profiles; here, however, the focus is given on the peak that corresponds to a location inside the logarithmic region. The origin of the other broadband peak further from the wall would require a large database of high FST cases to give detailed consideration and it is therefore not possible to discuss in this study. Within the logarithmic region, the broadband turbulence peak coincides with plateau-like region in the variance profiles. For sufficiently high Reynolds number flows, i.e. having sufficient scale separation, the wall-normal location of that peak has been shown to nominally coincide with the centre of the log region as shown by Hutchins and Marusic (2007a). They also related the outer peak with the large-scale structures in the log region. For FST cases, a similar behaviour is observed where there appears to be a nominal spectral peak in the log region. Furthermore, the peak energy in this region occurs about a wavelength of 10δ, which is also the most energetic wavelength in the free-stream. This dominant scale was, in fact, a deliberate choice made when establishing the scales of the FST as it is consistent with the energetic scales of high Reynolds number turbulent boundary layers. This behaviour was also observed by Sharp et al. (2009) where they presented the pre-multiplied energy spectra of boundary layer at different wall-normal locations and the free-stream together and they concluded that the energetic wavelengths in the outer region were associated with the most energetic scales of the free-stream. Given the relationship between the free-stream energetic scales and the outer spectral peak, it is consequential to look at the ratio of their corresponding spectral energy at the outer peak wavelength. In this way, a wavelength-specific gain of the turbulence level compared to FST as given in Figure 4.4(a) could be obtained. This is similar to the broadband gain that is previously presented in Figure 4.1(a). Likewise, it is deduced that the level of amplification varies with the level of free-stream and high-range FST cases tend to amplify less.

For canonical turbulent boundary layers, the location of the outer spectral peak has been shown to gradually move outward in wall units, y^+, with increasing Re_τ and this movement is also found to be proportional to $Re_\tau^{1/2}$ (Klewicki et al., 2007; Mathis et al., 2009). The location of the outer spectral peak for the inclusive set of FST cases show agreement with this trend as plotted in Figure 4.4(b). Despite the good agreement, it should be noted that the range of Re_τ covered in this study is limited and it is therefore very difficult to decipher this relationship without the guidance from previous work in this area.

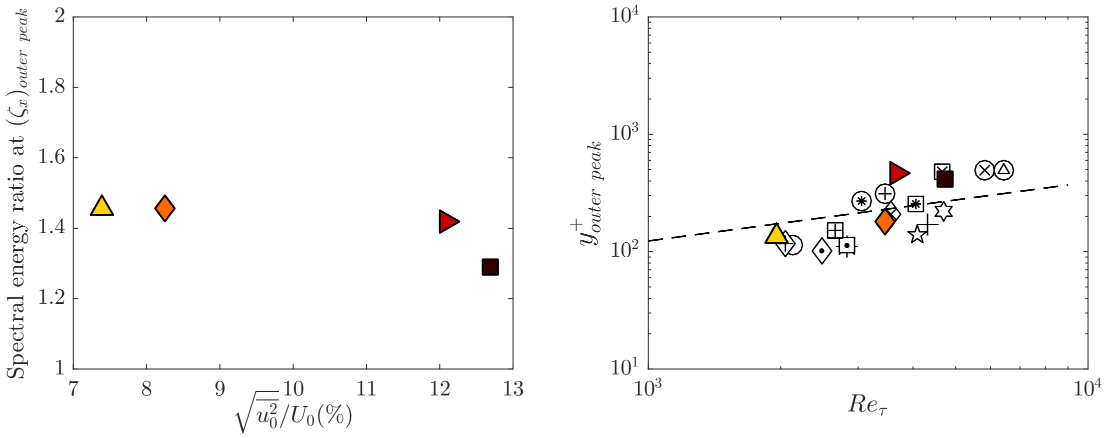

(a)

(b)

Figure 4.4: (a) Spectral energy ratio between the FST and the boundary layer at the outer peak wavelength (b) variation of the wall normal location of the outer peak of the inner-normalised variance of the streamwise velocity fluctuations with Reynolds number. (△) case A; (◆) case B; (▶) case C; (■) case D. Conditions of the cases for all other data markers are found in Table 3.3. Dashed line represents the relation of $3.9Re_\tau^{1/2}$ from Mathis et al. (2009) for the wall-normal location of the outer peak based on the definition of the log region as $100 < y^+ < 0.15Re_\tau$.

4.3 Summary

In this chapter, the turbulence statistics has been presented through variance profiles of the streamwise velocity fluctuations. By examining the energy spectra of the streamwise velocity fluctuations in the boundary layer, it has been inferred that the FST penetrates into the boundary layer and can go very near the wall. This has led to an overall increase in the streamwise velocity fluctuations in the boundary layer as observed in the variance profiles and the influence has been more prominent with increasing strength of the turbulence level in the free-stream. The near-wall peak amplitude has also kept increasing with the turbulence level. This has been found analogous to the trend in high Reynolds number canonical flows with increasing Reynolds number. Similar to these flows, this trend has also been attributed to the increasing influence of energetic large-scales in the outer region on the near-wall with increasing Reynolds number. It is also observed that the wall normal location of the near-wall broadband peak moves gradually outwards in wall units. Further studies and examinations are needed to validate this observation since it challenges the idea of having a fixed location ($y^+{\approx}15$) for the peak turbulence production in the near-wall region which has been accepted in turbulence studies to date.

The boundary layer formed a secondary peak in the logarithmic region under the effect of FST. This has been found similar to outer peak formation in high Reynolds number flows when there is enough scale separation. The strength of that peak has been observed to increase with increasing Reynolds number, directly related to the turbulence level in the free-stream for this particular study, and to move gradually outwards in wall units as also encountered in high Reynolds number canonical flows.

Chapter 5

Scale Interactions

5.1 Introduction

Despite not having measurements very close to the wall, Sharp et al. (2009) suggested that the FST can reach deep into the boundary layer and have a direct effect on the inner scales of the boundary layer. The previous section demonstrated that the direct effect indeed reaches down to the wall and in fact moves the near-wall peak farther away from the wall. It is also important to examine any other effect of FST on near-wall turbulence. Decomposing the scales as large and small scales using a sharp spectral cut-off filter, Mathis et al. (2009) found that the near-wall turbulence is modulated by the energetic outer region of the flow in a canonical high Reynolds number boundary layer. Here, in this chapter, a similar analysis for the FST cases is carried out and the interactions between these decomposed-scales are investigated through single and multi-wire measurements.

5.2 Scale separation and skewness analysis

A filter at a cut-off wavelength (ζ_x^+) of 4000 (the horizontal dashed line in Figure 4.3) represents a reasonable demarcation between the large- and small-scale components of the streamwise fluctuating velocity signal as the component of the energy above or below the cut-off, respectively. This also corresponds to $\zeta_x/\delta \approx 1 - 2$ for all the cases. The robustness of the decoupling procedure is shown in Mathis et al. (2009) for various different cut-off wavelengths; therefore in terms of investigating the interactions between the large and small scales, the choice of cut-off wavelength is not expected to have a considerable effect.

Figure 5.1 shows the inner-normalised variance profiles of scale-decomposed streamwise velocity fluctuations. These two separate variance profiles can be considered as the two

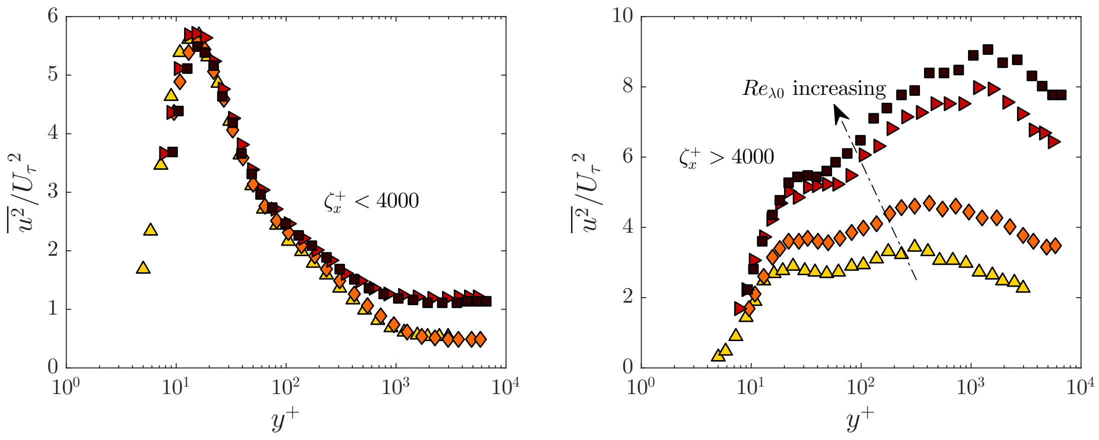

(a) (b)

Figure 5.1: Variance profiles of scale-decomposed streamwise velocity fluctuations. (a) Small-scales and (b) large-scales based on a cut-off wavelength filter of $\zeta_x^+ = 4000$. (△) case A; (◆) case B; (▶) case C; (■) case D.

components that add up to the variance profiles presented in Figure 4.1(b). The contribution from the small-scale to the total variance of the streamwise velocity fluctuations (Figure 5.1(a)) does not seem to change with different turbulence intensity levels across most of the boundary layer; however, overall, the effect of small-scales seems to diminish to the edge of the boundary layer for all FST cases. The small-scale variance profiles have essentially eliminated any superposed effect of large-scale motions on the measured statistics. The fact that the small-scale contributions collapse for different cases after filtering out the superposition of large-scales indeed confirms the direct penetration effect of FST on the near-wall region as also suggested by Sharp et al. (2009). That also shows that the choice of cut-off wavelength was appropriate to separate the scales.

The large-scale variance profiles exhibit an increase in the near-wall region, reaching a local maxima ($y^+ \approx 15 - 30$) and increases further farther away from the wall. Overall, large-scale contribution increases across almost all wall-normal locations with increasing FST levels. Apart from gradual movement of the local peak turbulence intensity location, there is also amplitude increase of the local peak with increasing FST levels. This is also observed in high Reynolds number flows as the increasing effect of large-scales on the near-wall region with increasing Reynolds number and this is found to be an indication of a growing outer-layer influence on the near-wall region (Hutchins and Marusic, 2007b; Smits et al., 2011).

Any modulation effect involved in the interactions between the scales is not directly inferred from these two plots as the modulation can be symmetric. More insights about the modulating effect of the large scales could be obtained from skewness analysis. Mathis et al. (2011b) confirmed that the amplitude modulation coefficient (R) defined by Mathis et al. (2009) as the correlation coefficient between the large-scale fluctuations and the filtered envelope of the small-scale fluctuations is similar to the cross-term of the scale-decomposed skewness, $3\overline{\overline{u_L^+ u_S^{+2}}}$. They even suggested to alternatively use this cross-term to quantify the level of amplitude modulation instead of the amplitude modulation coefficient. Therefore, first, the cross-term of the scale-decomposed skewness factor will be used to diagnose the modulating effects of the large scales. Later, in this chapter, the modulation effect will be exploited more with the modulation coefficient R.

For the skewness analysis, the expansion of the skewness factor, S_u, as first used by Schlatter and Örlü (2010b) for wall-bounded flows and as outlined in Mathis et al. (2011b), is followed. Using a scale-decomposed signal of the fluctuating streamwise velocity signal as $u^+ = u_L^+ + u_S^+$, S_u can be expanded in the following form

$$S_u = \overline{\overline{u_L^{+3}}} + 3\overline{\overline{u_L^{+2} u_S^+}} + 3\overline{\overline{u_L^+ u_S^{+2}}} + \overline{\overline{u_S^{+3}}} \tag{5.1}$$

with $\overline{\overline{X}} = \overline{X}/(\overline{u^{+2}})^{3/2}$ for any quantity X (refer to equation 2 to 4 in Mathis et al. 2011b).

Figure 5.2 shows the total skewness and the three dominant terms (terms 1, 3 and 4 in the above equation) that contribute to this skewness for different FST cases. The cross-term $3\overline{\overline{u_L^{+2} u_S^+}}$ is close to zero and does not contribute to the skewness factor and hence is not shown.

The total skewness factor is compared in Figure 5.2(a) with the results of Mathis et al. (2011b) that was obtained from a turbulent boundary layer without FST at $Re_\tau = 2800$. It is seen from this figure that the skewness profile of case A being the lowest turbulence intensity case with $Re_\tau = 1960$ has closer values to their study. The similarity of the trend in the profiles starts to fail due to the presence of an intermittent region in their case of a turbulent boundary layer without FST whereas this intermittent region does not exist in a turbulent boundary layer under the FST effects. For turbulent boundary layers without FST, it is shown by Metzger and Klewicki (2001) that the local minima of the skewness in the near-wall region increases and becomes positive with increasing Reynolds number. Although the Reynolds numbers under consideration in the present study are not comparable to the highest value in their study, a similar trend in the local minima in the near-wall region is also observed for FST cases with increasing FST levels. This could be another supporting evidence for a possible analogy between the turbulent boundary layers under the FST effect and the high Reynolds number turbulent boundary layers without FST. The positive local minima observations here for the FST cases are similarly found in the results from Sharp et al. (2009).

The contributions from the large-scale term $\overline{\overline{u_L^{+3}}}$ (Figure 5.2(b)) are almost always positive and seem to increase with FST levels. The positiveness of the large-scale contributions can be attributed to the fact that the distribution of large-scales in a grid-generated turbulence is slightly positively skewed (Mydlarski and Warhaft, 1996). This is also illustrated on the figure with the inset plot for the probability density function of large-scales

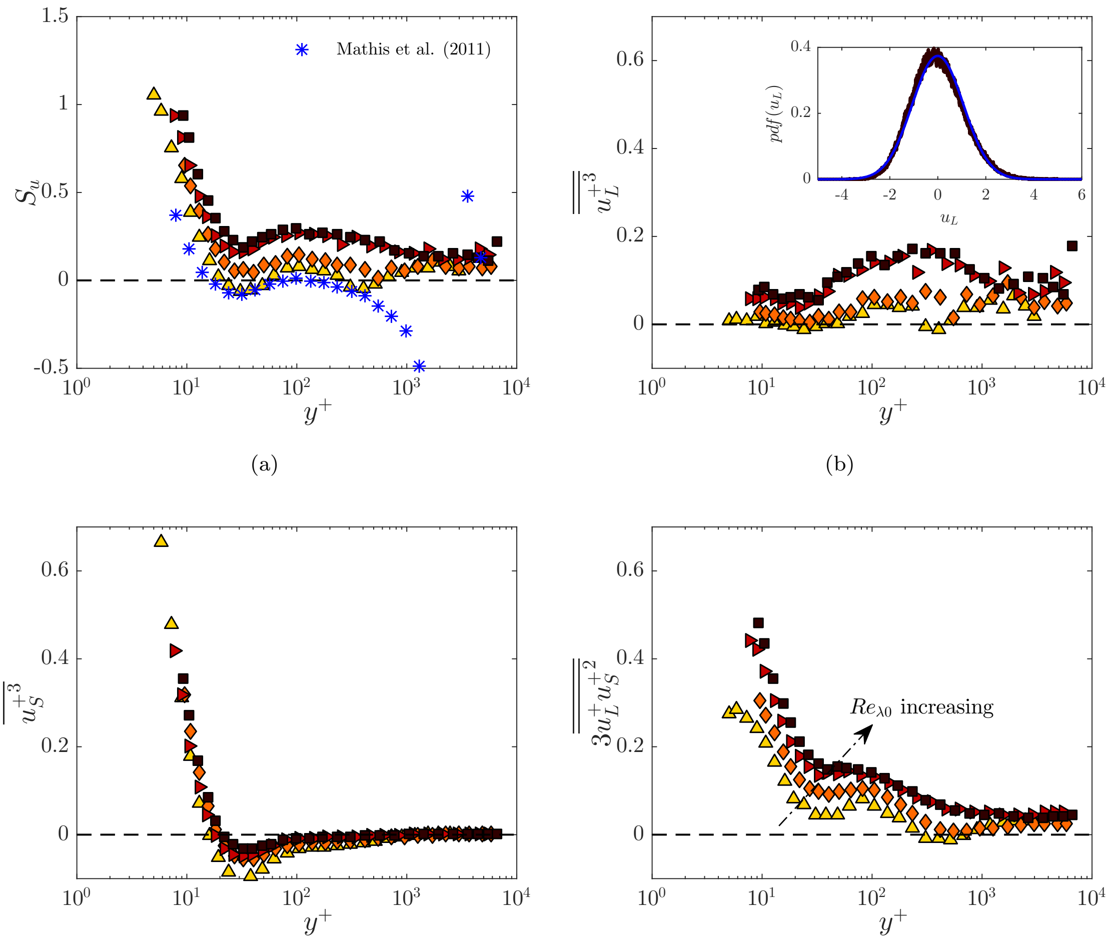

(a) (b)

(c) (d)

Figure 5.2: Variation of (a) the skewness factor, S_u, in comparison with the data from Mathis et al. (2009) for $Re_\tau = 2800$ and dominant terms of the scale-decomposed skewness (b) $\overline{\overline{u_L^{+3}}}$, (c) $\overline{\overline{u_S^{+3}}}$ and (d) $\overline{\overline{3u_L^+u_S^{+2}}}$ across the boundary layer: (△) case A; (◆) case B; (▶) case C; (■) case D. The inset for (b) shows a probability density function (pdf) of the large scales, u_L, for a representative case (case D) at $y^+ \approx 100$ in comparison with a Gaussian distribution (blue smooth line).

for case D as a representative case and it is seen that the distribution is slightly positively skewed when compared to a Gaussian distribution. It is also worth to note that similar turbulence intensity cases (case A and case B or case C and case D) have similar large-scale contributions. The substantial amount of contributions for all cases seems to occur at around the assumed start of the log-region and higher above, i.e. $y^+ > 30$. This region of dominance is expected to be due to the large scales in FST and their penetration and presence in the log-region of the boundary layer.

Figure 5.2(c) shows that the small-scale term $\overline{\overline{u_S^{+3}}}$ exhibits little variation across the majority of the boundary layer among different FST cases. The only place where there is any noticeable difference occurs around the near-wall region. The small-scale terms are actually found to locally contribute to the rise of the local minima of the skewness in the near-wall region (Mathis et al., 2011b). The figure shows that increasing the large-scale free-stream turbulence affects the small-scale contribution and this effect increases with increasing FST levels.

The final dominant term, $3\overline{u_L^+ u_S^{+2}}$, shown in Figure 5.2(d), indicates that the amplitude modulation effect increases with increasing levels of FST. There also appears to be some collapse of the wall-normal location of the cross-term with increasing turbulence intensity. This suggests that there could be a finite limit to the levels of amplitude modulation that can be achieved. This trend with increasing FST levels is similar to the Reynolds number trend of a canonical boundary layer in Mathis et al. (2011b). This could imply that the present FST cases could be a limiting trend for a high Reynolds number flow where the turbulence intensity in the outer region is dominant. However, due to lack of available data, this is only proposed as a hypothesis.

Only for the two lower FST levels, the cross term can be seen to dip below zero in the outer region, however, it rises back above zero immediately after. This zero-crossing location has some implications on the phase relationship between large- and small-scales of the flow. Chung and McKeon (2010) noted that the amplitude modulation coefficient, R, can be interpreted as a phase relationship between the large- and small-scales. Duvvuri and McKeon (2015) showed that the phase relation naturally existing in the flow between the scales can be modified by introducing synthetic scales. They suggested that the envelope of all small-scales can be in-phase or out-of-phase with the synthetic large-scale depending on its location with respect to the location of the critical layer (this is the layer where the wave speed of the disturbance is equal to the local mean velocity).

Duvvuri and McKeon (2015) found the zero-crossing location of their amplitude modulation coefficient to be around $y/\delta{\approx}0.1$ (their δ definition is based on the location where $U = 0.99U_0$) which is very close to their critical layer location of $y/\delta{\approx}0.07$. For the present cases, only the two lower turbulence intensity cases exhibit a zero crossing at around $y/\delta{\approx}0.15$. This is further away from the wall compared to the single synthetic scale case. If the interpretation of the zero-crossing as an indicator for the critical layer is maintained, then, the critical layer for these two FST cases is farther from the wall. This suggests that the critical layer tends to move towards the free-stream for higher intensity disturbances (and/or disturbances that are over a range of scales).

It can be seen that for higher FST cases, there is no zero-crossing in the amplitude modulation coefficient. This suggests that the small- and large-scales remain in-phase throughout the entire boundary layer when the forcing exceeds a certain amplitude. This implies that for broadband, high intensity forcing in the free-stream, it might not be possible to match the wave speed of a given disturbance to the mean velocity within the boundary layer and therefore the small- and large-scale remain in-phase throughout the entire layer. The phase relations between the scales will be dealt in more detail in the following parts of this Chapter.

It was shown by Mathis et al. (2009) that single point measurements provide a reasonable estimate of the degree of amplitude modulation in the near-wall, with respect to a separate synchronised measurement at the outer peak, for a canonical turbulent boundary layer. However, the applicability of this to boundary layers forced by FST is yet to be established. A detailed study of the correlation between large scales of both FST and the outer region of the boundary layer and the near-wall small scales requires simultaneous multi-point measurements, which is presented later in this chapter through the multi-wire measurements.

5.3 Amplitude modulation: Single-point measurements

Figure 5.3 shows spectrograms, mean profiles and variance profiles for the four study cases. The details of the figure are given in the figure caption. The observations from the plots (i) and (ii) will be the repetition of that discussed for Figure 4.3; however, for the sake of argument, some of these discussions will be briefly repeated in this section.

The prominent feature of both spectrograms is the presence of an outer peak similar to high Reynolds number flows (Hutchins and Marusic, 2007a). This outer peak is within the logarithmic region of the mean flow as seen in the mean profile. This peak in spectral content in the outer region also appears to be located close to the knee of the variance profile, where the variance starts to decrease above this wall-normal location. All these features are consistent with existing data on canonical high Reynolds number turbulent boundary layers as previously discussed in Chapter 4.

It can be seen that the energy of the outer peak grows with increasing turbulence intensity due to the increasing energy content of the large-scales in the free-stream. These high-energy scales in the free-stream penetrate the boundary layer and attain a local maxima within the outer region of the boundary layer. In this sense, the increase in FST can be viewed as “simulating” an increase in Re_τ for a canonical boundary layer. It should also be noted that the peak in the pre-multiplied energy spectrum occurs at length scales near 10δ, which is consistent with the energetic scales of high Reynolds number turbulent boundary layers. To reiterate, this dominant scale was, in fact, a deliberate choice made when establishing the scales of the FST. It is certainly possible to alter this dominant scale for a different value by altering the active-grid operation mode as well as by altering the location of the flat plate relative to the grid.

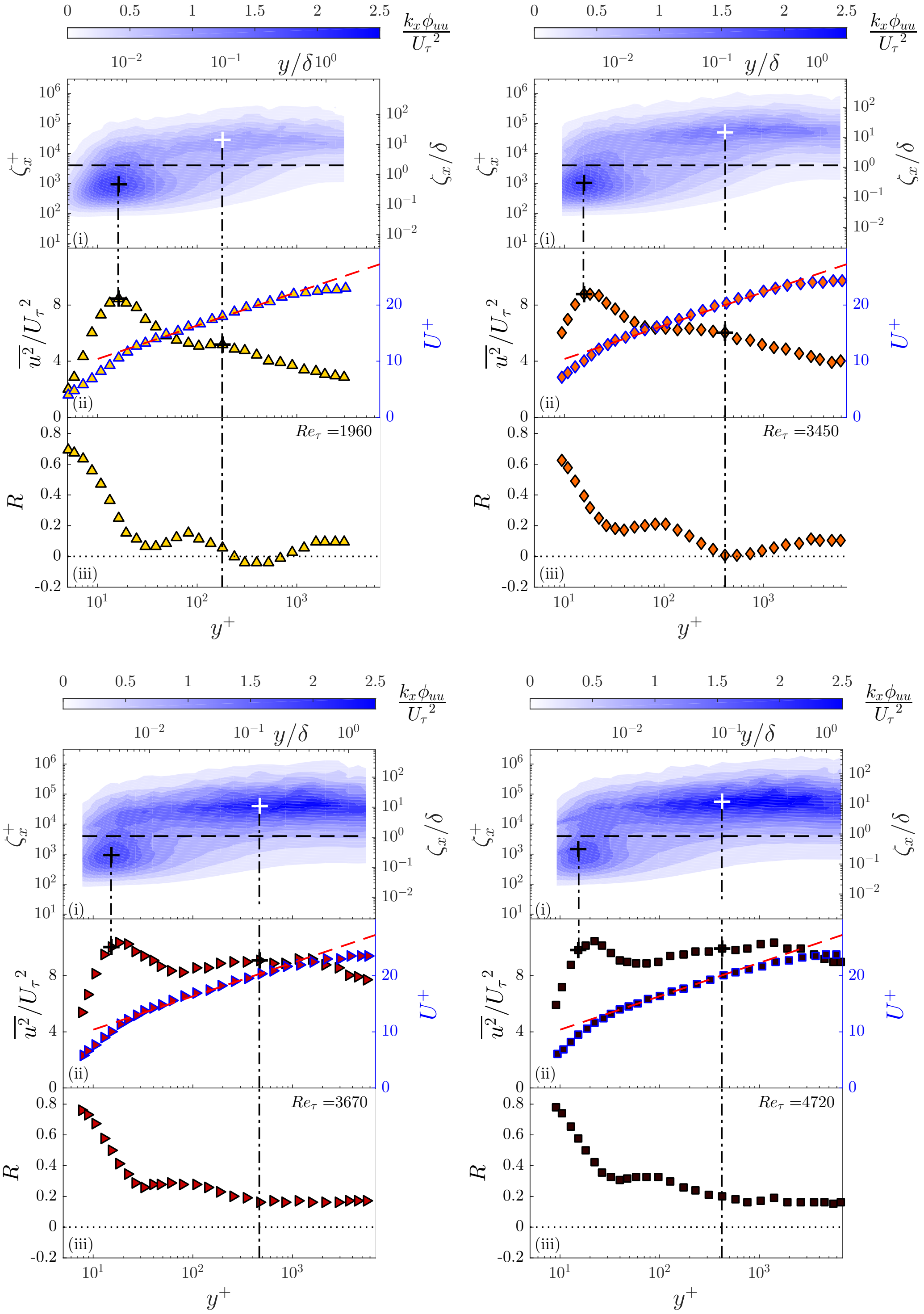

Figure 5.3: (i) Contour maps of the inner-normalised pre-multiplied energy spectra of the streamwise velocity fluctuations, $k_x\phi_{uu}/U_\tau^2$, for (△) case A; (◆) case B; (▶) case C; (■) case D. The ordinates show streamwise wavelength, ζ_x, in both inner (left) and outer (right) scaling. The abscissas show the wall-normal location, y, also plotted in both inner (bottom) and outer (top) scaling. (+) indicates inner (black) and outer (white) spectral peaks. The horizontal dashed line represents the location of the cut-off wavelength at $\zeta_x^+ \approx 4000$. (ii) Corresponding mean (blue outlined marker) and variance profiles. Dashed red line: log-law with coefficients $\kappa = 0.384$ and $A = 4.4$. Dot-dashed vertical lines and (+) symbols represent the locations corresponding to the spectral peaks indicated on (i). (iii) Amplitude modulation coefficient, $R(y^+)$, as defined in equation 5.2 (Mathis et al., 2009). Dot-dashed vertical lines follow the corresponding outer spectral peaks.

The energetic scales in the free-stream (as well as the outer region) have a footprint in the near-wall region. There is a shift of the energy towards long wavelengths (i.e., low wavenumbers) very near the wall. The extent of the penetration depends on the FST level and this essentially "simulates" the effect of increasing Reynolds number. Correspondingly, the amplitude of the near-wall peak in the variance profiles is amplified with increasing FST level. In addition to this direct effect reaching down to the wall, the large-scales in the boundary layer under the influence of FST have been observed to modulate the amplitude of the small-scales in the near-wall region. This effect has been examined using the skewness analysis in the previous section. Here, in this section, a similar approach from Mathis et al. (2009) was employed to investigate the modulating interaction among the scales. They devised an amplitude modulation coefficient as:

$$R = \frac{\overline{u_L^+ \ E_L(u_S^+)}}{\sigma_{u_L^+} \ \sigma_{E_L(u_S^+)}} \tag{5.2}$$

where u_L^+ is the large-scale fluctuations, $E_L(u_S^+)$ is the filtered envelope of the small-scale fluctuations, $\cdot^+$ indicates inner scaling, and σ is the standard deviation. This coefficient is used to quantify the level of modulation across the boundary layer as assessed by a single wire using the same cut-off filter (the horizontal dashed line in plots (i) of Figure 5.3) to separate the scales as large and small as previously done in Section 5.2. From Figure 5.3(iii), it can be seen for all FST cases that the level of correlation, i.e. R value, is high in the viscous layer of the boundary layer suggesting a high level of modulation of small scales in the near-wall region. This correlation decreases until a plateau is reached and then in the logarithmic region, it reaches its minimum value.

For high Reynolds number canonical boundary layers, the correlation coefficient reaches zero at the outer spectral peak location above which the correlation is reversed (Hutchins and Marusic, 2007a; Mathis et al., 2009). Here, in this study, only case A and B reach zero correlation value among which only case A crosses zero. However, the reversal of correlation observed in case A is very weak and does not sustain long. For other cases, the reversal in correlation behaviour is not observed. The lack of reversal (or weak negative correlation considering case A) is primarily related to a reduction in the intermittency in the outer part of the boundary layer when FST is present. The small-scale fluctuations in a canonical boundary layer have a distinct relationship to the large scales as they rely on these large scales for their energy and organisation. However, the small scales in the outer region of the current study are also influenced by the small scales of the FST. These FST-based small scales may not have any relationships to the large scales within the boundary layer and therefore mask the correlation reversal that might exist if it were possible to only consider the small scales that are relevant to the boundary layer. This interpretation also justifies that the lowest turbulence level, case A, exhibits negative correlations albeit weak since the small-scale fluctuations are not as strong as the higher turbulence cases. It is also important to draw attention to the location of the minimum in the correlation that is observed to coincide with the outer

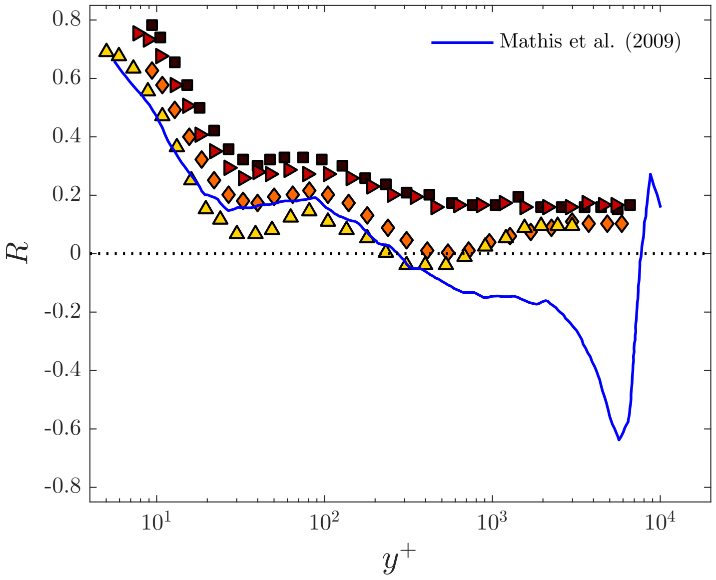

Figure 5.4: Amplitude modulation coefficient $R(y^+)$. (△) case A; (◆) case B; (▶) case C; (■) case D; solid line: Mathis et al. (2009) comparison at $Re_\tau = 7300$.

spectral peak. Only case A has some discrepancy between the location of the minimum and the spectral outer peak. For this difference, it is important to note that the energy variation in the spectra around the outer peak are rather weak which directly affects the choice of an outer nominal peak.

To investigate the trends in R for different FST cases, Figure 5.4 combines the profiles for the four cases and also presents them in comparison to Mathis et al. (2009). The local minimum in the buffer region increases with the increase in turbulence level of FST. This has been similarly observed in scale-decomposed skewness profiles (see Figure 5.2) where the small-scale terms were found to locally contribute to the rise of this local minima. This trend is similar to the Reynolds number dependence of the modulation coefficient for a canonical boundary layer (Mathis et al., 2011b), i.e., increasing FST is akin to increasing Re_τ of a canonical boundary layer. The result of a canonical turbulent boundary layer from Mathis et al. (2011b) sits in between the lower range turbulence intensity cases. As explained before, due to lack of intermittency, the correlation behaviour in the outer region is different for FST cases than a canonical boundary layer. Nonetheless, the similarity between the scale interactions in the near-wall region of the present flow and high Reynolds number boundary layers is remarkable. Therefore, a turbulent boundary layer under the effect of FST can be seen as one way of enhancing the scale interactions that are likely to happen in the near-wall region of high Reynolds number turbulent boundary layers.

5.4 Amplitude modulation: Multi-point measurements

Although single-point measurements were found to provide a reasonable estimate of the degree of amplitude modulation, multi-point synchronised measurements are preferred for the study of interactions between the outer-region and the near-wall region because several assumptions of the former analysis can be relaxed in place of direct observations. As such, the analysis that follows employs the first two wires in the rake described in Figure 2.11 in Chapter 2.

The results presented here in this section from multi-wire experimental campaign are replicated cases of B and D of single-wire measurements presented in the preceding sections. The name convention for cases are maintained for consistency. These two cases are both at $Re_x = 2.2 \times 10^6$ (with $x = 0$ at the leading-edge of the suspended flat plate). Relevant parameters from these cases are provided in Table 5.1, and were calculated in the same manner as described in Chapter 3. All gradient quantities were estimated using a sixth-order centred-differencing scheme as recommended in Hearst et al. (2012). The flow characteristics provided in Table 5.1 agree with those presented in Table 3.2 in Chapter 3 for the same cases to within the uncertainty margins. Furthermore, the new mean profiles collapse well with the old data. Thus, the measurements are repeatable and the multiwire rake and the angle of the probes (30° into the boundary layer as described before in Chapter 2) does not significantly influence the flow or measurements.

The inner probe is at $y^+ \approx 20$ around the near-wall peak and the outer probe is at $y_o^+ \approx 210$ in the log-region where the energy of the large scales is dominant. A sample of the fluctuating streamwise velocity signal in inner-scaling from the inner probe is given in Figure 5.5 for case B (top plot). The signals from the two probes are decomposed into large- and small-scale fluctuating components using the same cutoff wavelength as before as $\zeta_x^+ \approx 4000$. A high degree of correlation is visible from the large-scale fluctuations at these two different wall-normal locations (middle plot). This correlation is found to be $\sim 80\%$. This is higher than 65% found in Mathis et al. (2011a) that was justified as a result of the footprint caused by the superstructure-type events in the log region. The fact that the correlation is higher in FST cases supports the direct penetration of the FST large scales into the boundary layer and down to the near-wall region (this correlation is even higher for case D, $\sim 85\%$). When the small-scale fluctuations of the inner probe are observed in relation to large-scale fluctuations of the outer probe

Table 5.1: Free-stream and turbulent boundary layer parameters for the two study cases of the multi-wire measurements evaluated at the measurement location, $x/M = 43$.

FST cases	U_0 (m/s)	$\sqrt{\overline{u_0^2}}/U_0$ (%)	$Re_{\lambda 0}$	δ (m)	U_τ (m/s)	Re_τ	Re_θ
B (◆)	9.9	8.1	465	0.13	0.42	3590	4500
D (■)	10.1	12.2	630	0.16	0.43	4550	5340

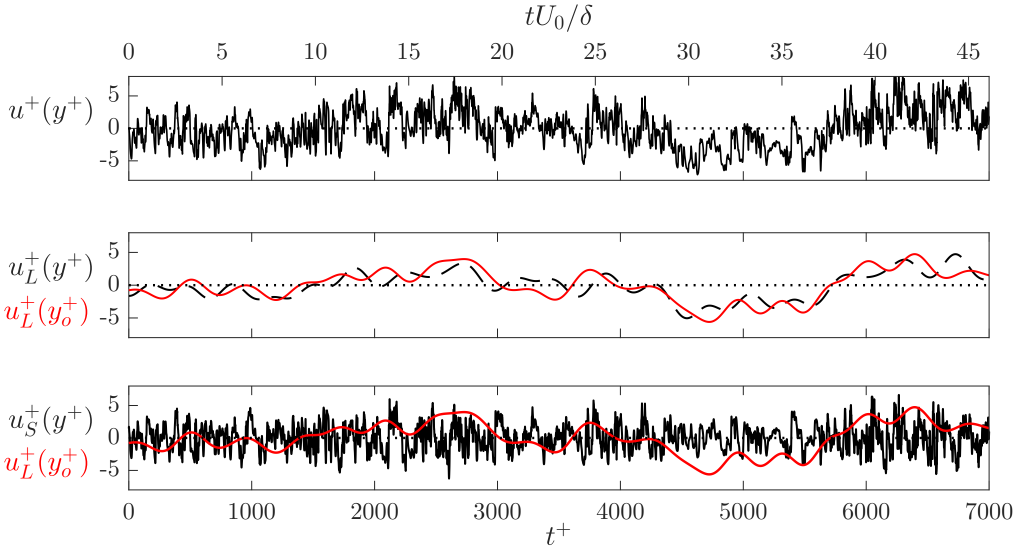

Figure 5.5: A sample of the inner-scaled fluctuating streamwise velocity signal for case B. (Top) raw fluctuating signal, $u^+(y^+)$, at $y^+ \approx 20$; (middle) dashed black line: large-scale fluctuating signal, $u_L^+(y^+)$, at $y^+ \approx 20$, solid red line: large-scale fluctuating signal, $u_L^+(y_o^+)$, at $y_o^+ \approx 210$; (bottom) solid red line: large-scale fluctuating signal, $u_L^+(y_o^+)$, at $y_o^+ \approx 210$, solid black line: small-scale fluctuating signal, $u_S^+(y^+)$, at $y^+ \approx 20$.

(bottom plot), the amplitude modulation effect between these signals can be revealed. For the negative large-scale fluctuations, the fluctuations of the small-scales seem to be quiescent while for the positive large-scale fluctuations, the amplitude of the small-scales fluctuations seems to be amplified. This is similar to a pure amplitude modulation concept in signal processing where a carrier signal (high-frequency signal) is modulated with a low-frequency component.

5.5 Applying the predictive inner-outer model by Marusic et al.

Given the similarities of the scale interactions with that of high Reynolds number canonical boundary layers, there is grounds to test the predictive inner-outer model of Marusic et al. (2010b), also detailed in Mathis et al. (2011a), for the turbulent boundary layers in the presence of FST. This would confirm the analogy between the two flows and validate the applicability of the model to this non-canonical case. Their model is able to predict the near-wall turbulence using only the large-scale information input. With this input, the predicted velocity signal at a wall-normal location is linked to a universal signal (a signal that is free from any large-scale influence) through the model coefficients. Figure 5.6 shows a schematic for the mathematical formulation of the predictive model as given

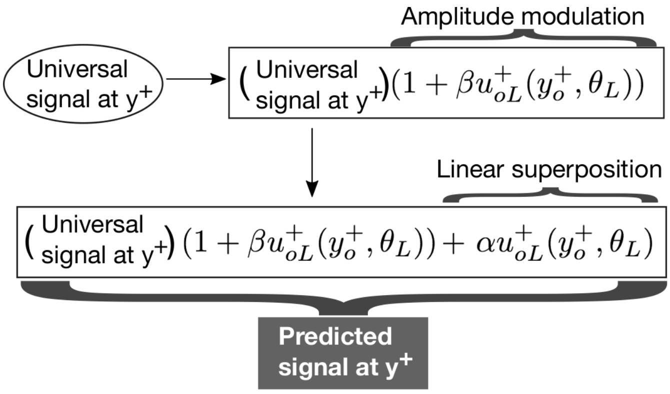

Figure 5.6: Mathematical formulation of the predictive inner-outer model of Marusic et al. (2010b) as adapted from Figure 1 in Mathis et al. (2011a). β: model coefficient for amplitude modulation; $u_{oL}^{+}(y_o^{+},\theta_L)$: low-pass filtered outer probe signal shifted forward in the streamwise direction for the corresponding θ_L where θ_L is the mean inclination angle of the large-scale structures; y_o^{+}: outer probe location; α: model coefficient for linear superposition;

in the following equation:

$$u_p^{+}(y^{+}) = u^{*}(y^{+})\{1+\beta u_{oL}^{+}(y_o^{+},\theta_L)\} + \alpha u_{oL}^{+}(y_o^{+},\theta_L) \tag{5.3}$$

where $u_p^{+}(y^{+})$ is the predicted signal, $u^{*}(y^{+})$ is the universal signal, α, β, and θ_L are the universal parameters and $u_{oL}^{+}(y_o^{+},\theta_L)$ is the large-scale input from a position in the log-region. It should be noted here that the outer probe large-scale signal in the formulation for FST cases, $u_{oL}^{+}(y_o^{+},\theta_L)$, is different compared to a canonical case because for FST cases the large-scale signal also includes the FST large-scales that penetrate into the boundary layer. It is also worth mentioning that the two probes in the present study are both moving whereas only the inner probe moved with the outer probe fixed in Mathis et al. (2011a). However, here, the inner probe moves significantly in wall units whereas the outer probe can be said to be relatively fixed relative to the main features of the flow. Therefore, this difference in the probe configuration is not expected to affect the results.

Briefly, the predictive model incorporates four different things: (i) a universal signal, u^{*}, that would exist in the absence of any large-scale influences (ii) the inclination of the large-scale structures with the wall, θ_L, which will lead to a time-delay in the interaction, (iii) the superposition of the large-scale fluctuation on the near-wall region, represented by model coefficient α, and (iv) amplitude modulation of the small scales by the superimposed large scales, represented by model coefficient β.

The three aforementioned parameters of the predictive model for different wall-normal locations are given in Figure 5.7 in comparison with the values from Mathis et al. (2011a). The superposition coefficient is related to the correlation between the large-scale fluctuations of the two probes, the relation of which has already been demonstrated

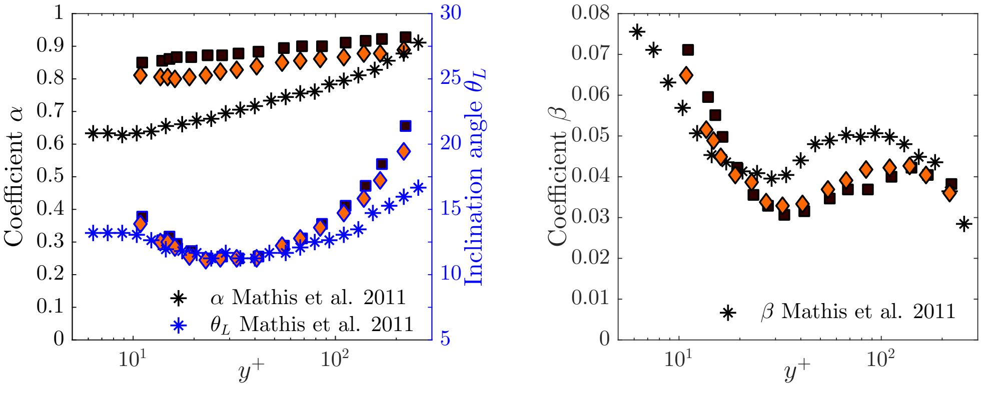

(a)

(b)

Figure 5.7: Wall-normal evolution of the predictive inner-outer model coefficients. (a) the superposition coefficient α and the mean inclination angle of the large-scale structures, θ_L (the blue outlined markers); (b) the amplitude modulation coefficient, β. (◆) case B and (■) case D. Marker symbol (✳): values from Mathis et al. (2011a).

in Figure 5.5 (middle plot) instantaneously at one specific wall-normal location. This coefficient is found as the value at the maximum of the cross-correlation between the large-scale components of the inner and outer probes as

$$\alpha = \ max\left(R_{u_L^+(y^+)\ u_L^+(y_o^+)}\right) \tag{5.4}$$

where

$$R_{u_L^+(y^+)\ u_L^+(y_o^+)} = \frac{\overline{u_L^+\left(y^+,t\right)\ u_L^+\left(y_o^+,t+\Delta t\right)}}{\sigma_{u_L^+(y^+)}\ \sigma_{u_L^+(y_o^+)}} \tag{5.5}$$

Here, when looked at the evolution of the coefficient in wall-normal direction for all locations below the outer spectral peak, a high degree of correlation can easily be seen throughout. This correlation is higher for case D (higher turbulence intensity) compared to case B (lower turbulence intensity). This confirms the observation from the spectrograms that the energy levels that reside in the near-wall region due to the penetration of FST increase with turbulence level in the free-stream (see Figure 5.3). When compared with α values from Mathis et al. (2011a), higher values are observed for FST cases. This is a result of FST scales penetrating the boundary layer. The model takes into account the inclination angle of the large-scale structures which corresponds to the streamwise shift at the maximum correlation (assuming Taylor's hypothesis). That is $\theta_L = \arctan\left(\Delta y/\Delta x\right)$ where Δx is calculated for the corresponding time shift between the large-scale signals from both probes using Taylor's hypothesis and Δy is the distance between the probes. The inclination angle, θ_L, is typically found to be within 12°and 16°, c.f., Mathis et al. (2011a) and references therein including Brown and Thomas

(1977); Robinson (1986); Marusic and Heuer (2007). The present study exhibits similar large-scale structural organisation with an inclination angle that is relatively constant between 11°< θ_L <15° for wall-normal locations $y^+ < 150$. Although FST disturbs the boundary layer from outside, the fact that it does not destroy the large-scale structural organisation in the log-region is a promising result to establish the analogy with the high Reynolds number canonical flows. Beyond that wall-normal location where the two probes get closer in wall-units (in physical units the probes are a set distance apart), the angle is found to increase and reach around 20° as justified by the presence of increasingly correlated small-scale structures that have higher inclination angles (Mathis et al., 2011a). The fact that this angle is even higher for FST cases can also be justified by the presence of FST small scales in addition to the boundary layer small scales.

Knowing α and θ_L, the outer probe signal can be shifted forward in the streamwise direction for the corresponding θ_L. The prediction formula (refer to Equation 5.3) takes the form of a de-trended signal with a right-hand side expression only with unknowns of $u^* \left(y^+\right)$ and β. The details of how to iteratively solve for $u^* \left(y^+\right)$ and β can be found in Mathis et al. (2011a). The value of β, which captures the modulation effect of the large scales on the envelope of the small scales in the turbulent boundary layer, gives similar results to the canonical case studied in Mathis et al. (2011a) especially in the near-wall region. Nonetheless, the trend in β is observed to be similar to the trend in R (Figure 5.3(iii)), which was also true for the canonical case of Mathis et al. (2011a). Since R indicates how much the signal is amplitude-modulated, β would be expected to indicate a similar trend to de-amplitude modulate this signal in order to remove the large-scale influence as similarly justified in Mathis et al. (2011a). This similarity also confirms that amplitude modulation of the scale interactions in the near-wall region is reasonably well represented in this “simulated” high Reynolds number flow. The magnitude of this coefficient is found to be smaller compared to the canonical case in Mathis et al. (2011a). When this model was applied to non-canonical cases like turbulent boundary layers subjected to pressure gradients in Mathis et al. (2015), the β values were similarly observed to be smaller compared to the canonical case in Mathis et al. (2011a). Agostini and Leschziner (2014) claimed that although this predictive model correctly represents the superposition effects of the large scales through the superposition coefficient α, it does not capture entirely the asymmetry in the modulation with β coefficient. If the β results are to be interpreted based on their observations, these asymmetries could be said to be stronger for a non-canonical flow and therefore additional factors might come into play when calculating β.

Finally, the universal signal can be determined using these model parameters. Since this signal is “universal” and thus independent of any large-scale influence, the signal for the two FST cases would not be expected to differ significantly. This can also be deduced through the variance distribution of the two signals determined as the universal signals for the two FST cases in Figure 5.8. The discrepancy between the two cases could be attributed to the fact that the model parameters were estimated based on the lower turbulence case and the calibration experiment (i.e. the present experiment to calculate the model coefficients) has limited range of wall-normal positions to correspond to the outer peak location of the higher turbulence case.

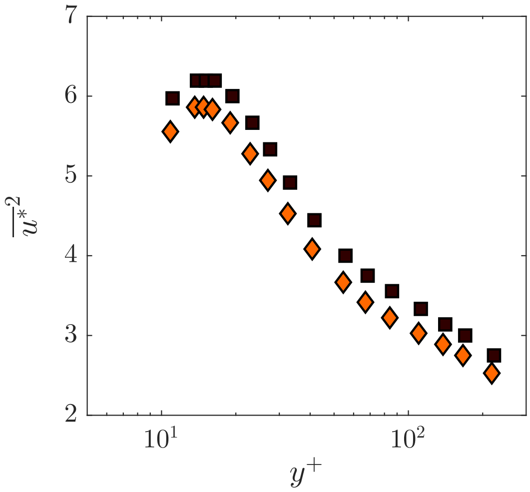

Figure 5.8: Variance distribution of the universal signal, u^*, in y^+ for (◆) case B and (■) case D.

Once these model parameters are established, the signal in the near-wall region can be predicted by using only large-scale signal input from a nominal peak in the outer region. Figure 5.9 presents the predicted and the measured values for the variance of the near-wall peak. Here, the aim is to validate the above model for the inclusive set of FST cases in addition to the two particular cases from multi-wire measurements. The predicted values are corrected for spatial resolution using the method of Chin et al. (2009). The prediction seems to work quite well for the FST cases with 75% R-squared value calculated for the identity line. The discrepancies from the equality line can be mainly due to (i) the difference in spectral filtering used for the scale separation and (ii) the limited wall-normal position range of the calibration experiment that could pose an inefficiency of the method for the cases where the spectral outer peak location is out of the calibrated range. Regardless, the validity of the model suggests that this approach could be generalised to capture the influence of “any” large-scale influence on near-wall turbulence.

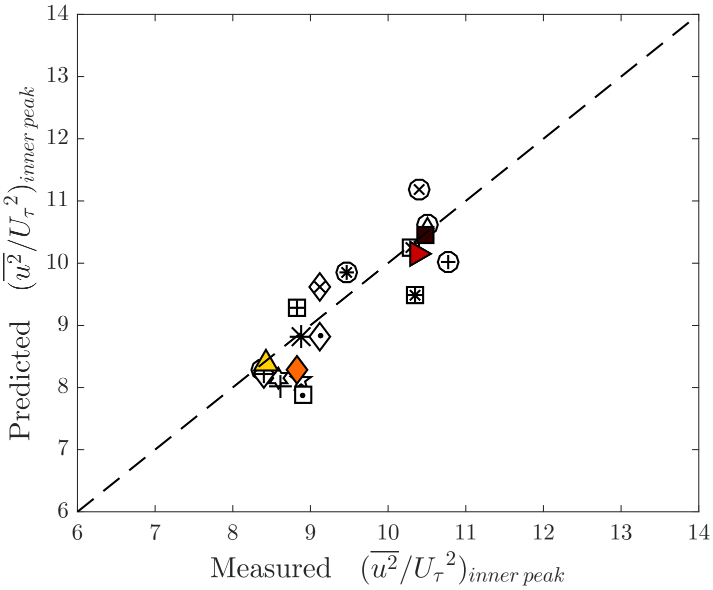

Figure 5.9: Predicted vs measured values of the near-wall peak amplitude of the variance of the streamwise velocity fluctuations. Conditions for (▲) case A; (◆) case B; (▶) case C; (■) case D can be found in Table 3.2. Conditions of the cases for all other data markers are found in Table 3.3. Dashed line is a representative line for equality of the two values.

5.6 Phase information: Single point measurements

A phase difference between the large and small scales was found for amplitude modulation in previous studies and it was observed to increase with increasing distance from the wall (Bandyopadhyay and Hussain, 1984; Chung and McKeon, 2010; Ganapathisubramani et al., 2012). Since the amplitude modulation coefficient is a correlation coefficient between the large scales and the envelope of the small scales, it could help define the phase relationship between them. However, Jacobi and McKeon (2013) noted the nature of the phase relationship was obscured when examined with the correlation coefficient since the correlation is computed at zero time-lag while a phase difference necessarily means a non-zero time-lag. Therefore, they suggested employing the cross-correlation function itself. Following their suggestion, the time shift (or the phase difference) relationship across the whole boundary layer is investigated in Figure 5.10 with cross-correlation contour maps from single point measurements. The phase difference is positive across the whole boundary layer implying that the envelope of the small-scale fluctuations leads the large-scale fluctuations in the boundary layer, in agreement with previous work (Chung and McKeon, 2010; Ganapathisubramani et al., 2012; Jacobi and McKeon, 2013). This phase difference is found to increase with wall-normal position, also in agreement with previous studies (Bandyopadhyay and Hussain, 1984; Chung and

McKeon, 2010; Guala et al., 2011; Ganapathisubramani et al., 2012; Jacobi and McKeon, 2013). However, unlike previous studies, the phase reversal is not observed for FST cases. This might be related to the increased small-scale fluctuations in the outer region of the boundary layer resulting from the FST. Nonetheless, the inner region phase relations are similar to a canonical boundary layer, which is promising as it indicates that the present methodology can be used to approximate the phase organisation of the large scales and the envelope of the small scales in high Reynolds number flows.

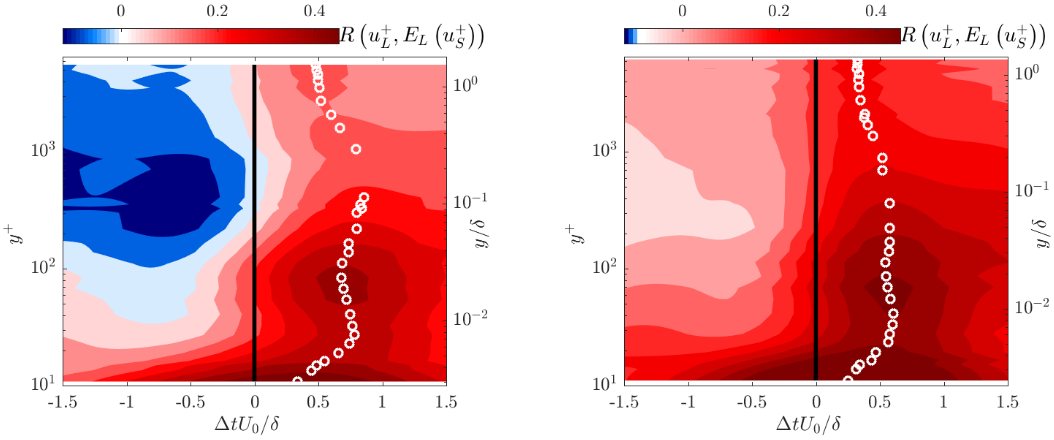

(a)

(b)

Figure 5.10: Contour maps of the cross-correlation between the large scales and the filtered envelope of the small-scales, $R(u_L^+, E_L(u_S^+))$. White circle markers depict the maximum correlation points. (Left) case B; (right) case D. The ordinates show the wall normal location, y, plotted in both inner (left) and outer (right) scaling. The abscissas show the time domain in outer scaling.

As mentioned previously in Section 5.2, Duvvuri and McKeon (2015) showed that the phase relations naturally existing in the flow between the scales can be modified by introducing a synthetic large scale. To reiterate, they suggested that the envelope of all small scales can be in-phase or out-of-phase with the synthetic large scale depending on its location with respect to the location of the critical layer and they interpreted the zero-crossing location of their amplitude modulation coefficient as an indication of phase reversal, which in turn could point to the presence of the critical layer. The present amplitude modulation coefficient plots (Figure 5.3(iii)) do not cross zero. This suggests that the critical layer tends to move towards the free-stream for higher intensity disturbances (and/or disturbances that are over a range of scales). This also implies that for broadband, high intensity forcing in the free-stream, it might not be possible to match the wave speed of a given disturbance to the mean velocity within the boundary layer and therefore the small- and large-scales remain in-phase. It must be noted that the wave speed of the disturbances in these FST cases is not known. However, if one assumes Taylor's hypothesis for FST, the energetic motions that are injected by the active grid in the free-stream would be expected to advect at the mean velocity of the free-stream. If this is the case, then, it would not be possible for the local mean within the boundary layer to match the "wave speed" of the external disturbance. It is also plausible that a penetrated FST disturbance might travel within the boundary layer at a "wave speed" between the local mean and the free-stream velocity. In this case, one would expect to find a critical layer inside the boundary layer. However, since the disturbances have a broadband spectrum, the critical layer of each disturbance would be expected to be weak and therefore would result in a smeared collection of critical layers across which the phase can change only gradually. Since both explanations could lead to lack of phase reversal, further extensive work on phase relationships in the presence of broadband forcing is needed for any firmer conclusions.

5.7 Summary

For the analyses in this chapter, the scales in the boundary layer were decomposed using a cut-off wavelength filter as previously done by Hutchins and Marusic (2007a) and Mathis et al. (2009). By investigating the scales separately, the increasing effect of large-scales on the near-wall region with increasing turbulence level was made clear. In addition to low-wavenumber energy (related to large-scales) superimposed in the near-wall region, a modulating interaction was also observed between the scales which was revealed first by the skewness analysis using the cross-term of the scale-decomposed skewness factor, $3\overline{\overline{u_L^+ u_S^{+}}^{2}}$. Later, this modulation was quantified by the modulation coefficient, R, as previously done in the literature by Mathis et al. (2009). The scale interactions observed in the boundary layer subjected to FST resembled those of a high Reynolds number boundary layer. The predictive inner-outer model of Marusic et al. (2010b) was implemented for the present cases in order to test the analogy between these flows. The analogy was confirmed by comparing the present model coefficients to those of high Reynolds number flows. Since the aim of the model is to be able to predict the near-wall turbulence with only large-scale input, this analogy implies that there is some universality, even under extreme free-stream conditions, of the large-scale influence on the near-wall turbulence.

It was also found that the envelope of the small-scale fluctuations led the large-scale fluctuations in the boundary layer as previously found for a canonical boundary layer (Chung and McKeon, 2010; Ganapathisubramani et al., 2012; Jacobi and McKeon, 2013). The inner region phase relations of a canonical boundary layer were well captured here indicating the ability of the FST cases to maintain the phase organisations observed in canonical high Reynolds number flows.

Chapter 6

Statistical and structural analyses of PIV data

6.1 Introduction

In this chapter, some results from the planar PIV measurements are presented and spatial characteristics of the turbulent boundary layer in the presence of FST are discussed. These features are compared to temporal characteristics where applicable. The results and discussions are restricted to the reduced data set of FST cases B and D which will be mainly referred to here as low and high turbulence level cases, respectively.

6.2 Mean and variance profiles

6.2.1 Streamwise velocity

Streamwise velocity component has been extensively analysed in the previous chapters. However, in order to show consistency between methods, mean and variance profiles of the streamwise velocity are replotted to compare the PIV results with hot-wire measurements. As can be clearly seen from Figure 6.1, the two methods match very well. Here, the advantage of having hot-wire measurements for the very near-wall information should be noted.

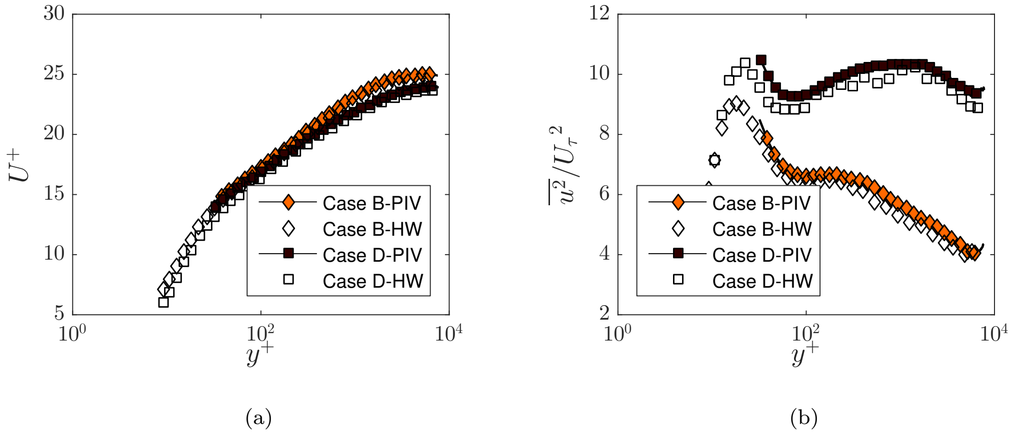

Figure 6.1: (a) Mean and (b) variance profiles of the streamwise velocity component from both PIV and hot-wire. Markers on the PIV data curve are interpolated data points for clear representation. Symbols are explained in the legend.

6.2.2 Wall-normal Velocity

PIV enables us to obtain wall-normal velocity information in a plane. This velocity component has not been examined in the previous chapters. Here, we present the mean and statistical results of this vertical velocity. The inner-normalised mean profiles of the wall-normal velocity in Figure 6.2(a) shows a near-wall similarity between the two FST cases. This is interesting as the effect of the turbulence level in the free-stream can be accounted for with the increase in the skin friction, U_τ, and this similarity can be achieved. The distinction between low and high turbulence level case can be easily seen starting from the mid log-region where FST is known to be present as a result of the direct penetration and clearly high-turbulence case is penetrating more strongly with higher mean wall-normal velocities.

Recently, an outer scaling has been proposed for mean wall-normal velocity by Wei and Klewicki (2016) and this scaling is also tested for the FST cases in Figure 6.2(b). The profiles certainly exhibit better collapse with this scaling; however, a complete similarity is lacking and the reasons for this are unknown. It is possible that the free-stream turbulence and the degree of randomness inflicted by its presence reduces the fidelity of this scaling. It should be noted that the boundary layer thickness (δ) from PIV measurements is defined as the height at which the mean turbulence intensity profile is within 1% of the turbulence intensity in the free-stream. This boundary layer definition was chosen because, as previously discussed, a traditional δ_{99} definition did not produce a reliable estimate of the boundary layer thickness due to a wide scatter around the mean free-stream velocity and iterative method from Perry and Li (1990) that was used previously for hot-wire measurements could not be used effectively due to insufficient near wall resolution to converge the integral scheme.

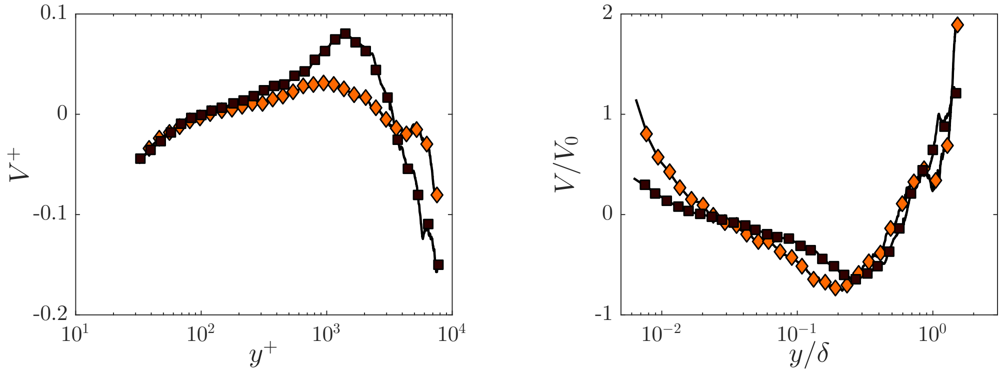

(a)

(b)

Figure 6.2: Mean wall-normal velocity profile in (a) inner-scaling (b) outer scaling proposed by Wei and Klewicki (2016). (◆) case B; (■) case D. Markers on the PIV data curve are interpolated data points for clear representation.

The variance profiles of the wall-normal velocity fluctuations are given in comparison with the channel flow data from Lozano-Durán and Jiménez (2014) at a comparable Re_τ in Figure 6.3. This comparison to channel flow is based on the observations in the previous chapters that the streamwise velocity component from hot-wire measurements (§4.2) is similar to the streamwise velocity in a channel flow. The lower turbulence case seems to follow the channel flow data better than the higher turbulence case. The near-wall similarity up to mid-log region is observed and as expected the distinction between high and low fluctuations is more obvious between the two cases higher up in the boundary layer towards the free-stream. This suggests that the free-stream turbulence appears to set the skin-friction velocity and the flow responds proportionally to the increase in skin-friction. In an integral sense, this is understandable as the momentum flux from a surface should be related to the drag experienced by this surface. Therefore, the velocity fluctuations should be expected to scale with skin-friction velocity. However, the degree of similarity between the three profiles in the inner region is remarkable. The fidelity of this scaling for the momentum flux (i.e. Reynolds shear stress) is examined in more detail in the next section.

The right axis of the figure (blue outlined) is given as normalised with the variance of the streamwise velocity fluctuations of the free-stream. This would also give information about the isotropy of the flow in the free-stream. The isotropy ratio can be defined as $I = \frac{\sqrt{\overline{u_0^2}}}{\sqrt{\overline{v_0^2}}}$. The isotropy (or anisotropy thereof) is found to be around 1.4 for case B and around 1.3 for case D. These values are slightly higher than the previous active grid studies that similarly followed Makita's original active grid design (Larssen and

Devenport, 2011; Kang et al., 2003). However, the anisotropy is mostly associated with the largest scales of the flow and since in this study the u fluctuations are forced to be large-scale (such that the spectral peak was at 10δ), the lack of isotropy is expected.

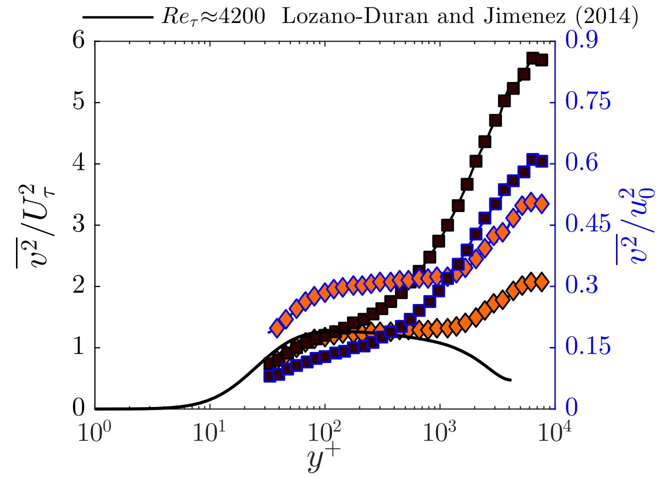

Figure 6.3: Variance profiles of the wall-normal velocity fluctuations. The ordinates show the profiles in (left) inner-normalised and (right) free-stream-variance normalised (blue outlined). (◆) case B; (■) case D; solid black line: Lozano-Durán and Jiménez (2014). Markers on the PIV data curve are interpolated data points for clear representation.

6.3 Reynolds shear stress profiles

Generation of Reynolds shear stress is believed to be the main source for the maintenance of turbulence and increased drag on the surface. Therefore, it is of interest to see how Reynolds shear stress profiles behave under the effect of FST. Figure 6.4(a) shows the shear stress correlation coefficient, also known as velocity correlation coefficient. For higher turbulence case, this coefficient is lower as expected since the penetration is higher for this case. The effect of the penetration of uncorrelated, large-scale FST is to reduce the velocity correlations. This effect is similarly shown in Hancock and Bradshaw (1989) and Thole and Bogard (1996). They also suggested that these uncorrelated large-scales from the free-stream have only small contribution to Reynolds shear stress in the inner region.

Figure 6.4(b) shows profiles of Reynolds shear stress for two different FST cases. The wall-normal location is plotted in inner-coordinates while the shear stress is normalised by skin-friction velocity. The figure shows that although for higher turbulence case the penetration is higher, it does not result in higher mean values for the inner-scaled Reynolds shear stress. Also in this figure, the channel flow data from Lozano-Durán and Jiménez (2014) is plotted as comparison. Low turbulence case B, seems to follow the channel data better than high turbulence case D. Once again, despite the large amount of disturbance in the free-stream, the momentum flux in the near-wall region appears to scale with local skin-friction velocity regardless of the turbulence intensity in the free-stream. This is consistent with the observations for the vertical component. However, this behaviour is markedly different from the behaviour of streamwise velocity component where scaling with skin-friction velocity did not collapse the profiles.

It is also worth noting that the shear stress profiles exhibit an extended plateau region with increasing turbulence level. This is similar to a "higher" Reynolds number canonical flows where the extent of the plateau increases with increasing Re_τ. This further strengthens analogy between high Reynolds number canonical flow and boundary layer under increasing effect of FST.

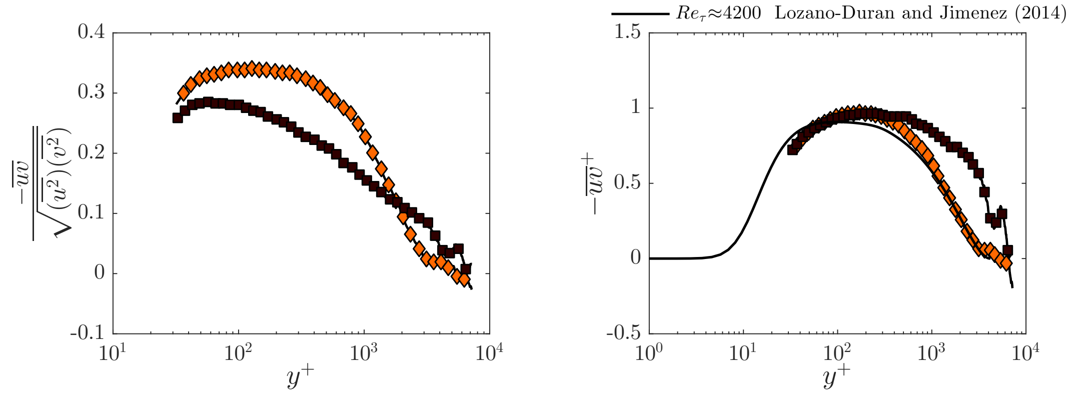

(a)

(b)

Figure 6.4: (a) Shear stress correlation coefficient and (b) inner-normalised Reynolds shear stress profiles. (◆) case B; (■) case D; solid black line: Lozano-Durán and Jiménez (2014). Markers on the PIV data curve are interpolated data points for clear representation.

Figure 6.5 shows the contours of the instantaneous Reynolds shear stress for a representative case. Considerable amount of Reynolds shear stress production can be detected instantaneously from this snapshot, i.e. uv product values as high as $10U_\tau^2$. With the addition of more turbulence in the free-stream (case D), this has been observed to increase even more (figure not shown here). These instantaneous momentum transport events can be characterised by examining its distribution through the boundary layer and comparing this to other canonical flows.

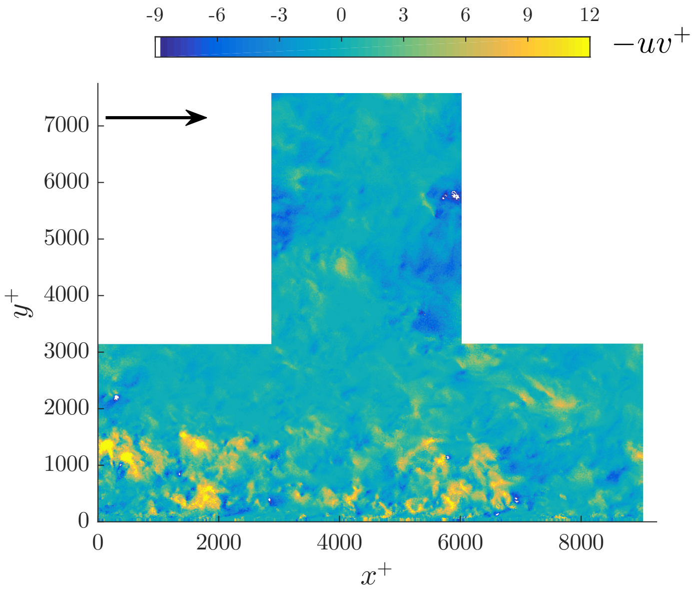

Figure 6.5: Contour plot of instantaneous inner-normalised Reynolds shear stress ($-uv^+$) for case B. Flow is from left to right.

6.3.1 Distribution of uv events

After examining the mean profiles of the Reynolds shear stress, it is important to see how uv events are distributed across the boundary layer. One can refer to Appendix A for the pdfs of the individual velocity components, u and v. Figure 6.6 shows the contour maps of the normalised pdfs of instantaneous shear stress for the two FST cases. Across the whole boundary layer, both pdfs are skewed towards negative values which is consistent with the sign of the mean Reynolds shear stress (Figure 6.4(b)). This demonstrates that the dominant contributions to total Reynolds stresses are from negative shear stress events of sweeps ($u > 0$, $v < 0$) and ejections ($u < 0$, $v > 0$) and they outweigh the contributions from positive shear stress events of inward ($u < 0$, $v < 0$) and outward ($u > 0$, $v > 0$) interactions.

When profiles are extracted at various wall-normal locations, the distributions for both FST cases can be compared as done in Figure 6.7. At $y^+ \approx 100$, where the mean Reynolds shear stress collapse, the pdfs seem to differ for the most intense uv events, i.e. at the tails of the distribution. This shows the effect of increasing turbulence intensity on the intense ejection and sweep events. This again is analogous to an increase in Reynolds number for a canonical wall-bounded flow (Corino and Brodkey, 1969). For the outer region location, $y/\delta \approx 0.2$, higher turbulence case shows a clear distinction in the distribution as also expected from the mean Reynolds shear stress profile where the two FST cases do not collapse anymore.

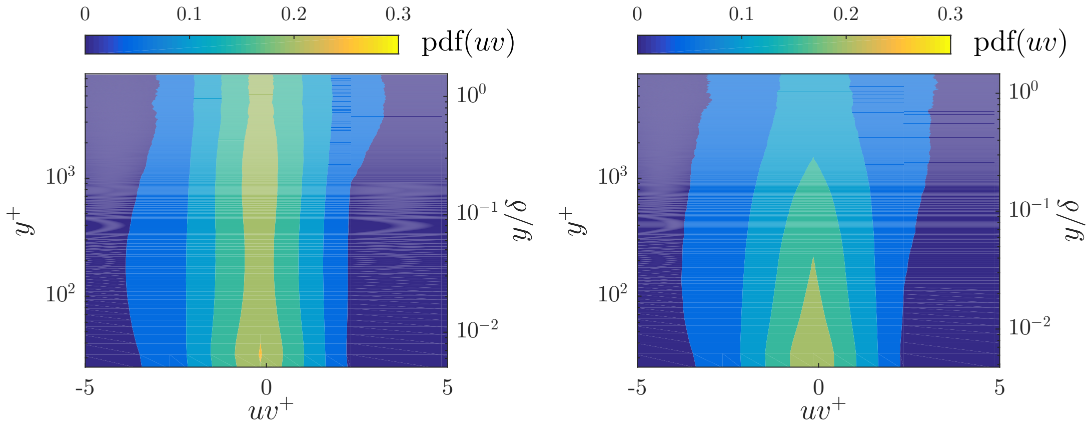

(a)

(b)

Figure 6.6: Contour maps of the normalised pdf of uv. The ordinates show the wall-normal location in inner (left) and outer (right) scaling. (a) case B (b) case D.

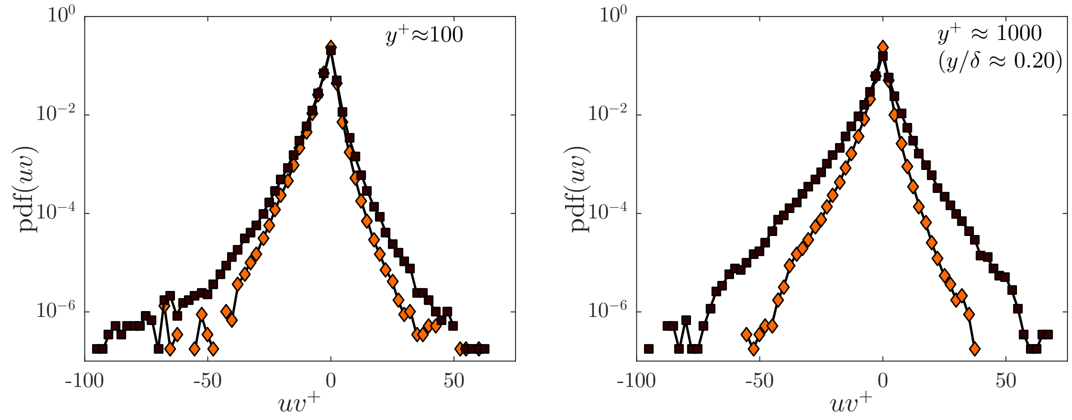

(a)

(b)

Figure 6.7: Comparison of the pdfs of the two FST cases at two wall-normal locations (a) $y^+ \approx 100$ (b) $y/\delta \approx 0.2$. (◆) case B; (■) case D.

6.3.2 Quadrant Analysis

The above analysis showed how the probability distribution of uv product is skewed towards either positive or negative events. To determine the contributions of different positive and negative events, conditional averaging of this product is needed based on the quadrant analysis introduced by Wallace et al. (1972) and Lu and Willmarth (1973). They suggested that there is useful information contained in the signs of the individual velocity fluctuations. They also exploited this by classifying the products of these fluctuations into four categories which they later called quadrants of the Reynolds shear stress plane: Q1 ($+u$, $+v$), Q2 ($-u$,$+v$), Q3 ($-u$, $-v$), and Q4 ($+u$, $-v$). Events in the second quadrant, Q2, correspond to negative streamwise fluctuations (low-speed) being lifted away from the wall by positive wall-normal fluctuations, and they are referred to as *ejections*. Events in the fourth quadrant correspond to positive streamwise fluctuations (high-speed) being moved towards the wall by negative wall-normal fluctuations and these motions are called *sweeps*. Q1 and Q3 are called outward and inward interactions. This type of quadrant analysis does not specify the form of the eddies creating sweeps and ejections, but it allows to evaluate the contributions these events make to the total mean values of various quantities (Adrian, 2007).

The Reynolds shear stress can be written as follows:

$$\overline{uv} = \int\int_{-\infty}^{\infty} uvP(u,v)dudv \tag{6.1}$$

where $P(u,v)$ is the joint probability density function and $uvP(u,v)$ is the covariance integrand, i.e. a weighted joint pdf. The integral of this covariance integrand over a differential area $dudv$ represents the contribution of that particular pair of u and v to the covariance $\overline{uv}$ both in sign and magnitude. When plotted on $u-v$ plane, this covariance integrand will be zero on each axis by its definition; therefore, the distribution of contributions to Reynolds shear stress will be distinctly split into four quadrants.

Figure 6.8 shows covariance integrands of u and v at various wall-normal locations for both FST cases. The larger contributions are clearly seen to be from Q2 and Q4 events for both cases. In these quadrants, for high turbulence case D, the extent of the elliptical shape of the covariance integrand is larger. This shows the effect of increasing turbulence level in the free-stream on the intensity of these quadrant events. As the wall-normal location increases, the elliptical shape of the weighted joint pdf becomes more circular and the fractional contributions from Q1 and Q3 events also increase. For a turbulent boundary layer with no-FST, the ejections (Q2 events) are known to be dominant above the buffer layer throughout the boundary layer (Lu and Willmarth, 1973; Jiménez et al., 2010). However, for a turbulent boundary layer under the effect of FST, the contribution from sweep events is comparable to the contribution from ejections and it even outweighs for high turbulence case D. This can be justified with the penetration of free-stream fluctuations into the boundary layer, i.e. increasing negative wall-normal velocity fluctuations.

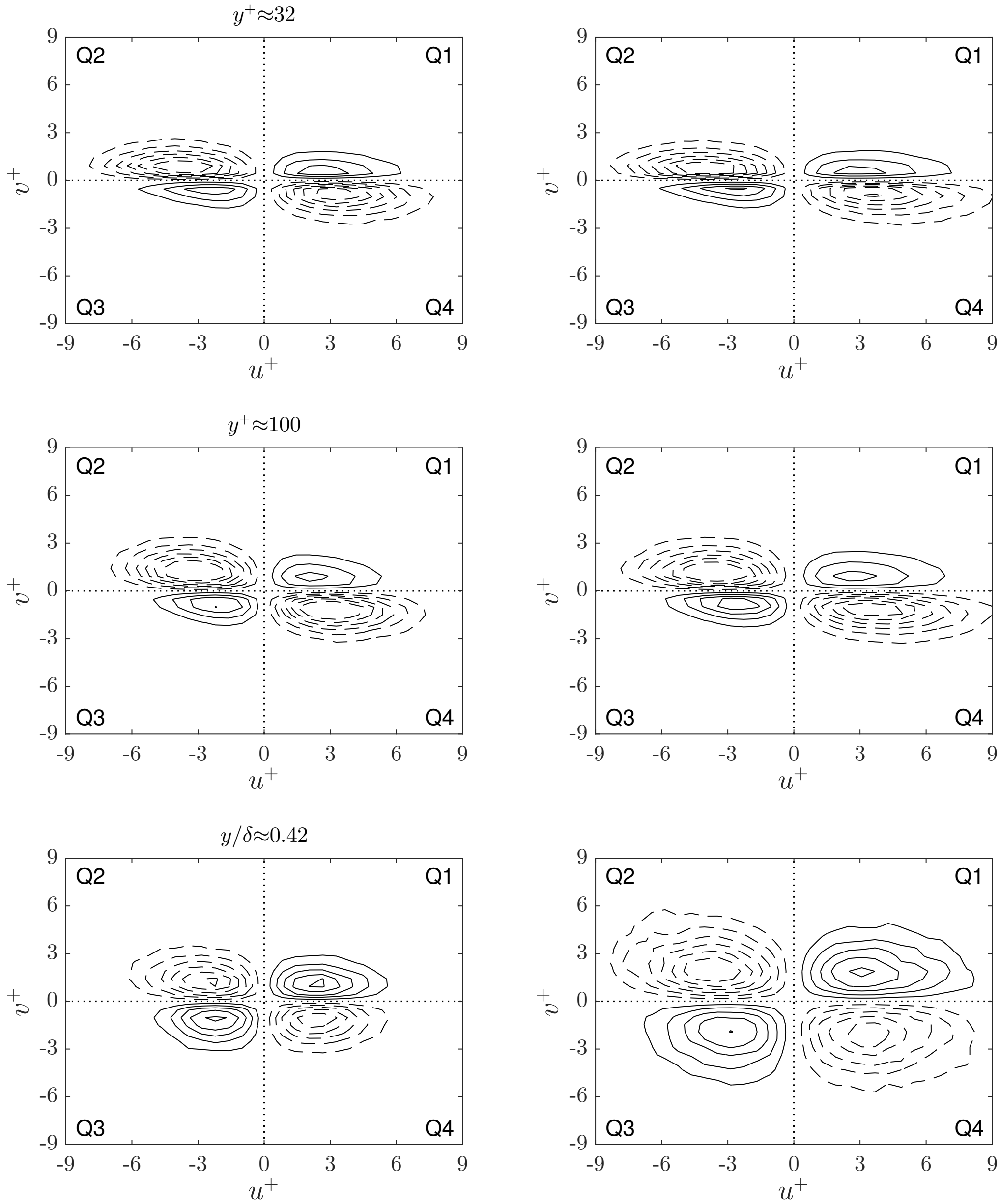

Figure 6.8: Covariance integrands of u and v fluctuations (left) case B (right) case D at various wall-normal locations: (top) $y^+\approx32$ (middle) $y^+\approx100$ and (bottom) $y/\delta\approx0.42$. Negative contours are shown with dashed lines. The outermost contour level is ±0.01 and the increment is 0.01 for positive contours and -0.01 for negative contours. Zero contours are not shown.

To focus on the intense occurrences of the Reynolds shear stress, Willmarth and Lu (1972) extended the quadrant analysis by introducing a hole filtering. The uv plane is divided into five regions as schematically shown in Figure 6.9(a). In the figure, the shaded region is called "hole" and is bounded by $|uv|$ = constant lines. Here, a hole size, h, is defined as a threshold to exclude uv events of small magnitude to determine the relative contributions of the more intense uv events. The fractional contributions from each quadrant, Q, can be calculated with the relation given below following Lu and Willmarth (1973).

$$\frac{\widetilde{uv}|_{Q_i}}{\overline{uv}} = \frac{1}{\overline{uv}}\left(\frac{1}{N}\sum_{n=1}^{N} uv|_i S_i(h)\right) \qquad i \ = 1,4 \tag{6.2}$$

and where N is the total number of samples and

$$S_i\,(h) = \begin{cases} 1, & \text{if } |uv| \ \geq \ h\sqrt{\overline{u}}\sqrt{\overline{v}} \ \text{ and } (u,v) \text{ pair is in the } i^{th} \text{ quadrant of the } u-v \text{ plane,} \\ 0, & \text{otherwise} \end{cases} \tag{6.3}$$

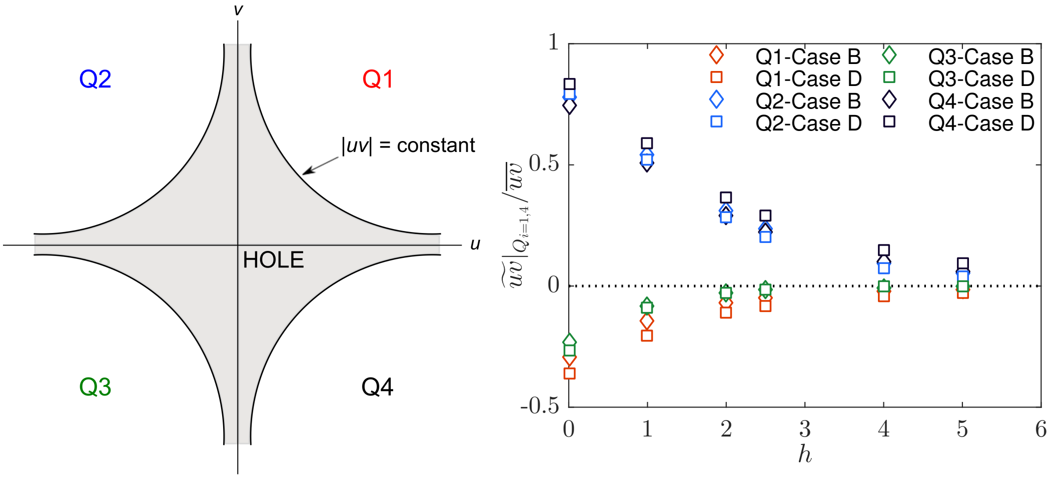

(a) (b)

Figure 6.9: (a) Schematic illustrating quadrant splitting of the $u-v$ plane with shaded hole region (b) Fractional contributions to the Reynolds shear stress by each quadrant at $y^+{\approx}40$ for various hole sizes, h, for both FST cases. Symbols are explained in the legend.

Different hole sizes are tested as representatively illustrated for a wall-normal location of $y^+{\approx}40$ in Figure 6.9(b). Bogard and Tiederman (1986) reported that the optimum threshold for the buffer region is $h{\approx}1$, based on direct comparisons between the detected events and instantaneous visualisations of the flow. Lozano-Durán et al. (2012) was also able to get comparable results for bursts in the buffer region for their threshold value of 1.75 and they also observed that their results are qualitatively similar within the range of $1 \leq h \leq 3$. For the present study, h value is chosen as 2.

Figure 6.10 presents quadrant contributions with a hole size of h = 2 for both cases. It is obvious that the dominant contributors are Q2 and Q4 events for both cases. The outward and inward interactions, Q1 and Q3, respectively, contribute very little to the total Reynolds shear stress. These interaction events have been observed to be more active towards the edge of the boundary layer in the presence of FST as opposed to a canonical turbulent boundary layer. This feature is similarly found in channel flows as the increased contribution of the two dominant quadrants, Q2 and Q4, near the centreline of the channel is compensated by a parallel increase of the contributions from the quadrants Q1 and Q3 (Jiménez et al., 2010). This similarity can be justified by common intermittency characteristics of the two flows, i.e. channel flow and the turbulent boundary layer under the FST effect. Sweeps are slightly more dominant for high turbulence case D than low turbulence case B up to $y/\delta{\approx}0.5$. This could be explained by stronger penetration of FST for case D. The contributions from sweeps and ejections for case D seem to be almost equal across the boundary layer. For case B, the ejections seem to be the main contributor to the Reynolds shear stress. This shows that the near-wall fluctuations are still dominant in their own right for this case.

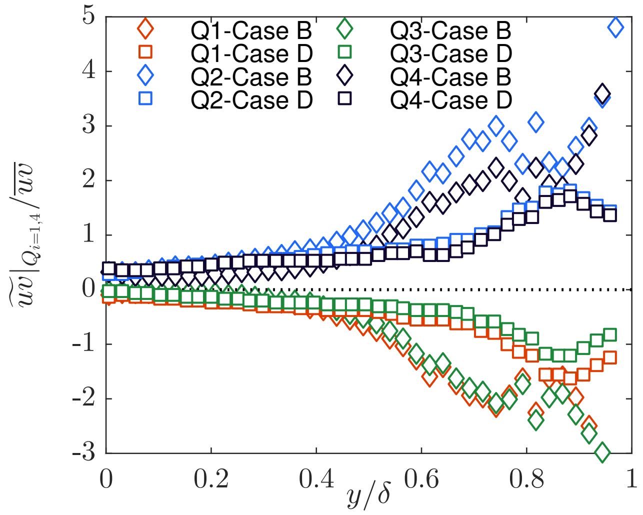

Figure 6.10: Distribution of quadrant contributions based on the hole size of $h = 2$ for both FST cases. Symbols are explained in the legend.

The ratio of Q2 to Q4 events is given in Figure 6.11. Ejections seem to be dominant for almost the whole boundary layer for low turbulence level case B. On the other hand, for case D, sweeps are dominant up to $y/\delta{\approx}0.1$ from which ejections take over. It is also interesting to note that the ratio Q2/Q4 exhibits higher values for low turbulence case B than high turbulence case D. It is possible that, for case B, the near-wall ejections did not encounter as strong suppression from sweeps towards the wall as it is for case D. This also reveals the robustness of near-wall ejections despite high free-stream fluctuations for both cases. This ratio stays in the range 1.5-2 for channel flows and reaches 3 for a canonical boundary layer at $y{\approx}\delta$ (Jiménez et al., 2010) and present study cases are noticeably closer to channel flows.

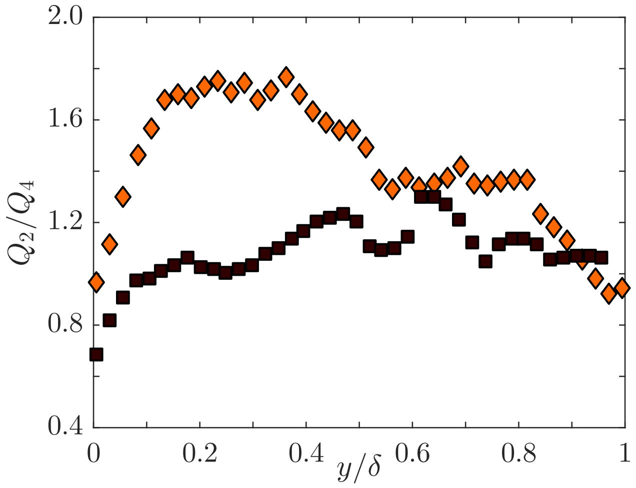

Figure 6.11: Distribution of the ratio Q2/Q4. (◆) case B; (■) case D.

Quadrant analysis identifies the distributions of the events associated with the high- and low-speed fluid; however, to investigate how these high- and low-speed fluid regions are organised in the flow, velocity correlations are required. For this purpose, the next section will present the two-point spatial correlations.

6.4 Velocity correlations

To provide an estimate of the dimensions of the scales that are involved in generating Reynolds shear stress and in creating the coherent motions of sweeps and ejections, two-point space-time correlations are useful. In a shear flow, when the variable measurement location is displaced throughout the flow relative to a fixed measurement location, the shape and extent of the iso-correlation contours reveal information about the shape and size of the flow structures underlying the correlation (Wallace, 2014). Here, in this study, using the planar PIV, the streamwise-wall-normal plane spatial correlations can be computed. The two-point correlation coefficient between any two quantities R_{AB} is defined as (Ganapathisubramani et al., 2005):

$$R_{AB} = \frac{\overline{A\,(x,y)\,B\,(x+\Delta x, y+\Delta y)}}{\sigma_A \sigma_B} \tag{6.4}$$

where, σ_A and σ_B are the standard deviations of the quantities of interest A and B, respectively and Δx and Δy are the streamwise and wall-normal separations, respectively, between these two components. The multiple realisations are ensemble averaged to obtain the correlation coefficient and the overline notation denotes this averaging. Based on this definition, velocity correlations are computed at every wall-normal location in relation to every other location in the boundary layer. Figure 6.12 shows the two-point auto-correlations for the streamwise velocity fluctuations, R_{uu}, computed at different wall-normal locations for both cases. Note the abscissa shows the streamwise distance in both upstream and downstream distance.

In the near-wall (Figure 6.12a), the contour lines are confined to a relatively small region. As the reference wall-normal location for the correlation calculations move away from the wall, i.e. in the log layer and above (Figure 6.12b-e), the contour lines are more elongated and cover an extended region as similarly observed in canonical flows (Ganapathisubramani et al. (2005); Tutkun et al. (2009) among many others). Correlation contours weaker than 0.1 are not shown on the figure; however, it has been noticed that the outer layer is physically connected to every other layer of the boundary layer down to the wall, albeit weakly correlated. This shows the coherence of the structures inside the boundary layer even in the presence of FST. The negative correlations appear to be stronger and more elongated at higher wall-normal locations in the boundary layer. The wall-normal extent of these negatively correlated structures is observed to significantly increase above the log-region (Figure 6.12e). It is obvious that the field of view of the present measurements is too short to capture the entire extent of these elongated structures. The positive correlations have inclined features which will be discussed in more detail in the following paragraphs.

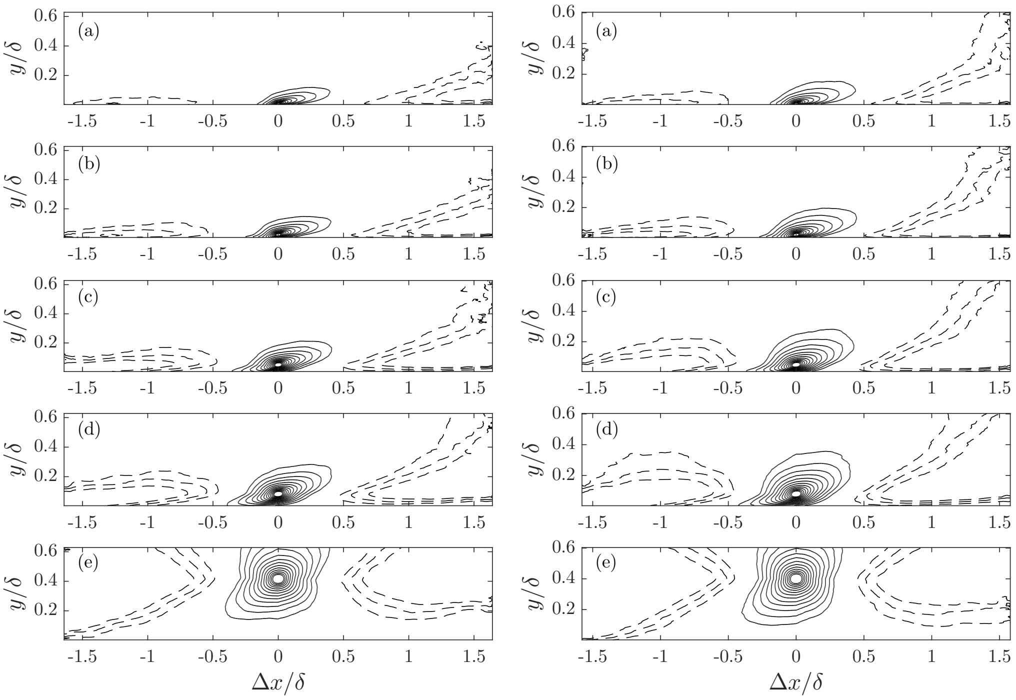

Figure 6.12: R_{uu} correlation computed at different wall-normal locations. (a) $y^+ \approx 40$ (b) $y^+ \approx 100$ (c) $y^+ \approx 240$ (d) $y^+ \approx 400$ (e) $y/\delta \approx 0.4$. (Left) case B (right) case D. Negative contours are shown with dashed lines. The outermost contour level is ±0.1 and the increment is 0.05 for positive contours and -0.05 for negative contours. Zero contours are not shown.

To be able compare the structure sizes for both FST cases, Figure 6.13 presents a specific contour level tracked for these cases for the wall-normal locations as chosen above. There is very little difference in the extent and shape of the structures between the two cases. Even the way these structures are inclined seem to be similar for both cases. This suggests that the change in the free-stream turbulence level does not affect the structural organisation of the flow in the streamwise-wall-normal plane. This finding, when taken together with the findings of structural similarity of flow over rough walls (Jiménez, 2004; Flack et al., 2005; Placidi, 2015) suggests that a universal structural similarity is present. The structure of boundary layer does not seem to depend on the boundary conditions. This is remarkable since the extent of disturbance in this case is over 10% (in FST level), which is stronger than the near-wall peak turbulence intensity in a canonical flow.

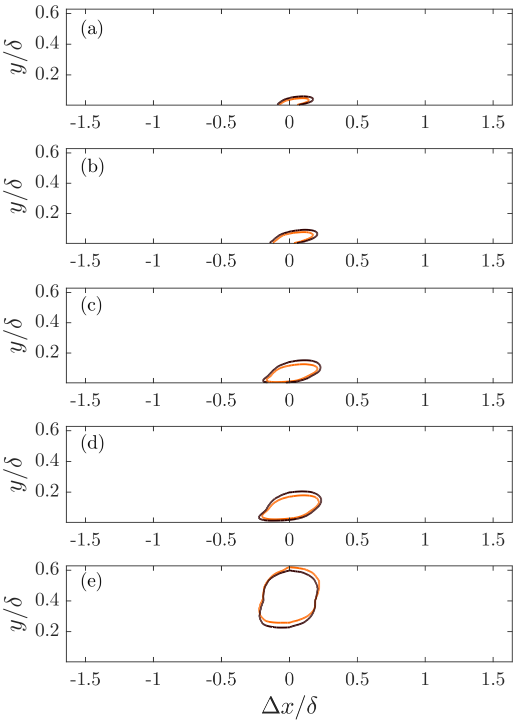

Figure 6.13: R_{uu} correlation comparison for FST cases at different wall-normal locations (a) $y^+ \approx 40$ (b) $y^+ \approx 100$ (c) $y^+ \approx 240$ (d) $y^+ \approx 400$ (e) $y/\delta \approx 0.4$. Representative contour level is 0.25. — case B; — case D.

It has been well-established in the literature that the outer layer of a canonical boundary layer contains inclined structures that are associated with ejections and sweeps (Brown and Thomas, 1977; Head and Bandyopadhyay, 1981). Adrian et al. (2000b) referred to these structures, that are coherently aligned in the streamwise direction creating a large-scale coherent motion, as the hairpin vortex packets. Their model supported the existence of vortex organisation both in the near-wall and outer layer of the flow. One of the characteristic feature of these packets, as mentioned previously in Chapter 1, is the streamwise alignment of a series of hairpin vortices, inclined away from the wall at angles between 12°and 20° (Christensen and Adrian, 2001). However, the present study is not focused on the specific coherent structures that create this organisation. Here, the structural organisation underlying the correlation contours will be presented. For this purpose, the inclination angle can be estimated from the correlation contours by assuming an elliptical shape for a constant contour level and determining the angle of the major axis of the fitted ellipse. As one might recall from Chapter 5, the inclination angle of the large-scale structures were also obtained from multi-wire measurements using the streamwise shift between the inner and outer probe signals (using Taylor's hypothesis). Figure 6.14 shows the results from these two methods (note that the PIV wall-normal extent is limited according to the available measurement range of multi-wire measurements). These two methods both give compatible results. The discrepancy in the last few points might be due to the use of Taylor's hypothesis for hot-wire data. Nonetheless, the inclination angle of the structures is found to be consistent with the literature and, to reiterate, suggests promising results for the analogy between high Reynolds number flows and the present study cases as the structural organisation inside the boundary layer is not altered despite the external disturbance from FST.

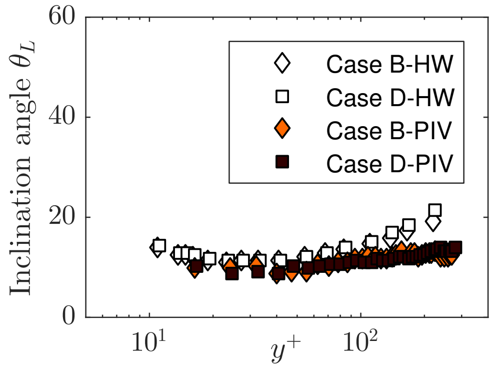

Figure 6.14: Comparison of the inclination angle, θ_L, obtained through hot-wire and PIV measurements. Symbols are explained in the legend.

Figure 6.15 shows R_{uu}, R_{vv} and R_{uv} correlations at two representative wall-normal locations in comparison for the two FST cases. There is essentially no significant difference among the cases for none of the correlations. As mentioned before, an increase in the free-stream turbulence level, i.e. penetration of higher energy fluctuations into the boundary layer, does not affect the extent and size of the structures inside the boundary layer in the plane of interest, i.e. streamwise-wall-normal plane. The sharp drop of R_{vv} correlation at $y^+\approx100$ is worth to note suggesting that the streamwise coherence in v fluctuations is quite short. In the outer region, $y/\delta\approx0.42$, the streamwise extent increases due to higher interactions with the free-stream and the direct penetration of FST, hence the increased v fluctuations, into the boundary layer in this region. R_{uv} correlations at $y^+\approx100$, similar to R_{uu}, have long streamwise coherence. The negative values also suggest that the low-speed fluid is associated with an upwash over long streamwise distances (Ganapathisubramani et al., 2005). There is also slight asymmetry, albeit hardly noticeable, which becomes more apparent in the outer region, $y/\delta \approx 0.42$.

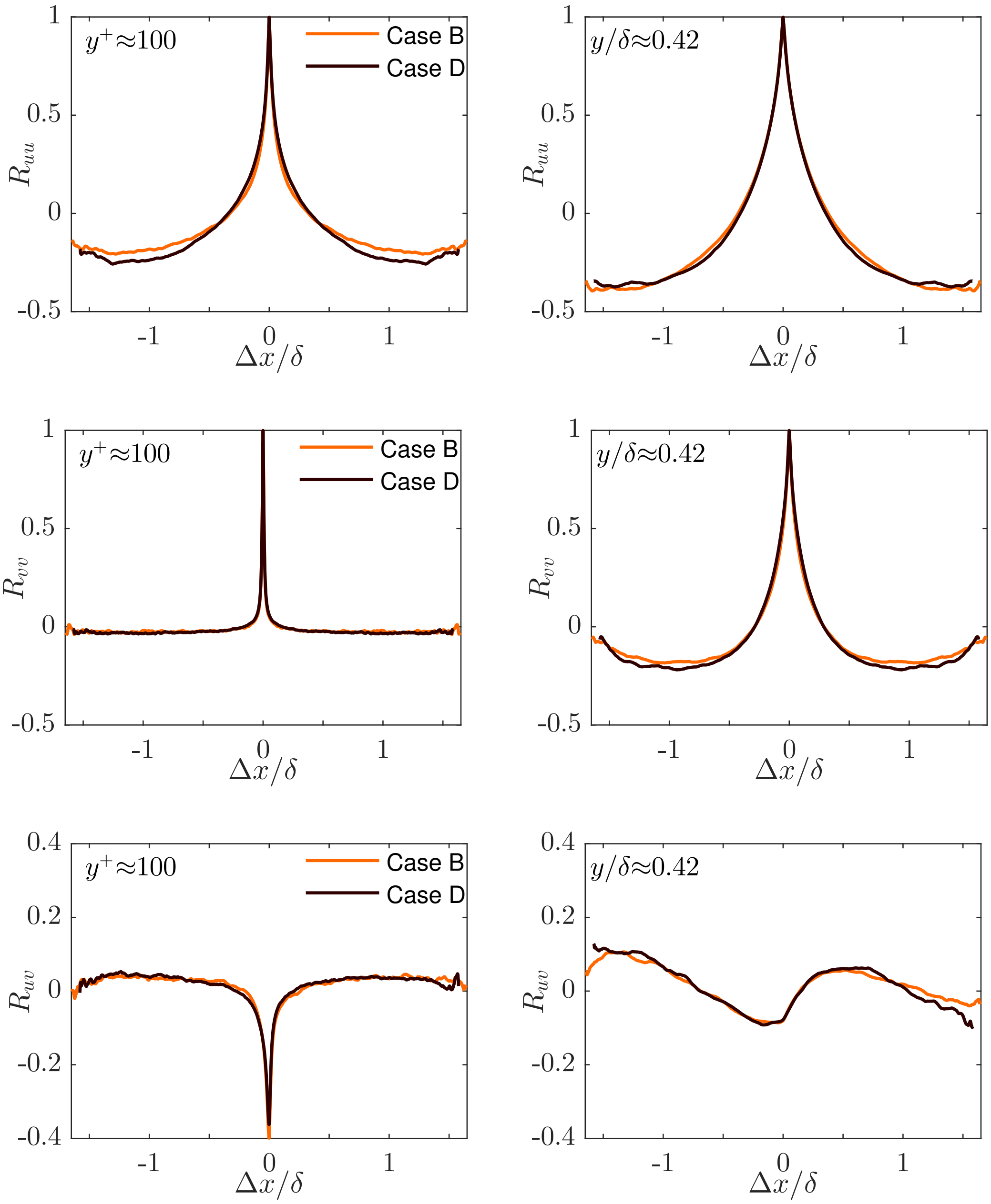

Figure 6.15: (Top) R_{uu} (middle) R_{vv} (bottom) R_{uv} correlations at (left) $y^+ \approx 100$ and (right) $y/\delta \approx 0.42$ for both FST cases. — case B; — case D.

Representative streamwise and wall-normal length scales can be estimated from the correlations by choosing a contour level (Christensen and Wu, 2005). Figure 6.16 shows these length scales for R_{uu} and R_{vv} correlations in comparison for both cases for a contour level of 0.5. Since the scales are dependent on the chosen contour level, these plots will only reveal the trends of the length scales in the boundary layer. Lx of R_{uu}

correlations seem to stay constant for both cases for the wall-normal range presented. This trend is similar to a channel flow (Christensen and Wu, 2005). Ly of R_{uu} correlations almost collapse for two cases and show a gradual increase above the log-region. It should be noted that the wall-normal length scales are presented for $y/\delta \geq 0.03$ as below this location, the contours are almost merging with the wall and it is hard to infer wall-normal extents of these contours.

For Lx of R_{vv}, it can be seen that the length scales start from quite small values (almost zero) due to low streamwise coherence of R_{vv} as previously mentioned. For these length scales, high turbulence case D have slightly higher values than low turbulence case B. This could be justified by different penetration levels of these two cases as higher penetration would be related to higher wall-normal fluctuations in the boundary layer. A decrease of Ly above y/δ≈0.4 for case D and above y/δ≈0.45 for case B has been observed and this could be related to the uncorrelated free-stream fluctuations dominantly present in this region.

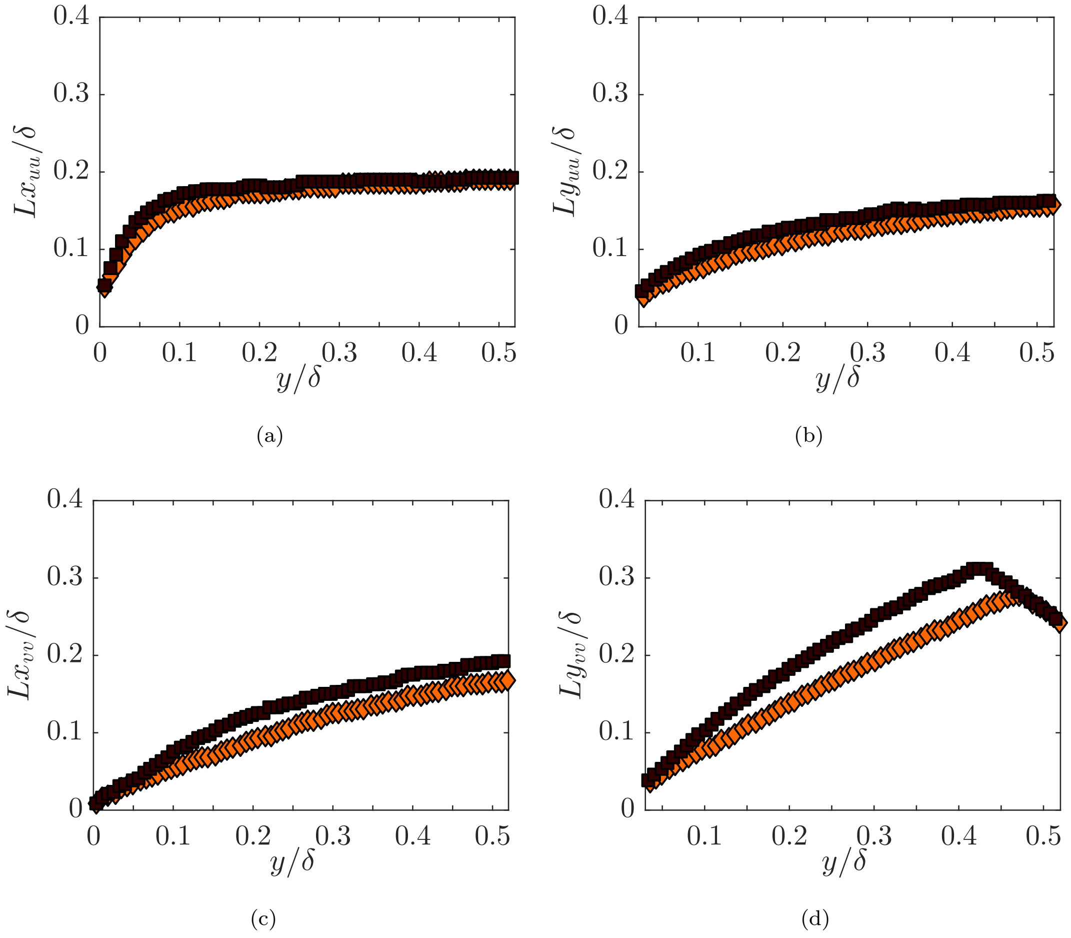

(a)

(b)

(c)

(d)

Figure 6.16: Wall-normal variation of (a-c) streamwise and (b-d) wall-normal length scales based on $R_{uu} = 0.5$ and $R_{vv} = 0.5$ for both FST cases. (◆) case B; (■) case D.

6.5 Summary

This chapter dealt with PIV data. The analysis of this data added further statistical and structural information for the flow of interest. Wall-normal velocity and Reynolds shear stress profiles were observed to follow the inner-scaling which has been found contrary to the streamwise fluctuations. Addition of free-stream turbulence into the flow resulted in an extended plateau region around the local peak for Reynolds shear stress profiles. Increasing the level of FST resulted in further extension of that plateau. This effect was found similar to high Reynolds number canonical flows for increasing Re_τ.

Quadrant analysis was employed to determine the contributions of different Reynolds-stress-producing events. The dominant contributors were found to be sweep and ejection events in the boundary layer. The outward and inward interaction events were observed to contribute very little until towards the edge of the boundary layer. These results suggested a degree of similarity in momentum transport between the present cases and channel flows.

Two-point velocity correlations were presented. The streamwise velocity autocorrelations showed structures that are coherent for extended distances in streamwise direction whereas the wall-normal velocity correlations were found to be quite short in streamwise coherence. The inclination angle of these coherent structures was estimated using the correlation contours and the value was found to be consistent with the literature. This study might potentially support the claim for the structural similarity across all wall-bounded flows as the structures were found statistically identical with previous studies like on rough walls. Finally, some representative length scales were estimated from the correlations and discussed to reveal the trend in the length scales inside the boundary layer in the presence of FST.

The two-point correlations reveal the existence of large-scale coherent features of the flow. To further isolate the instantaneous structure of coherence, vortex detection schemes need to be implemented. However this is not the scope of the present study. To give a brief idea about the flow structure, Appendix B presents some instantaneous snapshots of vorticity and signed swirling strength for both FST cases.

Chapter 7

Conclusions

In this study, large-scale FST, generated by an active grid, was imposed on a zero-pressure-gradient turbulent boundary layer as an external disturbance. The characteristics of the turbulent boundary layer in the presence of FST was investigated. Particular attention was given to scale interactions within the boundary layer. The study was conducted as an experimental work using hot-wire anemometry and PIV. The outcomes of the study will be summarised below in light of the questions posed in §1.4

The effects of FST on the skin friction and boundary layer integral parameters were found to be consistent with the previous studies. Mean streamwise velocity profiles exhibited an extended logarithmic region (in wall units). This has important implications for the overlap argument of the turbulent boundary layer as the law of the wall can extend up to higher wall-normal locations (in wall units) without being dictated by the outer scales in the boundary layer. Due to the presence of external turbulence, there was no intermittent region at the edge of the boundary layer; therefore, the wake region of the boundary layer was suppressed. In this respect, FST cases were found to resemble channel flows.

Streamwise velocity fluctuation profiles reflected the penetration of high free-stream fluctuations into the boundary layer as they demonstrated higher turbulence intensities across the whole boundary layer compared to a no-FST case. The level of amplification was observed to increase with increasing FST level. The trend in the near-wall peak amplitude of FST cases with increasing FST level was found analogous to high Reynolds number flows for increasing Re_τ. This led to the detailed investigation of energy distribution within the boundary layer in the presence of FST. The results from the spectral analyses confirmed the penetration of large-scale FST into the boundary layer very near the wall as evident with increased energy levels of long-wavelengths in that region. The results also showed two distinct energy peaks in the boundary layer with the addition of FST. The outer one of these energy peaks was imposed by FST large-scales and occurred at the same wavelength as these scales. The energy level of the outer peak was detected to increase with the increase in FST level. The formation of outer spectral peak and the increase of its energy level with increasing Re_τ have been observed as the characteristics of high Reynolds number flows in the recent findings in the literature and this has been attributed to the more energetic large-scale structures at these high Reynolds numbers. These large-scales have been said to have footprint in the near-wall region as well as modulating the small-scales in that region. This suggested a similar interaction in the present study between the energetic large-scales in the outer region affected by large-scale FST and the near-wall small scales.

Scale decomposition with a sharp cut-off wavelength filter enabled separating the scales as large- and small-scales as previously done by Hutchins and Marusic (2007a) and Mathis et al. (2009). In the present study, the large-scales were observed to modulate the amplitude of the near-wall small scales. This modulating interaction was quantified using the skewness and correlation coefficient analyses. This added up to the analogy between the high Reynolds number flows and present study cases. The latest efforts in the community have been aimed towards predicting the near-wall turbulence using only the large-scale information input at high Reynolds number flows. A predictive model has recently been suggested by Marusic et al. (2010b) for canonical high Reynolds number flows for this purpose. The present study showed promising results for the application of the model for a non-canonical case and suggested some universality, even under extreme free-stream conditions, of the large-scale influence on the near-wall turbulence.

From the PIV data, the wall-normal velocity and Reynolds shear stress information were extracted. The profiles of the two quantities showed similarities between the low- and high-turbulence level cases (in inner scaling) in the near-wall region. This was noted to be in contrast to the inner-scaled streamwise fluctuating profiles. The distinction due to the increase in FST level was depicted in the outer region of the boundary layer. Investigation of the contributions of different turbulence-producing events to the mean Reynolds shear stress suggested resemblance of momentum transport between the present FST cases and channel flows. The common intermittency characteristics of the two flows was believed to play the main role in this similarity.

The structural organisation of the flow was presented using the two-point spatial velocity correlations. This enabled describing the coherence of the turbulent structures in the boundary layer. The inclination angle of the structures inferred from the correlation contours (and also from multi-wire measurements) was found to be consistent with the literature. This similarity implied that the structural organisation inside the boundary layer was not altered despite the external disturbance from FST. This signifies a potential universal structural representation of wall-bounded flows where the boundary conditions do not change the organisation of the structures but their strength.

7.1 Recommendations for further work

This study provided high quality data of a zero-pressure gradient turbulent boundary layer, particularly in the near-wall region, under the effect of FST, which was missing in the existing literature. In light of the outcomes of this study, further research would be encouraged both with the present data to complement the work and possible new data with different techniques to extend it.

This study focused on the effect of increasing turbulence level in the free-stream. FST cases that were investigated in detail had the same length scales but different turbulence intensity levels. A wider range of turbulence level cases could be interesting to look into whether there is a lower and/or an upper limit of turbulence level for the responses of the boundary layer to external disturbances. Similar experiments could be performed to explore the effects of changing FST length scales, i.e. by generating FST cases for similar turbulence intensity but at different length scales.

Current PIV data could be used to further analyse the instantaneous structures of the boundary layer. Feature identification algorithms could be used to detect those structures and the contributions to Reynolds shear stress from particular structures could be isolated. Further experiments could be performed using stereoscopic PIV to obtain the out-of-plane velocity component which would be valuable with the presence of highly fluctuating free-stream. Also PIV measurements on a different plane such as streamwise-spanwise plane would enable the investigation of spanwise structural organisation in the presence of external disturbance. This would ultimately provide useful information to contribute towards the proposition of structural universality.

Appendix A

Distribution of u and v fluctuations

High level turbulence case D exhibits more even distribution and higher fluctuations throughout the boundary layer for streamwise velocity fluctuations as shown in Figure A1. This is the evidence of higher penetration for this case. For lower turbulence case B, the near-wall has still its own dominance as the distribution of the fluctuations is wider than in the free-stream. When profiles are extracted at various wall-normal locations as in Figure A2, one can compare the trend in the distributions. For high turbulence case, collapsing profiles at different wall locations confirm the even distribution of u fluctuations throughout the boundary layer for this case. The figure also shows corresponding Gaussian distributions (dashed lines) and it has been observed that the distributions of the fluctuations become more Gaussian as the turbulence intensity increases. However, for both cases, the u distributions slightly depart from Gaussian towards positive side and this has been found consistent with the previous studies on active grid generated turbulence (Mydlarski and Warhaft, 1996; Sharp et al., 2009).

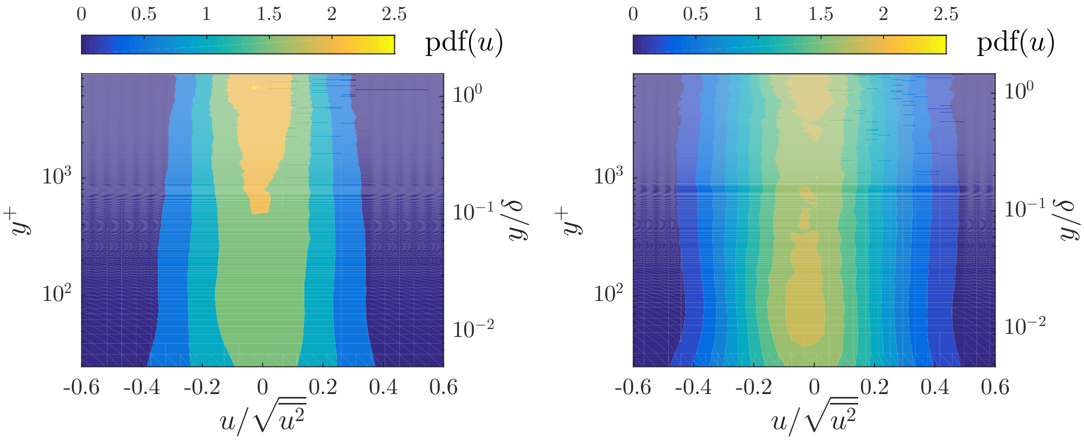

(a)

(b)

Figure A1: Contour maps of the normalised pdf of streamwise velocity, u. The ordinates show the wall-normal location in inner (left) and outer (right) scaling. (a) case B (b) case D.

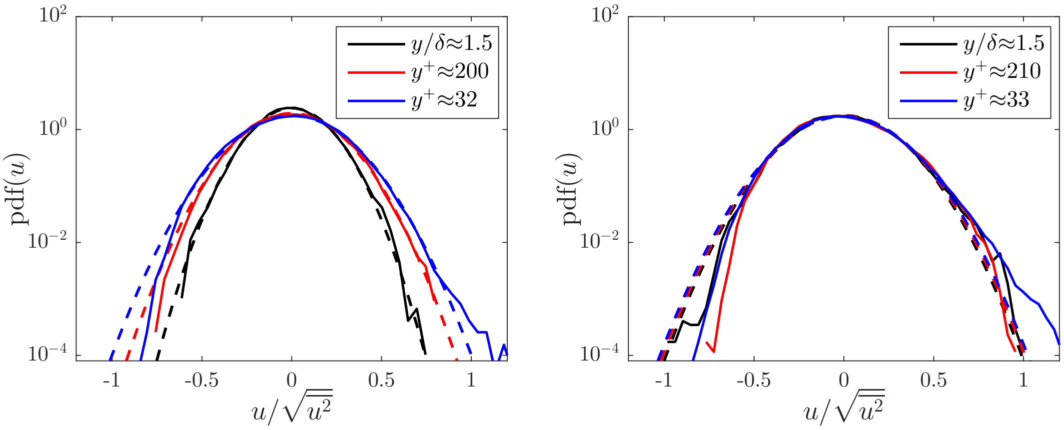

(a)

(b)

Figure A2: Comparison of the pdfs at various wall-normal locations (a) case B (d) case D. Dashed lines: corresponding Gaussian fit.

The distributions of the wall-normal velocity fluctuations for both FST cases are plotted in Figure A3. It appears that the distribution is narrower in the near-wall region than in the free-stream for both cases. Even though there is forcing in the free-stream, the presence of the wall blocks the distribution of the wall-normal component of the velocity. This is contrary to what has been observed from the distributions of the u fluctuations. As similarly done above, profiles can be extracted at various wall-locations (Figure A4). The distributions are observed to become narrower down into the boundary layer. From the tails of the distribution of both cases at the closest wall-normal location, $y^+{\approx}32$, it can be speculated that higher turbulence case encounters more resistance from the wall as the wall-normal velocity has a narrower tail for this case.

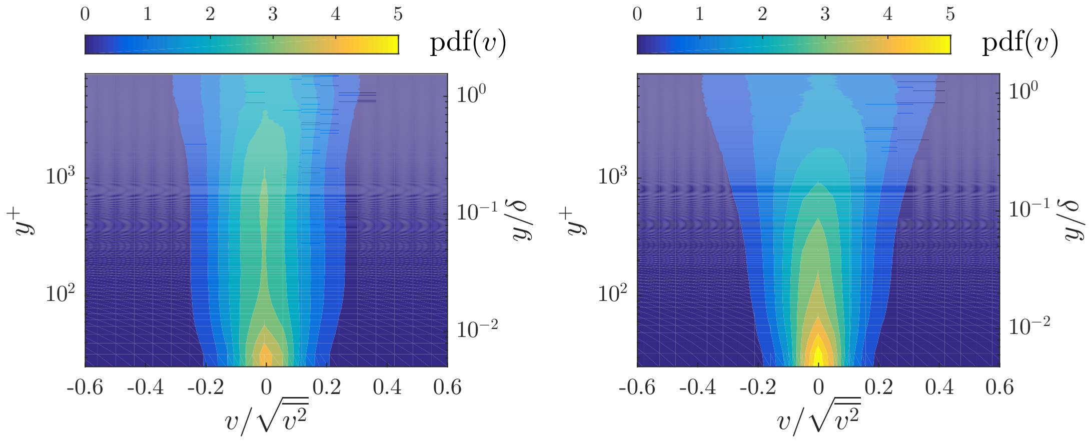

(a) (b)

Figure A3: Contour maps of the normalised pdf of wall-normal velocity, v. The ordinates show the wall-normal location in inner (left) and outer (right) scaling. (a) case B (b) case D.

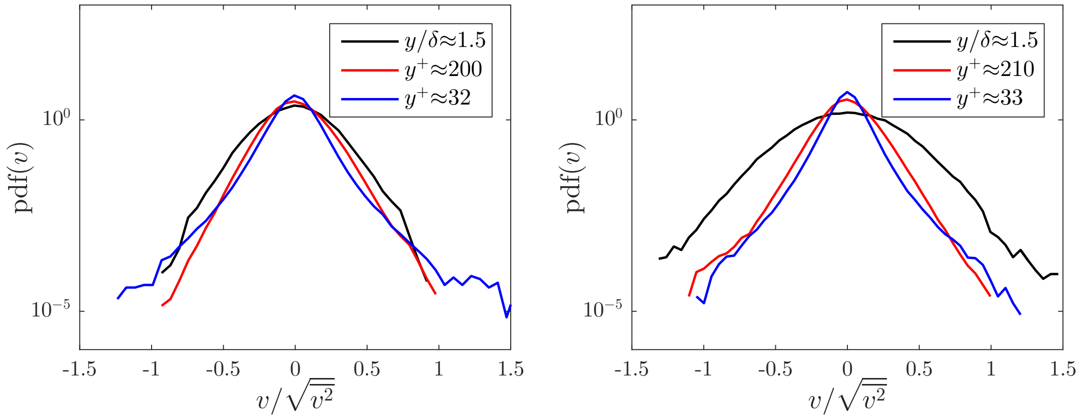

(a) (b)

Figure A4: Comparison of the pdfs at various wall-normal locations (a) case B (d) case D. Normalised pdf comparisons of v (a) low turbulence (b) high turbulence

Appendix B

Instantaneous fields of vorticity and swirling strength

Figure B1 shows the instantaneous snapshots for the spanwise vorticity component, ω_z, for both FST cases. With the increase of turbulence level in the free-stream, more vortical structures are observed. Streaky, tilted-up structures along the streamwise direction are better noticeable for high turbulence case D.

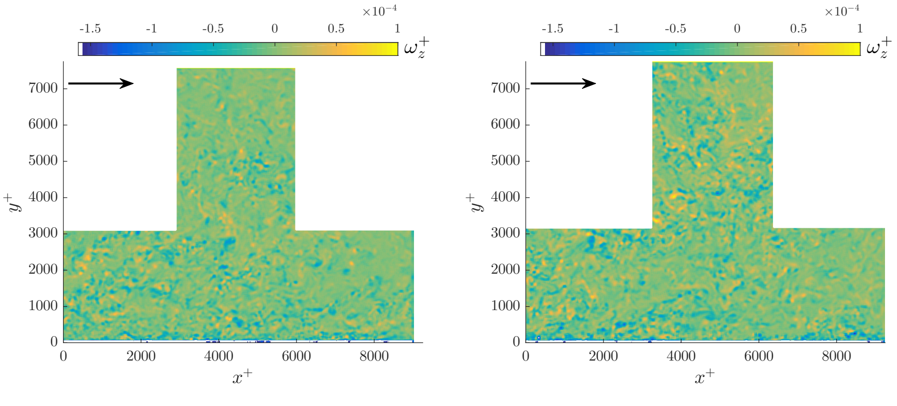

(a)

(b)

Figure B1: Contour plot of instantaneous inner-normalised vorticity, (ω_z^+) for (a) case B and (b) case D. Flow is from left to right.

Additionally, the probability distributions for the spanwise vorticity is presented in Figure B2. The width of the distributions decreases with increasing wall-normal distance. Higher vorticity values are observed for case D in the outer region as evident from wider distribution in that region. Logarithmic region seems to be dominated by negatively signed vorticity for both cases.

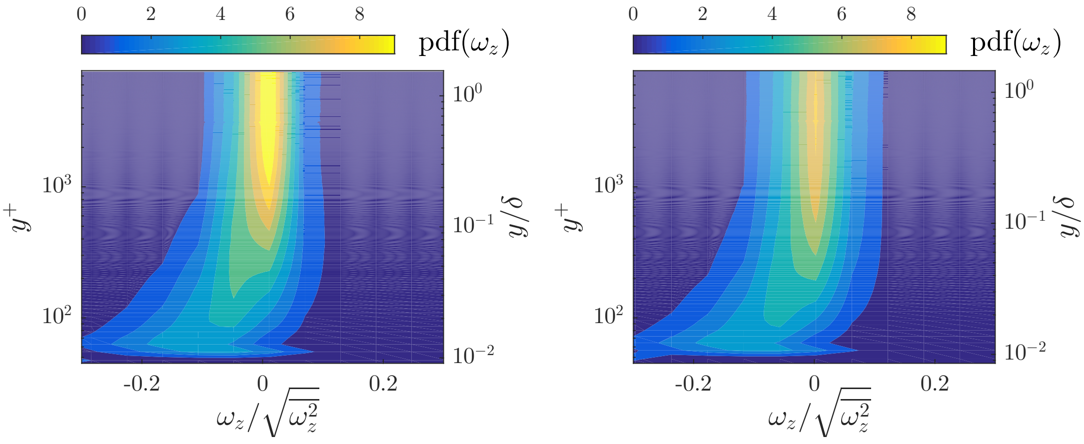

(a) (b)

Figure B2: Contour maps of the normalised pdf of vorticity, ω_z. The ordinates show the wall-normal location in inner (left) and outer (right) scaling. (a) case B (b) case D.

Swirling strength, λ_{ci}, is introduced to calculate reliable vortex statistics since vorticity cannot distinguish between pure shear flow and the actual swirling motion of a vortex (Adrian et al., 2000a). Swirling strength is defined as the imaginary part of the complex root of the velocity tensor. For details of swirling strength calculation, one can refer to Adrian et al. (2000a) and Ganapathisubramani (2004). Swirling strength is signed according to the sign of the vorticity and defined as signed swirling strength to indicate the sense of rotation of the vortices. Figure B3 presents signed swirling strength for both FST cases for the same instants presented above for vorticity snapshots. The swirling strength is non-zero only when the velocity vectors in that plane describe a local swirling motion (Christensen and Adrian, 2001). The increase in the strength of the vortex cores is noticeable for high turbulence level case D and the swirls are larger as well as stronger for this case.

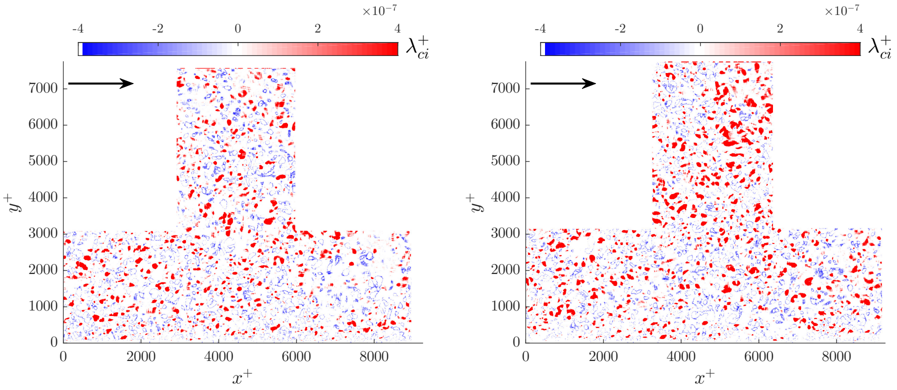

(a) (b)

Figure B3: Contour plot of instantaneous inner-normalised signed swirling strength, (λ_{ci}^+) for (a) case B and (b) case D. Flow is from left to right.

References

Adrian, J. R., Christensen, T. K., and Liu, Z.-C. (2000a). Analysis and interpretation of instantaneous turbulent velocity fields. *Experiments in Fluids*, 29(3):275–290.

Adrian, R., Meinhart, C., and Tomkins, C. (2000b). Vortex organization in the outer region of the turbulent boundary layer. *Journal of Fluid Mechanics*, 422:1–54.

Adrian, R. J. (2007). Hairpin vortex organization in wall turbulence. *Physics of Fluids*, 19(4):041301.

Adrian, R. J. and Westerweel, J. (2011). *Particle Image Velocimetry.* Cambridge Univ Press.

Agostini, L. and Leschziner, M. A. (2014). On the influence of outer large-scale structures on near-wall turbulence in channel flow. *Physics of Fluids*, 26(7):075107.

Balakumar, B. and Adrian, R. (2007). Large- and very-large-scale motions in channel and boundary-layer flows. *Philosophical Transactions of the Royal Society of London A: Mathematical, Physical and Engineering Sciences*, 365(1852):665–681.

Bandyopadhyay, P. (1992). Reynolds number dependence of the freestream turbulence effects on turbulent boundary layers. *AIAA Journal*, 30:1910–1915.

Bandyopadhyay, P. R. and Hussain, A. K. M. F. (1984). The coupling between scales in shear flows. *Physics of Fluids*, 27(9):2221–2228.

Blair, M. F. (1983a). Influence of free-stream turbulence on turbulent boundary layer heat transfer and mean profile development, part ii—analysis of results. *Journal of Heat Transfer*, 105:41–47.

Blair, M. F. (1983b). Influence of free-stream turbulence on turbulent boundary layer heat transfer and mean profile development, part i—experimental data. *Journal of Heat Transfer*, 105:33–40.

Bogard, D. G. and Tiederman, W. G. (1986). Burst detection with single-point velocity measurements. *Journal of Fluid Mechanics*, 162:389–413.

Breuer, K. (1995). Stochastic calibration of sensors in turbulent flow fields. *Experiments in Fluids*, 19(2):138–141.

Brown, G. L. and Thomas, A. S. W. (1977). Large structure in a turbulent boundary layer. *Physics of Fluids*, 20(10):S243–S252.

Bruun, H. H. (1995). *Hot-wire anemometry: principles and signal analysis.* Oxford science publications. Oxford Univ. Press, Oxford.

Brzek, B., Torres-Nieves, S., Lebrón, J., Cal, R., Meneveau, C., and Castillo, L. (2009). Effects of free-stream turbulence on rough surface turbulent boundary layers. *Journal of Fluid Mechanics*, 635:207–243.

Castro, I. P. (1984). Effects of free stream turbulence on low Reynolds number boundary layers. *Journal of Fluids Engineering*, 106:298–306.

Cekli, H. and Water, W. (2010). Tailoring turbulence with an active grid. *Experiments in Fluids*, 49(2):409–416.

Cekli, H. E. (2011). *How to stir turbulence.* PhD thesis, Eindhoven University of Technology.

Charnay, G., Mathieu, J., and Comte-Bellot, G. (1976). Response of a turbulent boundary layer to random fluctuations in the external stream. *Physics of Fluids*, 19(9):1261–1272.

Chin, C. C., Hutchins, N., Ooi, A. S. H., and Marusic, I. (2009). Use of direct numerical simulation (DNS) data to investigate spatial resolution issues in measurements of wall-bounded turbulence. *Measurement Science and Technology*, 20(11):115401.

Christensen, K. (2004). The influence of peak-locking errors on turbulence statistics computed from piv ensembles. *Experiments in Fluids*, 36:484–497.

Christensen, K. T. and Adrian, J. R. (2001). Statistical evidence of hairpin vortex packets in wall turbulence. *Journal of Fluid Mechanics*, 431:433–443.

Christensen, K. T. and Wu, Y. (2005). Characteristics of vortex organization in the outer layer of wall turbulence. In *TSFP Digitial Library Online*. Begel House Inc.

Chung, D. and McKeon, B. J. (2010). Large-eddy simulation of large-scale structures in long channel flow. *Journal of Fluid Mechanics*, 661:341–364.

Coles, D. (1956). The law of the wake in the turbulent boundary layer. *Journal of Fluid Mechanics*, 1:191–226.

Corino, E. R. and Brodkey, R. S. (1969). A visual investigation of the wall region in turbulent flow. *Journal of Fluid Mechanics*, 37:1–30.

Dogan, E., Hanson, R. E., and Ganapathisubramani, B. (2016). Interactions of large-scale free-stream turbulence with turbulent boundary layers. *Journal of Fluid Mechanics*, 802:79–107.

Dogan, E., Hearst, R. J., and Ganapathisubramani, B. (2017). Modelling high Reynolds number wall–turbulence interactions in laboratory experiments using large-scale free-stream turbulence. *Philosophical Transactions of the Royal Society of London A: Mathematical, Physical and Engineering Sciences*, 375(2089).

Duvvuri, S. and McKeon, B. J. (2015). Triadic scale interactions in a turbulent boundary layer. *Journal of Fluid Mechanics*, 767:R4.

Esteban, L. B. (2015). Free-stream turbulence effects on turbulent boundary layers. Master's thesis, University of Southampton.

Fernholz, H. and Finley, P. (1996). The incompressible zero-pressure-gradient turbulent boundary layer: An assessment of the data. *Progress in Aerospace Sciences*, 32(4):245 – 311.

Flack, K. A., Schultz, M. P., and Shapiro, T. A. (2005). Experimental support for townsend's reynolds number similarity hypothesis on rough walls. *Physics of Fluids*, 17(3):035102–.

Gad-El-Hak, M. and Corrsin, S. (1974). Measurements of the nearly isotropic turbulence behind a uniform jet grid. *Journal of Fluid Mechanics*, 62:115–143.

Ganapathisubramani, B. (2004). *Investigation of turbulent boundary layer structure using stereoscopic particle image velocimetry.* PhD thesis, University of Minnesota.

Ganapathisubramani, B., Hutchins, N., Hambleton, W. T., Longmire, E. K., and Marusic, I. (2005). Investigation of large-scale coherence in a turbulent boundary layer using two-point correlations. 524:57–80.

Ganapathisubramani, B., Hutchins, N., Monty, J. P., Chung, D., and Marusic, I. (2012). Amplitude and frequency modulation in wall turbulence. *Journal of Fluid Mechanics*, 712:61–91.

Ganapathisubramani, B., Longmire, E. K., and Marusic, I. (2003). Characteristics of vortex packets in turbulent boundary layers. *Journal of Fluid Mechanics*, 478:35–46.

Guala, M., Hommema, S. E., and Adrian, R. J. (2006). Large-scale and very-large-scale motions in turbulent pipe flow. *Journal of Fluid Mechanics*, 554:521–542.

Guala, M., Metzger, M., and McKeon, B. J. (2011). Interactions within the turbulent boundary layer at high reynolds number. *Journal of Fluid Mechanics*, 666:573–604.

Hancock, P. E. and Bradshaw, P. (1983). The effect of free-stream turbulence on turbulent boundary layers. *Journal of Fluids Engineering*, 105(3):284–289.

Hancock, P. E. and Bradshaw, P. (1989). Turbulence structure of a boundary layer beneath a turbulent free stream. *Journal of Fluid Mechanics*, 205:45–76.

Hanson, R. E. (2013). *Control of Transient Growth Induced Transition in a Zero–Pressure Gradient Boundary Layer Using Plasma Actuators.* PhD thesis, University of Toronto.

Head, M. R. and Bandyopadhyay, P. (1981). New aspects of turbulent boundary-layer structure. *Journal of Fluid Mechanics*, 107:297–338.

Hearst, R. and Lavoie, P. (2015). The effect of active grid initial conditions on high reynolds number turbulence. *Experiments in Fluids*, 56(10):185.

Hearst, R. J., Buxton, O. R. H., Ganapathisubramani, B., and Lavoie, P. (2012). Experimental estimation of fluctuating velocity and scalar gradients in turbulence. *Experiments in Fluids*, 53(4):925–942.

Hearst, R. J. and Ganapathisubramani, B. (2015). Quantification and adjustment of pixel-locking in particle image velocimetry. *Experiments in Fluids*, 56(10):1–5.

Hearst, R. J. and Lavoie, P. (2012). A parametric study of high reynolds number grid-generated turbulence. In *42nd AIAA Fluid Dynamics Conference and Exhibit*, page 2852. American Institute of Aeronautics and Astronautics.

Hoyas, S. and Jiménez, J. (2006). Scaling of velocity fluctuations in turbulent channels up to $Re_\tau = 2003$. *Physics of Fluids*, 18:011702.

Hultmark, M. and Smits, A. J. (2010). Temperature corrections for constant temperature and constant current hot-wire anemometers. *Measurement Science and Technology*, 21(10):105404–.

Hunt, J. C. R., Durbin, P. A., and Wu, X. (1998). Interactions between freestream turbulence and boundary layers. Technical report, Center for Turbulence Research.

Hutchins, N. and Marusic, I. (2007a). Large-scale influences in near-wall turbulence. *Philosophical Transactions of the Royal Society A: Mathematical, Physical and Engineering Sciences*, 365(1852):647–664.

Hutchins, N., Nickels, T. B., Marusic, I., and Chong, M. S. (2009). Hot-wire spatial resolution issues in wall-bounded turbulence. *Journal of Fluid Mechanics*, 635:103.

Hutchins, N., N. and Marusic, I. (2007b). Evidence of very long meandering features in the logarithmic region of turbulent boundary layers. *Journal of Fluid Mechanics*, 579:1–28.

Jacobi, I. and McKeon, B. (2013). Phase relationships between large and small scales in the turbulent boundary layer. *Experiments in Fluids*, 54(3):1481.

Jacobi, I. and McKeon, B. J. (2011a). Dynamic roughness perturbation of a turbulent boundary layer. *Journal of Fluid Mechanics*, 688:258–296.

Jacobi, I. and McKeon, B. J. (2011b). New perspectives on the impulsive roughness-perturbation of a turbulent boundary layer. *Journal of Fluid Mechanics*, 677:179–203.

Jiménez, J., Hoyas, S., Simens, M. P., and Mizuno, Y. (2010). Turbulent boundary layers and channels at moderate reynolds numbers. *Journal of Fluid Mechanics*, 657:335–360.

Jiménez, J. (2004). Turbulent flows over rough walls. *Annu. Rev. Fluid Mech.*, 36(1):173–196.

Jones, M. B., Marusic, I., and Perry, A. E. (2001). Evolution and structure of sink-flow turbulent boundary layers. *Journal of Fluid Mechanics*, 428:1–27.

Jørgensen, F. E. (2002). *How to measure turbulence with hot-wire anemometers - a practical guide.* DANTEC Dynamics.

Kang, H. S., Chester, S., and Meneveau, C. (2003). Decaying turbulence in an active-grid-generated flow and comparisons with large-eddy simulation. *Journal of Fluid Mechanics*, 480:129–160.

Kim, K. C. and Adrian, R. J. (1999). Very large-scale motion in the outer layer. *Physics of Fluids*, 11(2):417–422.

Klewicki, J., Fife, P., Wei, T., and McMurtry, P. (2007). A physical model of the turbulent boundary layer consonant with mean momentum balance structure. *Philosophical Transactions of the Royal Society of London A: Mathematical, Physical and Engineering Sciences*, 365(1852):823–840.

Klewicki, J. C. (2010). Reynolds number dependence, scaling, and dynamics of turbulent boundary layers. *Journal of Fluids Engineering*, 132(9):094001–094001.

Kline, S. J., Reynolds, W. C., Schraub, F. A., and Runstadler, P. W. (1967). The structure of turbulent boundary layers. *Journal of Fluid Mechanics*, 30:741–773.

Knebel, P., Kittel, A., and Peinke, J. (2011). Atmospheric wind field conditions generated by active grids. *Experiments in Fluids*, 51:471–481.

Kondjoyan, A., Péneau, F., and Boisson, H.-C. (2002). Effect of high free stream turbulence on heat transfer between plates and air flows: A review of existing experimental results. *International Journal of Thermal Sciences*, 41(1):1–16.

Larssen, J. V. (2005). *Large Scale Homogeneous Turbulence and Interactions with a Flat-Plate Cascade.* PhD thesis, Aerospace and Ocean Engineering.

Larssen, J. V. and Devenport, W. J. (2011). On the generation of large-scale homogeneous turbulence. *Experiments in Fluids*, 50:1207–1223.

Ligrani, P. M. and Bradshaw, P. (1987). Spatial resolution and measurement of turbulence in the viscous sublayer using subminiature hot-wire probes. *Experiments in Fluids*, 5(6):407–417.

Lozano-Durán, A., Flores, O., and Jiménez, J. (2012). The three-dimensional structure of momentum transfer in turbulent channels. *Journal of Fluid Mechanics*, 694:100–130.

Lozano-Durán, A. and Jiménez, J. (2014). Effect of the computational domain on direct simulations of turbulent channels up to $Re_\tau = 4200$. *Physics of Fluids*, 26(1).

Lu, S. S. and Willmarth, W. W. (1973). Measurements of the structure of the reynolds stress in a turbulent boundary layer. *Journal of Fluid Mechanics*, 60(3):481–511.

Makita, H. (1991). Realization of a large-scale turbulence field in a small wind tunnel. *Fluid Dynamics Research*, 8(2):53–64.

Makita, H. and Miyamoto, S. (1983). Generation of high intensity turbulence and control of its structure in a low speed wind tunnel. In *2nd Asian Congress on Fluid Mechanics*, pages pp. 101–106.

Marusic, I. and Heuer, W. D. C. (2007). Reynolds number invariance of the structure inclination angle in wall turbulence. *Phys. Rev. Lett.*, 99:114504.

Marusic, I., Mathis, R., and Hutchins, N. (2010a). High Reynolds number effects in wall turbulence. *International Journal of Heat and Fluid Flow*, 31(3):418–428. Sixth International Symposium on Turbulence and Shear Flow Phenomena.

Marusic, I., Mathis, R., and Hutchins, N. (2010b). Predictive model for wall-bounded turbulent flow. *Science*, 329(5988):193–196.

Marusic, I., McKeon, B. J., Monkewitz, P. A., Nagib, H. M., Smits, A. J., and Sreenivasan, K. R. (2010c). Wall-bounded turbulent flows at high reynolds numbers: Recent advances and key issues. *Physics of Fluids*, 22(6):065103.

Marusic, I., Monty, J. P., Hultmark, M., and Smits, A. J. (2013). On the logarithmic region in wall turbulence. *Journal of Fluid Mechanics*, 716:R3.

Mathis, R., Hutchins, N., and Marusic, I. (2009). Large-scale amplitude modulation of the small-scale structures in turbulent boundary layers. *Journal of Fluid Mechanics*, 628:311–337.

Mathis, R., Hutchins, N., and Marusic, I. (2011a). A predictive inner-outer model for streamwise turbulence statistics in wall-bounded flows. *Journal of Fluid Mechanics*, 681:537–566.

Mathis, R., Marusic, I., Hutchins, N., Monty, J., and Harun, Z. (2015). Inner-outer interaction predictive model for wall-bounded turbulence subjected to pressure gradient effect. In *International Symposium on Turbulence and Shear Flow Phenomena (TSFP-9)*.

Mathis, R., Marusic, I., Hutchins, N., and Sreenivasan, K. R. (2011b). The relationship between the velocity skewness and the amplitude modulation of the small scale by the large scale in turbulent boundary layers. *Physics of Fluids*, 23(12):121702.

McKeon, B. and Morrison, J. (2007). Asymptotic scaling in turbulent pipe flow. *Philosophical Transactions of the Royal Society of London A: Mathematical, Physical and Engineering Sciences*, 365(1852):771–787.

Metzger, M. M. and Klewicki, J. C. (2001). A comparative study of near-wall turbulence in high and low reynolds number boundary layers. *Physics of Fluids*, 13(3):692–701.

Millikan, C. (1938). A critical discussion of turbulent flows in channels and circular tubes. In *Proc. 5th International Congress on Applied Mechanics, Cambridge, MA, USA*, pages 386–392.

Monkewitz, P. A., Chauhan, K. A., and Nagib, H. M. (2008). Comparison of mean flow similarity laws in zero pressure gradient turbulent boundary layers. *Physics of Fluids*, 20(10):105102.

Monty, J. P., Hutchins, N., Ng, H. C. H., Marusic, I., and Chong, M. S. (2009). A comparison of turbulent pipe, channel and boundary layer flows. *Journal of Fluid Mechanics*, 632:431–442.

Mydlarski, L. and Warhaft, Z. (1996). On the onset of high-Reynolds-number grid-generated wind tunnel turbulence. *Journal of Fluid Mechanics*, 320:331–368.

Nagata, K., Sakai, Y., and Komori, S. (2011). Effects of small-scale freestream turbulence on turbulent boundary layers with and without thermal convection. *Physics of Fluids*, 23(6):065111.

Nagib, H. M. and Chauhan, K. A. (2008). Variations of von Kármán coefficient in canonical flows. *Physics of Fluids*, 20(10):101518.

Panton, R. L. (2001). Overview of the self-sustaining mechanisms of wall turbulence. *Progress in Aerospace Sciences*, 37(4):341–383.

Patel, V. C. (1965). Calibration of the preston tube and limitations on its use in pressure gradients. *Journal of Fluid Mechanics*, 23:185–208.

Perry, A. E. and Li, J. D. (1990). Experimental support for the attached-eddy hypothesis in zero-pressure-gradient turbulent boundary layers. *Journal of Fluid Mechanics*, 218:405–438.

Placidi, M. (2015). *On the effect of surface morphology on wall turbulence.* PhD thesis, University of Southampton.

Poorte, R. and Biesheuvel, A. (2002). Experiments on the motion of gas bubbles in turbulence generated by an active grid. *Journal of Fluid Mechanics*, 461:127–154.

Raffel, M., Willert, C., Wereley, S. T., and Kompenhas, J. (2007). *Particle Image Velocimetry: A Practical Guide.* Springer-Verlag.

Robinson, S. K. (1986). Instantaneous velocity profile measurements in a turbulent boundary layer. *Chemical Engineering Communications*, 43(4-6):347–369.

Schlatter, P. and Örlü, R. (2010a). Assessment of direct numerical simulation data of turbulent boundary layers. *Journal of Fluid Mechanics*, 659:116–126.

Schlatter, P. and Örlü, R. (2010b). Quantifying the interaction between large and small scales in wall-bounded turbulent flows: A note of caution. *Physics of Fluids*, 22(5):051704.

Sciacchitano, A., Neal, D. R., Smith, B. L., Warner, S. O., Vlachos, P. P., Wieneke, B., and Scarano, F. (2015). Collaborative framework for piv uncertainty quantification: comparative assessment of methods. *Measurement Science and Technology*, 26(7):074004–.

Sharp, N., Neuscamman, S., and Warhaft, Z. (2009). Effects of large-scale free stream turbulence on a turbulent boundary layer. *Physics of Fluids*, 21(9):095105.

Simmons, L. F. G. and Salter, C. (1934). Experimental investigation and analysis of the velocity variations in turbulent flow. *Proceedings of the Royal Society of London. Series A, Containing Papers of a Mathematical and Physical Character*, 145(854):pp. 212–234.

Smits, A. J., McKeon, B. J., and Marusic, I. (2011). High-Reynolds number wall turbulence. *Annual Review of Fluid Mechanics*, 43(1):353–375.

Stefes, B. and Fernholz, H.-H. (2004). Skin friction and turbulence measurements in a boundary layer with zero-pressure-gradient under the influence of high intensity free-stream turbulence. *European Journal of Mechanics - B/Fluids*, 23(2):303–318.

Taylor, J. R. (1997). *An Introduction to Error Analysis: The Study of Uncertainties in Physical Measurements.* University Science Books.

Theodorsen, T. (1952). Mechanism of turbulence. Columbus: Ohio State University. Proc. 2nd Midwest. Conf. Fluid Mech.

Thole, K. A. and Bogard, D. G. (1996). High freestream turbulence effects on turbulent boundary layers. *Journal of Fluids Engineering*, 118:276–284.

Tropea, C., Yarin, A., and Foss, J. (2007). *Springer Handbook of Experimental Fluid Mechanics.*

Tutkun, M., George, W. K., Delville, J., Stanislas, M., Johansson, P. B., Foucaut, J.-M., and Coudert, S. (2009). Two-point correlations in high Reynolds number flat plate turbulent boundary layers. *Journal of Turbulence*, 10(N21):1–23.

Wallace, J. M. (2014). Space-time correlations in turbulent flow: A review. *Theoretical and Applied Mechanics Letters*, 4(2):022003–.

Wallace, J. M., Eckelmann, H., and Brodkey, R. S. (1972). The wall region in turbulent shear flow. *Journal of Fluid Mechanics*, 54:39–48.

Wei, T. and Klewicki, J. (2016). Scaling properties of the mean wall-normal velocity in zero-pressure-gradient boundary layers. *Phys. Rev. Fluids*, 1(8):082401.

Willmarth, W. W. and Lu, S. S. (1972). Structure of the Reynolds stress near the wall. *Journal of Fluid Mechanics*, 55:65–92.

Zagarola, M. V. and Smits, A. J. (1998). Mean-flow scaling of turbulent pipe flow. *Journal of Fluid Mechanics*, 373:33–79.

Örlü, R. (2009). *Experimental studies in jet flows and zero pressure-gradient turbulent boundary layers.* PhD thesis, KTH Royal Institute of Technology.